

A Survey of Irradiated Pillars, Globules, and Jets in the Carina Nebula

P. Hartigan ¹, M. Reiter ², N. Smith ², J. Bally ³,

ABSTRACT

We present wide-field, deep narrowband H₂, Br γ , H α , [S II], [O III], and broadband I and K-band images of the Carina star formation region. The new images provide a large-scale overview of all the H₂ and Br γ emission present in over a square degree centered on this signature star forming complex. By comparing these images with archival HST and Spitzer images we observe how intense UV radiation from O and B stars affects star formation in molecular clouds. We use the images to locate new candidate outflows and identify the principal shock waves and irradiated interfaces within dozens of distinct areas of star-forming activity. Shocked molecular gas in jets traces the parts of the flow that are most shielded from the intense UV radiation. Combining the H₂ and optical images gives a more complete view of the jets, which are sometimes only visible in H₂. The Carina region hosts several compact young clusters, and the gas within these clusters is affected by radiation from both the cluster stars and the massive stars nearby. The Carina Nebula is ideal for studying the physics of young H II regions and PDR's, as it contains multiple examples of walls and irradiated pillars at various stages of development. Some of the pillars have detached from their host molecular clouds to form proplyds. Fluorescent H₂ outlines the interfaces between the ionized and molecular gas, and after removing continuum, we detect spatial offsets between the Br γ and H₂ emission along the irradiated interfaces. These spatial offsets can be used to test current models of PDRs once synthetic maps of these lines become available.

1. Introduction

Most stars form within large molecular cloud complexes that are also sites of massive star formation. Massive stars have profound effects on their parent clouds, primarily by

¹Rice University, Department of Physics and Astronomy, 6100 S. Main, Houston, TX 77521-1892

²Department of Astronomy, University of Arizona, Tucson, AZ 85721

³Center for Astrophysics and Space Astronomy, University of Colorado, Boulder, CO 80309

emitting copious amounts of extreme ultraviolet radiation that create large bubbles of ionized gas which then expand to produce blisters as the gas emerges from the confines of the cloud. Along the edges of the ionized volumes, far-ultraviolet radiation impinges upon the dark clouds, heating and dissociating the molecular gas in a photodissociation region (PDR, a.k.a. photon-dominated regions; e.g. Hollenbach & Tielens 1997). As the molecular cloud evaporates, the PDR boundary can develop pillars, which later detach to create isolated globules, often with a young star located near the apex of the globule (e.g. O’Dell et al. 1993; Hester et al. 1996). Because PDR boundaries trace surfaces where massive stars deposit energy back into their nascent clouds, following how these boundaries evolve with time is important from the standpoint of star formation energetics. PDRs also provide examples of interfaces between hot ionized gases and cooler, neutral gases where dynamical instabilities may develop.

Because molecular clouds are shrouded in dust, extinction may completely hide PDRs from view at optical and UV wavelengths. Fortunately, H_2 fluorescence makes it possible to observe PDR interfaces directly in the near-infrared where extinction is an order of magnitude lower. Figure 1 summarizes the basic physics of this interaction. FUV radiation from high-mass stars excites H_2 into the Lyman and Werner bands, and subsequent cascades generate strong $2.12\mu\text{m}$ quadrupole line emission from the $v = 1-0$, $J = 3-1$ transition. Hence, the 1-0 S(1) line defines the PDR interface, allowing us to observe precisely where the FUV radiation is absorbed.

Different regions of star formation possess distinct kinds of irradiated interfaces. For example, although the Carina nebula (and to a lesser extent the Eagle Nebula) have a rich array of pillars, globules, and walls, the more massive but significantly older Cyg OB2 association has mostly isolated globules, while Ara OB1 shows a single long wall (Hartigan et al. 2012). These variations arise from the combined effects of differing ages, number and location of massive stars, and density structures within the parent molecular clouds.

Located 2.3 kpc from the Sun (Smith 2006a), Carina is an ideal target to study firsthand how stars form in the presence of strong radiation. The region contains $\gtrsim 70$ O-type stars (Smith 2006b), and as such is more representative of a typical H II region we might observe in another galaxy (as opposed to regions like Orion that have $\lesssim 10$ O stars). Carina is also young enough to have much ongoing star formation, but old enough that the most massive stars have cleared away enough material to reveal a spectacular naked-eye H II region replete with a dizzying array of globules and pillars. Carina spans more than a degree on a side, but with modern imaging systems it is now possible to acquire high-resolution large-scale images that cover the entire star-forming region in a single observing run. Some of the most massive stars in our galaxy are located in Carina, including spectral types as early as O2

(Walborn et al. 2002), WNH stars (Smith & Conti 2008), and of course, the famous LBV star Eta Car, a prime candidate for the next Galactic supernova.

Carina provides a snapshot of the early phases of an OB association. Its massive O-type stars are distributed in several clusters, with the two largest groups, Tr 14 and Tr 16, situated in the central cavity of the nebula. These two groups contain several of the most massive stars in the region, and they dominate the ionizing flux of the outer Carina Nebula. Tr 16 consists of several sub-clusters identified from X-ray surveys (Feigelson et al. 2011; Wolk et al. 2011), while Tr 14 and the nearby cluster Tr 15 appear more compact. Typical ages for the young stars in Tr 14 and Tr 16 are 1–3 Myr (Ascenso et al. 2007; Hur et al. 2012), with some evidence that Tr 15 is older by several million years (Wang et al. 2011). A substantial fraction of the O-type stars (about half, depending on whether or not one counts Cr 228 as part of Tr 16; see Smith 2006a) are scattered across 30-40 pc residing in several smaller sub-clusters (Tr 15, Cr 228, Cr 232, Bo 10, Bo 11, and others). The presence of multiple groups of massive stars make it difficult to determine which source or sources are responsible for ionizing any given feature within the Nebula.

Historically, the Carina Nebula was considered to be an evolved H II region with little evidence for active star formation, a conclusion based on initial far-IR surveys that targeted the inner nebula (Harvey et al. 1979; Ghosh et al. 1988). The first wide-field IR survey that revealed the large extent of ongoing star-formation activity was the *Midcourse Space Experiment (MSX)* imaging of Carina (Smith et al. 2000). These wide-field mid-IR images uncovered an extended network of pillars, globules, bubbles, and embedded IR sources spread across several degrees. A number of other studies focused on signs of star formation and bright individual PDRs in the region (Megeath et al. 1996; Brooks et al. 2000, 2001; Rathborne et al. 2002; Brooks et al. 2003; Smith et al. 2004b; Rathborne et al. 2004; Smith et al. 2005). Smith & Brooks (2007) provide an overview of the global multiwavelength structure and energy budget of Carina. Later, imaging with the *Spitzer Space Telescope* clarified much of the spatial relationship between stars, ionized gas, PAHs, and dust and also revealed thousands of embedded protostars and disk excess sources organized in a hierarchical network of young star clusters spread across 30-40 pc (Smith et al. 2010b; Povich et al. 2011a). This collection of young clusters was confirmed with wide-field X-ray images obtained with *Chandra*, which documented the numerous T Tauri stars throughout the region (e.g. Feigelson et al. 2011).

Following the first ground-based discovery of a protostellar jet in the region (HH 666; Smith et al. 2004a), a survey with the *Hubble Space Telescope (HST)* Advanced Camera for Surveys (ACS) revealed ~ 40 jets or candidate jets (Smith et al. 2010a), confirming the active ongoing star formation in the region. The *HST* images included a contiguous mosaic

of the region surrounding the Tr 14 and 16 clusters, plus a number of other individual fields in the South Pillars and other regions. Many of these protostellar jets emerge from compact dark globules, also scattered throughout the region, indicating that at least some of these compact globules must contain protostars. *Spitzer* also revealed a few candidate molecular outflows based on their excess emission in the IRAC Band 2 filter (Smith et al. 2010b). We expand the census of known outflow sources with the wide-field images in this paper.

Several recent papers have explored the Carina star-forming region with large surveys at both X-ray, IR, and sub-mm wavelengths. As part of the Chandra Carina Complex Project (CCCP; Townsley et al. 2011; Broos et al. 2011), the Carina Nebula was targeted for deep X-ray exposures, and over 14000 point sources were discovered. In the near-IR, wide-field JHK images of the central portion of the Carina complex (Preibisch et al. 2011a,b) with VLT showed that most of the X-ray sources were likely to be cluster members. In the sub-mm, Preibisch et al. (2011c) and Pekruhl et al. (2013) surveyed an area of the Carina Nebula with 18-arcsecond resolution over a square degree and identified all of the principal areas of warm dust in the region, while Roccatagliata et al. (2013) published far-IR maps of the entire region using Herschel with similar spatial resolution. In the optical, Grenman & Gahm (2014) compiled a list of dozens of small dark globules in Carina from archival HST $H\alpha$ images of the central portion of the Carina star formation region. Tapia et al. (2011) has published H_2 2.12 μ m images of selected objects within Carina, and Ohlendorf et al. (2012) discuss mid-IR *Spitzer* images of the region whose filters include lines of H_2 .

Carina, with its strong UV field, modest extinction, and plentiful ongoing star formation is the premier region for studying how ionizing radiation affects jets (e.g. Smith et al. 2010a; Ohlendorf et al. 2012). Once jets emerge into the H II region, they become photoionized by the ambient ultraviolet light. Cooling from this process complicates the interpretation of emission line images because the observed radiation arises from both shock heating and radiative heating, and it can be difficult to distinguish a photoionized filament from a photoionized jet. In fact, Reiter & Smith (2013) found that most of the $H\alpha$ and [S II] emission from several Carina jets traces ionization fronts that arise from external UV radiation. However, there is also evidence for shielding, in that the dense central parts of jets appear relatively unaffected by the ambient radiation field when they first emerge from their natal cloud cores. In a region as complex as Carina, searches for jets benefit from molecular tracers such as H_2 to unveil embedded outflows (e.g. Stanke et al. 2000, 2002; Smith et al. 2010b; Lee et al. 2012, 2013) in addition to the standard optical tracers of $H\alpha$ and [S II].

In this paper we compile the deepest H_2 and Br- γ mosaics to date of the Carina star-forming region and compare them with new narrowband optical and broadband NIR images. The images cover three times the area of the JHK mosaics of Preibisch et al. (2011a), and

reveal subarcsecond detail along dozens of interfaces where FUV radiation from massive stars is in the process of destroying ambient molecular clouds. By subtracting appropriately-scaled continuum images from the narrowband ones, we construct pure emission-line images of the irradiated interfaces. The observed spatial offsets between the $\text{Br}\gamma$ and H_2 emission along the PDRs are independent of the reddening, and quantify how quickly the molecular gas flows into the H II region. Shocked H_2 gas delineates jets while they are embedded deep within a dark cloud, and complements the spatial structure of jets inferred from $\text{H}\alpha$ and [S II] emission (cooling zones of shocks and irradiated flows). Our [O III] images show the most highly-ionized parts of pillars, identify the highest shock velocities, and help to quantify how ambient UV-radiation fields affect shocked gas.

A main focus of this paper is to identify all the observable outflows and irradiated interfaces in Carina that are visible in our images, with the aim to provide a snapshot of the walls, pillars, globules, clusters, jets, and so on that are present within a typical region of ongoing massive star formation. Numerical simulations which include magnetic fields and radiative transfer (e.g. Arthur et al. 2011) can use the examples shown here to compare with the types of structures present in the models in order to better understand how star formation evolves in real systems.

2. Observations

2.1. H_2 , $\text{Br}\gamma$ and K Mosaics

The near-IR images of Carina in this paper were taken 11 – 18 March, 2011 with the NEWFIRM camera at the NOAO Blanco 4-m telescope at Cerro-Tololo in Chile. NEWFIRM is a large-format imager that consists of four 2048×2048 InSb arrays (Probst et al. 2008). A single exposure covers 27.6 arcminutes with a gap of 35 arcseconds between the arrays at a scale of 0.4 arcseconds per pixel. Images were taken in J, H, K, and through narrowband filters centered at H_2 1-0 S(1) and $\text{Br}\gamma$ using the standard NEWFIRM filter set. The H_2 and $\text{Br}\gamma$ filters both have $\Delta\lambda/\lambda$ of $\sim 1.1\%$. All mosaics were reduced and analyzed within the IRAF environment.

Because there are gaps between the arrays as well as numerous cosmetic defects, the usual strategy for observing with NEWFIRM is to obtain at least several dozen dithered exposures of a single field and use software to combine the set of images into a single mosaic; NOAO has devised a pipeline reduction process to perform this task. Unfortunately the pipeline does not work well for regions such as Carina that have a large amount of extended emission, because the pipeline interprets the extended emission as enhanced background

sky, and subtracts it. As a result, artificial negative ‘bowls’ surround all regions of extended emission in the pipeline reductions.

To solve this problem we observed $\text{Br}\gamma$ and H_2 in 6×6 grids with two small (< 1 arcminute) random dithers for each grid point and employed offsets between adjacent grid points of typically 6 arcminutes. With this strategy each point in the mosaic is observed enough times to eliminate bad pixels, and the grid covers a wide enough area so that each array has a substantial number of exposures that have no objects with extended emission, thereby eliminating sky-subtraction biases. However, this procedure demands that the sky exposures are always free of extended emission, so it is not possible to use the pipeline default of a group of exposures nearest in time. We tested our procedure by using a more time-consuming method of offsetting 1.5 degrees away for sky during the mosaic. Such large offsets proved problematic as they introduced significant positional drift during the mosaic, but the result was similar to what we were able to achieve with our $6\times 6\times 2$ mosaic.

Exposure times at each pointing were 2 minutes, so the entire exposure time for a single mosaic is 72 minutes. Allowing for dithers, telescope settling, and readout, each mosaic takes about 2 hours to complete in real time. The actual exposure time for a given location in the mosaic is largest near the center of the mosaic, and decreases towards the edges because fewer images contribute to the final mosaic at those locations. Nights with the best seeing were used for the H_2 and $\text{Br}\gamma$ observations. The sky was stable enough during the exposure sequence to enable sky subtraction between any two images in a given mosaic. Eliminating the mosaics with the worst seeing, we were left with 4 mosaics in $\text{Br}\gamma$ and 6 mosaics in H_2 . Combining these produced the final mosaic for each filter. The resulting H_2 and $\text{Br}\gamma$ mosaics have excellent image quality (FWHM images of 0.74 arcseconds and 0.79 arcseconds, respectively), each span about 1.1 degrees on a side, and have central exposure times of 3.5 hours for H_2 and 2.4 hours for $\text{Br}\gamma$ (Table 1). Distortion corrections and final coordinate mapping for the NEWFIRM images are determined by the pipeline process, and make use of known positions of bright stars in the 2MASS catalog. A check of the coordinates for several of the brightest stars in the final mosaics against their position in the SIMBAD database shows errors $\lesssim 1$ pixel (0.4 arcseconds).

We also imaged Carina in J, H, and K, with the aim of establishing a photometric database for the region, and as an aid to subtracting ambient continuum radiation as described below. Large-scale nebular emission is less of a problem for these filters, so we could acquire them using small mosaics under less favorable weather conditions, and later combine them to produce full mosaics. As such, the image quality in the J, H, and K-band mosaics, while typically 0.7 arcseconds, varies across the field of view and approaches 2 arcseconds in a few areas.

Interpreting narrowband images of regions like Carina can be problematic because reflected light from dust may be present along the same interfaces that produce H_2 and $Br\gamma$ emission lines. However, because the wavelengths of H_2 and $Br\gamma$ are nearly the same, the reddening is essentially identical at each point in the two images; hence, the continuum can be removed well by simply forming a scaled difference image ($H_2 - C \times Br\gamma$), where the scale factor C takes into account the differences in the filter bandpass widths. The NEWFIRM filter bandpasses imply $C=1.19$ for flat continuum sources. To verify this number we performed photometric measurements on a sample of stars in the final mosaics and found $C = 1.19 \pm 0.05$. All $H_2 - Br\gamma$ difference images shown in this paper include this correction factor. While extended continuum subtracts out well in the $H_2 - Br\gamma$ composites, stellar images typically leave a dark core surrounded by a light halo because the seeing was slightly better in the final H_2 composite than it was in $Br\gamma$. Stars that have strong $Br\gamma$ emission will appear white in the difference images.

The $H_2 - Br\gamma$ difference images are very effective for showing gradients in PDRs. However, quantifying the spatial offsets between the emission lines requires comparing spatial profiles across the two narrowband images, and these profiles include continuum. In principle one can remove the continuum algebraically by using the H_2 , $Br\gamma$, and K-band filters, scaling from their respective bandpasses and noting that any H_2 and $Br\gamma$ emission lines also contribute to the K-band flux (essentially three equations and three unknowns at each point in the image). While mathematically correct, the different seeing in the three mosaics leads to poor subtractions of point sources and distracting residuals at the locations of the stars. Hence, we have performed this procedure only along the edges of pillars and bright PDR interfaces where we measure the spatial offsets between H_2 and $Br\gamma$ (see section 3.2).

2.2. $H\alpha$, [S II], [O III], I-band, and Spitzer IRAC Mosaics

We obtained narrow-band images of the Carina Nebula on 9 – 11 March 2003 using the 8192×8192 pixel Mosaic 2 imager mounted at the prime focus of the CTIO 4-meter Blanco telescope. This camera has a pixel scale of $0.27'' \text{ pixel}^{-1}$ and a $35.4'$ field of view. We used $\Delta\lambda = 80 \text{ \AA}$ interference filters centered on the $\lambda = 5007$ [OIII] line, the $\lambda = 6563$ $H\alpha$ line, and the $\lambda\lambda = 6717 / 6731$ [S II] doublet, and a broad-band filter transmitting the SDSS i band. In each filter, we took several individual exposures with slight positional offsets to correct for gaps in the CCD array and to correct for detector artifacts.

We reduced the data in the standard fashion with the MSCRED package in IRAF, and absolute sky coordinates were computed with reference to USNO catalog stars. Emission-line images were flux calibrated by comparison with images of the Orion Nebula obtained during

the same run, and the Orion images were calibrated with reference to HST data. Distortion corrections for the Mosaic images were determined by measuring ~ 100 stars in common between the optical and NEWFIRM images, resulting in alignment errors ~ 0.1 arcsecond RMS between the optical and IR images.

In this paper we also make use of existing Spitzer images of the region. Smith et al. (2010b) targeted two regions in the Carina nebula with Spitzer for deep imaging in order to search for lower-mass protostars ($1-3 M_{\odot}$). Based on extended mid-IR emission in lower-resolution images from the MSX survey, those authors observed the South Pillars to further study the complex molecular emission and evidence for current star formation amid a large number of recently formed stars. The western region was chosen as an edge-on view of an ionization front and photodissociation region that also shows signs of star formation. These data were reduced using the GLIMPSE pipeline, and are described in more detail in Smith et al. (2010b).

In the following sections we consider the PDR interfaces as defined by H_2 fluorescence, and then turn to what the NEWFIRM and MOSAIC images reveal about outflows.

3. Observations of PDR Interfaces

Figure 2 identifies 61 areas of interest in the H_2 and $Br\gamma$ mosaics that are reproduced in Figs. 3 to 14. Each area has some notable aspect of H_2 or $Br\gamma$ emission, in the form of a spatially-resolved irradiated surface, a jet, cavity, bow shock or distinct nebular feature. These areas are located in one of eight larger regions in Carina: the Southern Pillars (Figures 3 and 4), the Eastern Walls (Figures 5, 6, and 7), the Northern Pillars (Figure 8 and 9), the vicinity of Tr 14 (Figure 10), a region around η Car (Figure 11), the Southwestern Pillars and Walls (Figure 12), the Northwestern Pillars and Walls (Figure 13), and the Western Wall (Figure 14). In what follows we collect the various types of objects together and refer to them by their area number.

3.1. Irradiated Walls, Pillars, and Globules

Several molecular ‘walls’ of irradiated H_2 with lengths 1 pc - 5 pc exist within the boundaries of the survey. As expected, pillars and waves along these walls form on the sides that face the ionizing sources in the center of mosaic, though it is difficult to assign a definitive exciting source owing to the large number of O stars in the region. Overplotting the 94 candidate OB stars of Povich et al. (2011b) on the H_2 composite did not yield any

insights into the identities of the exciting sources.

The walls generally divide into three categories: (1) *structured walls with few or no pillars* as exist in Areas 5, 9, 16, 46, 47, 51, and 56; (2) *structured walls with ‘chunky’ pillars that have aspect ratios $1 \sim 2$* in Areas 3, 7, 10, 11, 14, 33, 44, 48, 49, 52, 53, 59, 60, and 61; and (3) *structured walls with well-defined pillars* such as those in Areas 22, 27, 29, 32, 44, and 50. There does not seem to be any obvious relationship between the (projected) distance of the walls from Tr 14 and Tr 16 and the presence of pillars. For example, pillars exist along the walls in both Areas 29 and 44, the former situated only about 1.5 pc from Tr 14, while the latter lies at the western extreme of the H₂ emission a bit more than 10 pc away in projection from both Tr 14 and Tr 16.

The pillars come in a variety of aspect ratios, ranging from those with rounded heads and aspect ratios ~ 5 (Areas 1, 3, 8, 14, 15, 17, 18, 27, 31, 45, bottom of Area 22) to pillars that are very long and narrow (Areas 2, 4, 21, 23, 24, 37, top-right corner of Area 10). It is common for pillars to exhibit multiple arcs along their sides, implying a shouldered or scalloped shape (Areas 1, 2, 4, 18, 20, 21, 27, 33, 45). Some pillars have one or more bright NIR continuum sources situated near their apices (Areas 2, 3, 4, 8, 18, 21, bottom of Area 10), while others do not (Area 1, 14, 17, bottom of Area 22). There are many background and foreground stars in the region that could by chance coincide with the apex of any given pillar. However, in some cases (e.g. Area 4) enhanced Br- γ emission at the location of the NIR source associates the source with the pillar.

Isolated irradiated globules and pillars that have detached from their parent clouds exist throughout the region, and abound in the vicinity of Eta Car and Tr 14. Some of these show a classic head-tail ‘proplyd’ shape (Areas 23 and 24), while others are much more irregular (Areas 25 and 28). Several of these objects have one or more bright NIR continuum sources near their apices (Area 6, 21, 23, 24, 25, 40, 41, 55, upper left corner of Area 15), while others do not show any obvious NIR continuum sources near the head of the pillar (Area 12, 28, 32, 35, 36, 38, 39, 54, the object to right of main pillar in Area 4, and small globules in Area 6). In many cases the NIR source at the apex may drive a jet, but these can be difficult to detect at ground-based spatial resolution, and also because in the absence of strong extinction, Br γ is considerably fainter than H α for both shocked and irradiated flows. For example, Smith et al. (2010b) identified the star at the southern end of the pillar in Area 24 of Fig. 10 as the driving source for the HH 1013 flow they discovered with HST ACS images, but these HH objects are too small to resolve against the variable background in our ground-based images.

A collection of H₂ emission features in Fig. 2 in the Eastern Wall region that extends from Area 13 through Area 14 in Fig. 6 has some unusual characteristics. Unlike the major pillars highlighted above, all of which are bright in 70 μ m Herschel images (Preibisch et al.

2012), these regions of H₂ emission are not readily-visible with Herschel. However, there is a good correlation between absorption in our H α images and these H₂ structures, so some dust exists in these regions. The most likely explanation is that we are observing a low-extinction PDR that lacks sufficient dust column density to produce observable far-IR continuum.

3.2. Spatial Offsets between H₂ 1-0 S(1) and Br γ

Throughout the Carina Nebula we consistently observe spatial offsets between Br γ and H₂ emission along irradiated interfaces in the sense that Br γ is located closer to the source of ionizing radiation. This spatial offset is typically $\sim 1''$, which corresponds to ~ 20 times the RMS scatter between the stellar positions in the Br γ and H₂ images. This offset is independent of the reddening, and a potentially important diagnostic for PDRs. The offset involves a rather complex interplay between the atomic, molecular and ionized gas, the dust, and the radiation field. Both dust and gas serve to shield the molecular cloud from the radiation, but the opacities vary strongly with wavelength at ionization thresholds, and the situation is complicated by photoablation that causes newly-ionized gas to flow away from the cloud. Numerical models that include the requisite atomic and molecular radiative transfer as well as dynamics are just becoming available (e.g. Arthur et al. 2011), so quantifying these spatial offsets is a timely endeavor from the observational standpoint, and will hopefully motivate numerical models to predict offsets from their codes.

We chose the spectacular irradiated interface associated with G287.38-0.62 (Retallack 1983; Brooks et al. 2003; the 'Western Wall' in Area 61 of Fig. 14; see Fig. 15 for a color composite) to study emission line offsets in PDRs. This interface is very bright in all emission lines, and is large enough to allow measurements to be made along the periphery of the cloud where the incident ionizing radiation is more oblique, and near the apex where the radiation is more normal to the surface. One complication is that irradiated interfaces emit continuum radiation from reflected starlight. The filter bandpasses for Br γ and H₂ have somewhat different widths, and so subtraction between the two images could potentially affect the spatial distribution of the emission. We removed the continuum using the procedure described in section 2.1.

Intensity profiles extracted along the four line segments shown in Fig. 15 appear in Fig. 16. We define the position of the ionization front as the location where the normalized H α and [S II] profiles intersect. In practice, this location is simply a convenient fiducial point. In each panel there is a small offset on the order of 10^{16} cm between the peaks of the H α and [S II] emission, with the H α occurring, as expected, closer to the ionizing source. The decline of the integrated H α flux as the line of sight proceeds into the PDR also occurs in

Br γ . The lack of significant spatial offsets between these two hydrogen recombination lines implies that differential extinction from dust does not affect these profiles significantly. The fluoresced H₂ emission is offset by $\sim 5 \times 10^{16}$ cm from the Br γ (one arcsecond corresponds to 3.4×10^{16} cm). The profiles look similar to one-another even though we extracted them from different locations and projected angles relative to η Car and Tr 16. When interpreting these spatial offsets one must keep in mind projection effects caused by the curvature of the globule. Ideally, numerical models would predict spatial emission profiles integrated along the line of sight to compare with these observations.

4. Jets, Outflows, and Nebulous Objects

Narrowband H₂ imaging provides a view of the molecular outflows that are obscured at visual wavelengths and that may be unresolved with Spitzer’s relatively coarse angular resolution at $\lambda > 3 \mu\text{m}$. Jets with H₂ emission are usually still embedded in their natal clouds and shielded from the UV radiation that can dissociate molecules in exposed parts of the flows. In this section we first consider what the new images reveal about several previously-known flows, go on to identify new molecular outflow candidates based on their H₂ and [S II] morphologies, and then discuss several peculiar nebulous objects. Half of the candidate molecular flows fall within the field of view imaged with HST, whereas both new optical flows are in locations only imaged from the ground. Coordinates for the new candidate outflows are listed in Table 2.

4.1. Known Outflows

Smith et al. (2010a) detected 39 candidate and confirmed HH jets in the Carina nebula, only one of which had been observed before in ground-based images (HH 666; Smith et al. 2004a). In hindsight, several of the HH jets discovered with HST are also visible in earlier ground-based images, but except for HH 666, the jet-like morphologies of the HST objects were unclear in the ground-based data. Thirty-five of the HST jets in Carina fall within the field of view imaged with NEWFIRM (the remaining four are in NGC 3324). While a few of these jets have H₂ emission, most are too narrow or too faint to be discerned readily in the IR images. Nevertheless, the NEWFIRM images often provide valuable insights as to how irradiated pillars, globules, and the driving stars relate to the jets. In this section we discuss what the new images reveal about several of the most notable jets.

HH 666: HH 666 is a straight bipolar jet that emerges from the head of a dust pillar in

the bright-rimmed globule G287.57-0.91 (Smith et al. 2004a; Area 3 in Fig. 3; Fig. 18). The pillar itself points toward η Carinae. Optical imaging of this parsec-scale jet shows a chain of knots emitting in $H\alpha$ and [S II] along the jet axis outside the globule, while narrow-band near-IR [Fe II] images trace the flow into the obscured parts of the globule and back to the embedded driving source (Smith et al. 2004a; Reiter & Smith 2013). The composite image in Fig. 18 shows that knot E appears weakly in [O III], which could arise from a fast shock ($\gtrsim 100 \text{ km s}^{-1}$) into neutral gas, or from a slower shock into ionized gas.

NEWFIRM imaging uncovers some H_2 emission inside the pillar, but none that is unambiguously associated with the jet. The $H_2 - Br\gamma$ image in Fig. 18 shows H_2 emission along what appears to be the edges of a V-shaped cavity that originates at the source and opens to the northwest along the axis of the blueshifted jet (Smith et al. 2004a). This feature has a similar morphology to the infrared reflection nebula seen in the IR images of HH 666 (Reiter & Smith 2013), but it must have H_2 emission because it persists strongly in the $H_2 - Br\gamma$ image while reflected continuum would not. Additional H_2 emission from the northern edge of the flow on both sides of the driving source may trace the molecular material excited in the walls of an outflow cavity cleared by the flow, although this is not certain given the complex filamentary background.

The driving source of the flow, HH666-IRS (located at 10:43:51.3 -59:55:21.2; Smith et al. 2004a), does not appear in the X-ray catalog of Broos et al. (2011). The object has a negative residual (white) in the $H_2 - Br\gamma$ image in Fig. 18. The ratio of the stellar fluxes in the $Br\gamma$ and H_2 narrowband images is enhanced by $\sim 15\%$ relative to the median of stars in the field and to that expected for a flat continuum. However, the very red SED of HH666-IRS (Fig. 9 of Smith et al. 2004a) will generate about 11% more flux in $Br\gamma$ than in H_2 owing to the 44 nm redder central wavelengths of the $Br\gamma$ filter. If the remaining 4% excess were caused solely by line emission at $Br\gamma$, it would imply an emission equivalent width of about 4% of the filter bandpass, or $\sim 9\text{\AA}$, similar to what is observed for actively-accreting classical T Tauri stars and Ae stars, both of which show correlations of $Br\gamma$ line luminosity with disk accretion rates (Muzerolle et al. 1998; Donehew & Brittain 2011). Hence, the observed $Br\gamma/H_2$ ratio for HH666-IRS is in line with that expected given the extremely red observed SED of the source, and $Br\gamma$ emission could explain the remaining small excess. However this inference will need to be confirmed spectroscopically.

HH 900: A dark globule (visible in Area 11 in Figure 6, and in the [O III] image in Fig. 19) has a narrow ($\sim 0.2''$) rope-like tail that extends to the northeast that is visible only at HST resolution (Fig. 4 of Smith et al. 2010a). The globule lies within a wider $\sim 2''$ streak of $H\alpha$ emission that extends along the same direction on either side of the globule and points towards of a pair of oppositely-directed bow shocks. Smith et al. (2010a) identified

the $H\alpha$ streak as a jet associated with the globule, but also noted the presence of a star near the western edge of the streak that may drive a separate microjet.

Of the three brightest stars near the globule (marked with ‘+’ in Fig. 19), only the one labeled IRS (also known as 2MASS J10451881-5944238 or PCYC 838; Povich et al. 2011a) at the western end of the $H\alpha$ streak appears unusual in that it is significantly brighter in $Br\gamma$ than it is in H_2 , indicative of a very red source and/or one with strong $Br\gamma$ emission (as described for HH666 IRS above). The spectral energy distribution of this source based on 2MASS and Spitzer photometry exhibits a strong mid-IR excess (Povich et al. 2011a). The best fit of the grid of YSO models of Robitaille et al. (2006) obtained with the on-line SED fitting routine (Robitaille et al. 2007) occurs for a nearly-edge-on disk around a $2.3 M_\odot$ star of age 8.9×10^4 yr, with a total luminosity of $45 L_\odot$ and a disk accretion rate of $1.1 \times 10^{-9} M_\odot \text{yr}^{-1}$. However, uncertainties on such model fits can be large (Offner et al. 2012); for example, Povich et al. (2011a) report $\log L = 2.1 \pm 1.4 L_\odot$ and $M = 2.5 \pm 1.2 M_\odot$ for this source.

The H_2 emission in Fig. 19 is brightest on the northern side of the dark globule, and extends along the $H\alpha$ streak both to the northeast and to the southwest. The H_2 is offset to the south of the $H\alpha$ as would occur if the globule were irradiated by sources in Tr 16 to the north. However, further interpretation of this unusual object is difficult to do from ground-based images because many of the key features such as the dark rope-like tail are unresolved, and two potential exciting sources are superposed upon the H_2 , [S II], and $H\alpha$ nebular structures. New HST images and spectroscopy of the object will appear in a future work that will investigate this object more fully (Reiter, Smith, & Bally 2014; in preparation).

HH 901: HH 901 is a jet that emerges from the head of a pillar that is irradiated by O stars in Tr 14 and Tr 16 (Smith et al. 2010a; Area 29 of Fig. 10). Our images of this source in Fig. 20 show the typical structure of an irradiated pillar, with H_2 emission surrounded by limb-brightened $H\alpha$ and $Br\gamma$. A diffuse arc which is bright in $H\alpha$ and [O III] cuts across the middle of the pillar. This feature lies along the extension of the bow shock, although the high resolution HST images suggest the bow shock and the arc may be unrelated to one another.

The $H_2 - Br\gamma$ panel in the upper right of Fig. 20 shows that the HH 901 jet emits in H_2 as it emerges from the pillar. An H_2 knot marks the location where the jet emerges from the west side of the pillar, while it is possible to trace the jet in H_2 for about 0.02 pc to the east of the pillar. If H_2 emission came only from the irradiated edge of the pillar, we would expect the emission to trace the ionization front and peak at the apex of the arc facing Trumpler 14. Instead, the H_2 emission is bright at the edge of the globule on the west side, and extends along the optical jet to the east, arguing that H_2 originates in the outflow

itself.

A continuum source labeled IRS in Fig. 20 appears along the jet near the eastern edge of the pillar in the K-band and Br-gamma images at 10:44:03.58 -59:31:01 (2000), and is also visible in the I-band image. However, the stellar density is high enough in the near-IR that chance superpositions are a concern, and in HST images (Reiter & Smith 2013) the source lies above the jet axis and just outside the edge of the pillar. The object was not listed in the catalog of X-ray-selected members of Carina (Broos et al. 2011).

HH 902: Situated just above HH 901, the HH 902 jet is similar in that it originates from the tip of an irradiated pillar, though in this case the pillar is much wider (Smith et al. 2010a; Area 29 in Fig. 10; Fig. 21). A jet appears to the west of the pillar in the H α images in Fig. 21, and also somewhat less-distinctly in Br γ . The situation to the east is more complex. The HST image reveals a complex morphological structure in H α where the projection of the jet intersects the base of the pillar that contains HH 901. Reiter & Smith (2014) show that the eastern and western knots both move away from the pillar along the axis of the jet. This region has a strong continuum component in our K-band images.

The H $_2$ emission near HH 902 is rather unremarkable, and simply follows the outline of the pillar. A small nebulous knot in the H $_2$ image along the jet labeled ‘cont’ in Fig. 21 appears to be a continuum source, since its flux ratio of H $_2$ /K is similar to that of field stars. The object also appears in HST images in [Fe II] (Reiter & Smith 2013), and is likely to be unrelated to HH 902 because knots on either side of it have proper motions in the same direction (Reiter & Smith 2014). A star in the K-band image exists near the head of the pillar at coordinate J2000 10:44:01.61 -59:30:29 (Ohlendorf et al. 2012). However, the star field here is fairly dense, and there are no other indications (e.g. very red colors, reflected-light cavities, X-ray emission) that this source is driving the jet. Its position is about 2 arcseconds away from where Smith et al. (2010a) suspected the driving source should be located based on morphologies in their HST images, and is also about 2 arcseconds north of the axis defined by the H α proper motions measured by Reiter & Smith (2014). As for the other irradiated globules and pillars, the host pillar for HH 902 shows a spatial offset between H $_2$ and Br γ in its difference image (Figs. 10 and 21) in the sense that the Br γ forms a sheath on the outside of the H $_2$ emission from the pillar.

HH 1066: The newly-confirmed jet HH 1066 (formerly HH c-1) is driven from the head of a bright C-shaped proplyd (Reiter & Smith 2013). The proplyd is superposed upon a larger pillar in the background that itself has small-scale structure suggestive of at least three more pillars (Smith et al. 2010a; Area 29 of Fig. 10). The illumination source is to the south, in the general direction of Tr 14. The composite images in Fig. 22 show the proplyd and the large pillar well in H α , [S II], and even [O III] but the jet is only visible weakly in

H α and [S II] in our ground-based images.

The H $_2$ – Br γ difference image reveals the typical outline of inner H $_2$ emission enclosed by a shell of Br γ . However, towards the southwestern edge of the large pillar we find a spot of bright H $_2$ that appears to separate more from the corresponding Br γ emission to its south. The HST images hint that several interfaces converge at this point which may account for the additional H $_2$. It is also possible that a shocked knot exists at this location, but high-resolution images of this region with HST or ground-based AO will be needed to interpret the structure at this location. The exciting star located near the apex of the proplyd is PCYC 429, which has a near-infrared excess and is an X-ray source (Broos et al. 2011; Povich et al. 2011a).

HH c-9: Smith et al. (2010a) drew attention to a parabolic arc in the Tr 14 region that was bright in H α and [O III], and present but fainter in [S II]. It is located one arcminute due east of the cluster in Area 30 (Figs. 2 and 10). Our Br γ images show a similar morphology to the H α and [O III] images in Fig. 26. The object has no H $_2$ emission. The arc is a highly ionized shell of some sort, probably either a bow shock or the edge of a stellar wind bubble irradiated by stars in Trumpler 14. If it is a bow shock there is no obvious source for the flow in either the H $_2$ or Br γ images. Proper motion measurements will be the best way to determine the nature of this object.

HH 903 and HH c-10: The Smith et al. (2010a) HST ACS H α images of the southern pillar G287.88-0.93 show two distinct outflows. HH 903 originates from the center of the pillar and drives an optical jet to the west, with bow shocks that extend about an arcminute to both the east and west of the pillar. A second system, HH c-10, manifests as an H α shell that extends about 10 arcseconds to the southwest of a small cluster of stars located at the head of the pillar. Neither of these flows are easy to see in our NEWFIRM images (Area 2 of Fig. 3), though it is possible to see faint traces of the HST flows in our Br γ images. H $_2$ emission is not visible in the HH 903 jet and bow shocks or in the HH c-10 shell. However, at the location of the source of the HH 903 jet the pillar has several curved arcs like we observe at the heads of other pillars. This morphology suggests the pillar is either two pillars observed in projection, or that the pillar has a ‘shoulder’ where the driving source of the HH 903 jet lies.

HH 1008 and HH c-2: The pillar G287.73-0.92 (Area 4 of Fig. 3) is one of the most remarkable of its kind in the sky. HH 1008 is situated near the base of the pillar on the eastern side, and appears as a southward-moving bow shock in HST H α images (Smith et al. 2010a). This feature is visible in our Br γ images as well, albeit with less contrast owing to ground-based seeing. The candidate HH object c-2 located at the head of the pillar is too small to be detected from the ground. Neither object has H $_2$ emission.

4.2. New Outflows

We identified new outflow candidates in the Carina Nebula region via their morphology in our narrowband NEWFIRM and MOSAIC images. Optical outflow candidates all have bright [S II] emission, typical of HH objects. Several molecular jets and shocks appear in the H₂ images alone, but most are easier to see in the H₂ – Br γ difference images because continuum is present in similar amounts in both images and is largely removed in the subtraction. However, H₂ emission along PDRs (section 3.1) can be difficult to distinguish from shocked molecular flows in Carina. Following Davis et al. (2010), we designate objects that have clumpy or jet-like H₂ emission and do not define obvious PDR boundaries with the acronym MHO (molecular hydrogen object). Section 4.3 summarizes extended H₂ objects whose true nature remains uncertain from morphology alone.

4.2.1. New Optically-Identified Outflows and Candidates

HH 1123: HH 1123 consists of a group of four bright H α and [S II] knots arranged in a cross-shape (Fig. 23). The knots have the typical clumpy morphology of HH objects, and are not visible in [O III], Br γ or in H₂. A relatively faint star lies between knots A and C in the infrared images, but this source is not clearly associated with the emission knots. There is no indication of a jet, although a faint arc that extends from knot A to the east of knot C may mark the edge of a cavity. HH 1123 is situated along the northern extension of the Southwestern Loop. The Southwestern Loop is a region that hosts many filamentary structures and knots that appear to result from impacts of winds upon a large, slowly-expanding shell (Fig. 34), and it is possible that HH 1123 has a similar origin.

HH 1124: Images of the head of the irradiated pillar in Area 18 of Fig. 8 in H α , [S II], I-band, and H₂ are shown in Fig. 24. Three optical emission-line knots (A, B, and C) lie to the west of the pillar, while one knot (D) and a bow-shaped arc lie to the east. If we attribute all knots to a single source, then the pattern is consistent with a jet that emerges at PA \sim 53 degrees and is bent to the north by winds from the same source or sources that shape the pillar. The H₂ images show weak extensions along the axis of the putative jet that are not continuum because they are also visible in the H₂ – Br γ images in Fig. 8. However, this H₂ ‘jet’ marked in Fig. 24 could also simply define another irradiated surface along the pillar. The axis of the outflow also has extended emission in IRAC Band 2 images, including an extended green object (EGO) identified from a Band 2 – Band 1 difference image.

There are several infrared sources located near the head of the main pillar, so confusion between multiple outflows is always a concern. Two bright NIR sources positioned near the

center of the pillar, PCYC 884 and PCYC 889, are YSOs as they emit strongly in the Spitzer bandpasses (Povich et al. 2011a; Fig. 24) PCYC 884 lies at the base of an arc-shaped feature in the I-bandpass and is the only IR source in the region associated with such a feature. This arc has a morphology and orientation consistent with it defining the edge of an evacuated cavity driven by the outflow that produces knots A, B, and C. The source has a flat spectral energy distribution in the IRAC bands. Situated just to the west of PCYC 884, PCYC 889 is fainter in the near-infrared, but becomes a magnitude brighter than PCYC 884 at $24 \mu\text{m}$ (Povich et al. 2011a).

A region outlined by a box in Fig. 24 and located ~ 0.1 pc to the west of a near-infrared source (IRS 1 in the Figure) has several faint knots and extended emission in the $\text{H}\alpha$, [S II] and H_2 images. The knots are not necessarily associated with IRS 1; in fact, the $\text{H}_2 - \text{Br}\gamma$ difference image in Area 18 of Fig. 8 has an arc-shape, so this region is most likely another irradiated pillar. The object labeled IRS 2 is another red object in the direction of the globule. It lies along the axis of the main outflow and appears to be a subarcsecond binary with a PA ~ 105 degrees. Finally, a bright star just outside the edge of the pillar ~ 0.06 pc south of PCYC 884 is probably a foreground object, as it is bright in both the optical and infrared images and does not have any obvious influence on the morphology of the pillar.

HH 1125: HH 1125 is a thin, long, filamentary [S II] emission-line object located near HH 666 in the region of the southern pillars to the west of the H_2 structures shown in Area 3 of Fig. 3. The morphology of HH 1125 resembles other filamentary [S II] structures that trace the remains of an outflow lobe from an unseen driving source, such as HH 400 in Orion (Bally et al. 2001). The brightest feature in this object (marked ‘A’ in Fig. 25) has a morphology similar to that of a bow shock in a jet that propagates at position angle 280° . HH 1125 is invisible in $\text{H}\alpha$ and [O III], and also has no infrared counterparts in H_2 or $\text{Br}\gamma$, so it is unlikely to mark the edge of a dark cloud. The projected distance of the most distant observed knot B from the edge of the nebulous region is 3.7 pc, so HH 1125 would represent a large-scale outflow if it traces a jet. While any number of the bright stars in this densely-populated region could be the exciting source for a jet, none of them particularly stand out as an obvious driving source. Hence, without radial velocity and proper motion information we cannot rule out the possibility that HH 1125 represents the edge of a shell driven by one of the many massive stars in Carina.

HHc-21: Fig. 32 shows a small but distinct optical knot located about 1.5 arcseconds at PA = 200° away from a star. The knot, also faintly visible in [S II], but not in [O III], H_2 , or $\text{Br}\gamma$, is a candidate HH object we label HHc-21. The star is not listed as a member of Carina by Povich et al. (2011a). The system lies to the north of the $\text{H}\alpha$ arc R2 in the region of MHO 1622 - MHO 1626.

4.2.2. Candidate Outflows Identified in Narrowband H_2 Images

We have searched our images for evidence of shocked H_2 in outflows. Such objects typically appear as distinct knots rather than extended H_2 that defines a PDR front at the edge of a globule, wall or pillar. Morphologies of the PDRs in Carina can be quite complex, however, and it is not always immediately obvious from images alone which objects are shocked flows and which are PDRs. For this reason MHO objects in the Carina Nebula are best treated as candidate outflows pending verification by proper motions, though most will likely turn out to be outflows. A few of these were discovered independently by Preibisch et al. (2011b), and we discuss those objects together with the new sources in this section.

MHO 1605: MHO 1605 has the morphology of a barely-resolved bipolar outflow emerging from a small pillar embedded in the dark dust lane $\sim 4'$ south of Trumpler 14 (Preibisch et al. 2011b; Area 32 of Fig. 10). The object consists of two bright H_2 knots located just outside the pillar, along $PA \approx 3^\circ$. The pillar is well-defined as an extinction feature in the $Br\gamma$, $H\alpha$, [S II], and [O III] images. MHO 1605 is difficult to discern in the optical images, although there is some diffuse [S II] emission coincident with the H_2 knots. Emission in IRAC bands 1 - 3 is evident near the pillar head and is elongated along a north-south axis (not consistent with a point source), but the feature is too small (only $\sim 4''$ long in our H_2 image) to be clearly resolved with Spitzer.

Cr 232/N4 Area, MHO 1606 – 1608: Preibisch et al. (2011b) and Tapia et al. (2011) discussed the cluster Cr 232 that is associated with the extended H_2 emission in Area 33 of Fig. 10. The bright K-band source labeled IRS in Fig. 10 is a massive star embedded within a nearly edge-on circumstellar disk that Preibisch et al. (2011d) refer to as the ‘disk object’ (also known as source #902, Tapia et al. 2011). A separate foreground X-ray source, PCYC 556, is located about 2 arcseconds to the southeast of the near-IR peak, and appears in our near-IR images and those of Preibisch et al. (2011d) as a distinct point source. Fig. 10 uncovers over a dozen localized bright regions of H_2 emission in this region. Most of these follow arcs that define PDR boundaries in the dark cloud that houses the cluster, though several may turn out to result from shocks in outflows. Three bright H_2 features particularly stand out in the $H_2 - Br\gamma$ image as having a knotty morphology typical of shocked gas. The brightest of these, MHO 1607, consists of three distinct knots aligned approximately east to west over an extent of about 5 arcseconds. A few arcseconds to the northeast, MHO 1608 is more point-like, with a slight elongation along $PA 45^\circ$. Both these MHO objects are prominent in the H_2 image but are not present in $Br\gamma$. The $H_2 - Br\gamma$ image reveals two faint arcs that trail to the southeast of MHO 1608 and may outline the edges of an irradiated pillar. Neither the optical nor the IR images indicate any obvious driving source associated with these two objects, though of course there are many possibilities within the cluster,

which has 72 members according to Tapia et al. (2011). The IRAC Band 2 – Band 1 image shows diffuse emission in the area, with a modestly-bright feature located between MHO 1607 and 1608. A third object, MHO 1606, is an isolated, bright, comma-shaped H₂ knot located away from the cloud boundary ~ 80 arcseconds to the southwest of MHO 1607 and MHO 1608. This object also has weak [S II] emission.

MHO 1609: The detached pillar shown in Area 6 of Fig. 4 and in Fig. 27 is surrounded by several candidate HH objects (HH c-4 through HH c-8) identified by Smith et al. (2010a), but none of these are visible in our NEWFIRM images. However, our H₂ images uncover two extended spots of bright emission near the middle of the irradiated pillar. These spots lie just inside the H α and [S II] emission at the surface of the evaporating pillar. A K-band point source lies just west of the H₂ knots, but is offset from the probable flow axis enough that it is unlikely to be the driving source. It is unclear if the two elongated features are related as they are bright in a relatively narrow portion of the pillar, and at this resolution, are consistent with emission from the irradiated pillar edge. An alternative interpretation is that bright H₂ emission comes from photoevaporation of the denser clumps within a more diffuse pillar. None of the H₂ features in the pillar appear to be related to any of the candidate HH jets emerging from this globule that Smith et al. (2010a) identified with HST H α imaging. The five separate HH jet candidates emerging from this elongated globule suggest ongoing star formation from an object dense enough to survive despite harsh UV radiation that has largely cleared the surrounding gas and dust. In general, the H α features of the candidate HH jets are too faint or too tenuous to be identified in the ground-based images, although bright H₂ and Br γ emission from the head of the globule may reveal the protostar driving HH c-5.

MHO 1610: MHO 1610 is a single bright, compact H₂ knot embedded within more diffuse emission that probably outlines a globule as does so much of the H₂ emission from this region of the Eastern Walls (Preibisch et al. 2011b; Area 10 of Fig. 5; Fig. 28). While the images show two other nebulous objects and several stars within the boundaries of the diffuse emission, these sources also appear in the Br γ and K-band images and are dominated by continuum. The faint continuum source labeled IRS is coincident with a Herschel point source at 70 μ m. The H₂ knot is elongated by about 2.5 arcseconds along PA $\sim 45^\circ$, and is slightly narrower on its northeastern side.

MHO 1611 - 1615: MHO 1611, MHO 1612, MHO 1613, MHO 1614, and MHO 1615 form a group of H₂ knots located $\sim 8'$ northwest of Trumpler 14 (Area 52 of Fig. 13; Fig. 29). These knots reside near the edge of the dark lane that runs beneath Trumpler 14, and are centered around a loose cluster of at least 20 infrared-bright stars. The brightest star at the center of the cluster is PCYC 139, a class II infrared source with $L_{BOL} = 400 L_\odot$ and an

estimated mass of $4.9 M_{\odot}$ (Povich et al. 2011a). MHO 1611 is a group of several faint H_2 knots that stretches from near PCYC 139 to near the dark lane to the southwest. MHO 1612, MHO 1613, MHO 1614, and MHO 1615 lie within about a half arcminute of PCYC 139, and could have different exciting sources. MHO 1615 connects with a star situated 2.9 arcseconds at $PA=250^\circ$ from PCYC 139. This star appears point-like in the optical images but has an extension along the direction of MHO 1615 in the $Br\gamma$ and K-band images (Fig. 29), hence, it is the likely driving source for that portion of the H_2 emission. A faint arc of H_2 extends to the east of MHO 1613 towards MHO 1614. Another bright young star and infrared source, PCYC 147, is situated ~ 20 arcseconds to the east of the infrared cluster. Some 6 arcseconds to the south of PCYC 147 lies the optically-bright B1.5V star HD 303313, which does not appear heavily extinguished and is probably situated in front of the cluster.

The PCYC 139 cluster is not associated with ionized pillars or globules, and is not surrounded by a distinct H_2 shell that would outline the photodissociation front into a remnant cloud core. The dark lane to the southwest appears as an H_2 wall (Area 52 of Fig. 13), but this wall does not have any obvious connection with the cluster. The lack of visual counterparts to the H_2 knots suggests that the PCYC 139 cluster lies behind several magnitudes of extinction on the far side of the Carina nebula.

MHO 1616 - 1617: MHO 1616 lies 3 arcminutes west of the PCYC 139 cluster, and resembles a clumpy jet (Area 57 of Fig. 13). None of the H_2 knots have any optical counterparts. While there are several members of the Carina YSO association in the vicinity, none are aligned with the knots of MHO 1616. MHO 1617 is a faint jet of H_2 that extends for about 4 arcseconds from PCYC 179 at $PA \sim 75^\circ$ and ends in a bright knot. Another source 3 arcseconds to the south labeled ‘IR’ in Fig. 13 has an arcuate morphology that one would expect from a cavity created by an outflow along $PA \sim 50^\circ$. This direction intersects with MHO 1617, so it is possible that the IR source is responsible for some of the H_2 emission in this region. The IR source falls within the positional errorbars of a Herschel point source at $70\mu m$ (Preibisch et al. 2012).

MHO 1618: MHO 1618 is another shocked outflow candidate, this one located in the Eastern Wall region just south of Area 11 (Fig. 2). The $H_2-Br\gamma$ difference image uncovers a faint H_2 jet that is aligned with a bright infrared source not identified previously as a cluster member (Fig. 30). The source is visible in the optical and the IR images and also appears in all four IRAC Bands. We recorded the position of the IR source in Table 2, but it is also possible that the flow originates somewhere to the northwest of knot a, where a dark cloud resides. Proper motions of the H_2 knots would settle this question. The putative jet is only visible in H_2 .

MHO 1619 - 1621: A collection of bright H_2 clumps labeled MHO 1619, MHO 1620,

and MHO 1621 form part of a curve of faint extended H_2 situated ~ 11.5 arcminutes to the northeast of η Car (Area 13 of Fig. 6; Fig. 31). MHO 1619 is arc-shaped and has faint [S II] emission located to the west-northwest of knot-c. MHO 1620 appears as a chain of knots oriented east-west. Knot-a is notable for its [S II] emission, and knot-b has a complex internal structure down to the spatial resolution of the images. A third string of H_2 knots to the south of MHO 1620 defines MHO 1621. Two stars located on either side of MHO 1621 (Fig. 31) have no clear association with the H_2 . The $H\alpha$ image of the region shows a filamentary structure in absorption, implying that foreground shells of material exist in this region. None of these MHO objects has a clearly-defined exciting source.

G287.24-0.21, PCYC 438, and MHO 1622 - 1626: Area 19 of Fig. 8 and Fig. 32 reveal several potential outflow sources and groups of interesting H_2 emission line objects. Near the southeast corner of Area 19, a region of extended H_2 outlines the boundaries of the molecular cloud G287.24-0.21. The H_2 from this region forms a backwards “y” shape in Fig. 32 that is also bright in all four IRAC bands in the Spitzer images. The $H\alpha$ and [S II] emission from G287.24-0.21 are filamentary and more extensive than the H_2 , but generally follows the H_2 shape, as expected for an irradiated cloud boundary.

MHO 1622 - MHO 1626 define four groups of clumpy H_2 sources in Fig. 32. None these show any optical counterparts or obvious driving sources, though the star field in this region is rich and there are several cluster members in this region. MHO 1623, MHO 1624, and MHO 1626 are jet-like in appearance, while MHO 1622 and MHO 1625 have less-collimated morphologies. The bright NIR source PCYC 438 (Povich et al. 2011a, Fig. 32) has a bipolar nebula visible in the optical and NIR images that extends ~ 3 arcseconds on both sides of the star along $PA = 225^\circ$, though no jet is visible along the axis of the nebula. The bipolar nebula shows hints of what could be H_2 in the $H_2 - Br\gamma$ image, but the nebula is primarily a continuum source.

In addition to the MHO objects and bipolar nebula described above, five bright arc-shaped H_2 and $H\alpha$ features (labeled R1 – R5 in Fig. 32) define irradiated walls and pillars in this region. These all curve to the north, away from the dominant sources of radiation from the Tr 14 cluster and η Car. As in the other Carina PDR interfaces, the $H\alpha$ emission from the R1 – R5 arcs peaks closer to source of ionizing radiation than the H_2 emission does.

G287.10-0.73, MHO 1627 and MHO 1628: Of the four Extended Green Objects (EGOs) found in Spitzer/IRAC images by Smith et al. (2010b), only G287.10-0.73, an elongated IRAC Band 2 source located almost due west of Tr 14, is included within the field of view that we imaged in H_2 . While we do not see H_2 $2.12\mu\text{m}$ emission at the location of G287.10-0.73, probably owing to large extinction near the apex of the dusty pillar, our H_2 image

reveals a striking chain of knots that picks up where the Spitzer extension leaves off and emerges at $PA = 165^\circ$ both to the north and to the south from the head of the pillar (Area 58 of Fig. 13). On the southern side, a bright H_2 jet followed by two knots that are linked together by a stream of faint H_2 makes up MHO 1627, while on the northern side, two other bright H_2 knots comprise MHO 1628.

Both MHO 1627 and MHO 1628 are visible faintly in the Spitzer images, albeit with poor spatial resolution. No jet is visible in our Mosaic $H\alpha$, [S II] or [O III] images. A jet also does not appear in $Br\gamma$, so that the lack of $H\alpha$ is not simply due to foreground extinction. A point source at $70\mu\text{m}$ is located between MHO 1627 and MHO 1628 in Herschel images (Preibisch et al. 2012). The dark pillar associated with G287.10-0.73 is only visible in silhouette. Hence, the ambient ionizing radiation field is not strong in this region, which makes it easier for molecules to survive once the outflow leaves the confines of the dark cloud.

Overall, the number of new candidate flows discovered in Carina with NEWFIRM is smaller than would be expected based on other star-forming complexes at comparable distances (e.g. W5; Ginsburg et al. 2011). Unlike W5, Carina hosts numerous uncovered O-stars that create a harsh radiative environment capable of destroying molecules in much of the central portion of the nebula. The South Pillars region, which extends beyond the boundaries of our NEWFIRM images, has indications of ongoing star formation (e.g. Megeath et al. 1996; Smith et al. 2000; Rathborne et al. 2004; Smith et al. 2010b) that could produce additional flows. The new H_2 flows are spatially intermixed with the irradiated jets discovered with HST (Smith et al. 2010a; Fig. 17). The outflows are generally most pronounced in either optical ($H\alpha$, [S II]) or molecular (H_2) emission, but not both simultaneously. None of the molecular jets have strong optical emission and only one of the irradiated jets seen in $H\alpha$ has appreciable extended H_2 emission (see Sec. 4.1).

4.3. Other Extended Nebulous Objects

H_2 arcs: Three H_2 arcs to the west of the MHO 1619 – 1621 group (Area 13 of Fig. 6) do not clearly associate with a cloud boundary, and appear bright in H_2 . These objects look like shell fragments of some sort, but their nature is unclear.

Narrow [S II] filaments in the South Pillars region: The [S II] image and the scaled continuum-subtracted version [S II] – I_c in Area 62 (Fig. 33) reveal a remarkable pattern of five extremely thin, connected filaments. The northeastern filament labeled ‘1’ in the figure continues for several parsecs and defines the western boundary of the large pillar that contains the two bright H_2 structures in Area 3 (Figs. 2, 3). The curved shape of the cloud is

visible faintly to the west of filament 3. The southern portion of filament 3 also emits weakly in $H\alpha$. Filaments 2, 3, and 4 are most easily explained as constituting the leading edge of a bubble that is impinging upon the cloud (see inset to Fig. 33). In this model filament 5 could define the southern edge of the cloud. Proper motion measurements would be able to verify or disprove this scenario, which predicts motion of filaments 2, 3, and 4 to be northward, eastward, and southward, respectively.

The intersection points between shock fronts have generated a fair bit of interest recently because under some circumstances a normal shock known as a Mach stem may develop at this location, leading to a hot spot that has anomalous pattern motion relative to the larger bow shock structure. Multiple-epoch HST images show evidence for time-variable enhanced emission at intersection points of bow shocks exists in HH 34S and possibly also HH 47A (Hartigan et al. 2011). Laboratory experiments of this phenomena have quantified the critical angles where Mach stems can form (Foster et al. 2010; Yirak et al. 2013), and the experiments agree reasonably well with the theoretical and numerical predictions.

In Fig. 33, there is a small bright segment where filaments 3, 4, and 5 intersect, but no Mach stem should form there because the angle between filaments 4 and 5 is too acute, and none exists in the object. The situation at the junction of filaments 1, 2, and 3 is more complex. One bright [S II] knot, two fainter ones, and several foreground stars lie near the intersection point. The projected angle between filaments 1 and 2 is 75 - 105 degrees, depending on how one interprets the spatial structure at that point. An angle in the 75 - 90 degree range may produce a Mach stem, but the shock is nearly normal to the interface in any case. Filament 3 is distinctly more wavy in appearance than are the adjacent filaments, as expected if this filament marks the location of the shock as it overtakes irregularities along the surface of the cloud. The brightness variations along filament 3 seem uncorrelated with whether or not the wiggles in the front are concave or convex.

Large [S II] shells in the South Pillars region: A region where several bright arcs of [S II] overlap may define a fossil cavity driven by the massive stars to the north (Area 63 of Fig. 33). The shells extend east-west for over a parsec and are visible faintly in the $H\alpha$ images though not in [O III]

Shells and Filaments in the Southwest Loop: The southwestern boundary of the bright optical emission in the Carina Nebula is defined by a large curved arc that spans several pc in size, and within the arc lie a number of smaller knots and filaments. This region lies to the southwest of our H_2 mosaic, but was covered by the optical Mosaic images (see Fig. 34). The I_c -band image shows very little continuum along the arc. The scaled $H\alpha - I_c$ images in Fig. 34 remove stars reasonably well, and show that the arc has several bright knots situated along its inner part (labeled A - G in Fig. 34), as well as what appear to be smaller cavities

(features H, I and J) embedded in its outer portion. Knots C and F are bright and clumpy, and emit strongly in [S II].

The arc has the morphology and line emission characteristics of an expanding bubble that is ionized by massive stars at the center of the Carina Nebula. Features A – G appear to mark locations where the arc is impacted by winds that originate from the active central region of the Nebula. The existence of distinct smaller shells within the arc argues for multiple wind sources. Meaburn & Walsh (1986) discovered very similar structures within the Rosette, so this phenomenon is not unique to the Carina Nebula.

Candidate Background Planetary Nebula: Area 43 in Fig. 11 shows limb-brightened, elliptical H₂ feature with some wisps extending beyond the ellipse along a perpendicular axis. The object is unusual for Carina in that Br γ emission fills the H₂ ellipse, and weak H α is also present. A faint star is located near the center of the object. An IRAC Band 2 – Band 1 difference image reveals some extended 4.5 μ m (green) emission in the center of this object. IRAC emission matches the Br γ emission, but not H₂, suggesting we are seeing Br α and not shocked H₂ in the 4.5 μ m image in this case. The emission structure with H₂ surrounding Br γ emission, combined with a symmetrical elliptical morphology and a central star is best explained by a planetary nebula situated behind the obscuring dark clouds of the Carina nebula.

Knots near the Carina ‘Defiant Finger’: A striking irradiated globule known as the Carina Defiant Finger (Smith et al. 2004b) exists in the vicinity of the Keyhole. A chain of emission knots extends from the globule’s northern edge (from the “wrist”) that are bright in H α , [S II], and H₂ (Area 37 of Fig. 11; Fig. 35). However, the knots exhibit spatial offsets between [S II] and H α , and between H₂ and Br γ characteristic of PDRs. The [O III] image shows the knots in absorption against the nebular background, as expected for dusty globules. Faint emission from the knots in the IRAC bands is consistent with thermal emission from these dusty blobs. This collection of objects most likely define the remains of a pillar within Trumpler 16 that has been destroyed by the intense UV radiation in this region. The northern-most knot has a bright infrared source on its northern boundary labeled as ‘IRS’ in Fig. 35. This location is where a young star should be if it formed at the apex of the pillar. Smith et al. (2004b) derived a photoablation rate of $\dot{M} \approx 2 \times 10^{-5} M_{\odot} \text{ yr}^{-1}$ in this region, so small knots such as these should be transient objects.

The Runaway Star Trumpler 14 MJ 218

The Br γ images reveal a curious arc-shaped feature situated about 6 arcseconds to the northwest of a bright star (Area 26). The arc stands out in color composites owing to its relatively strong Br γ emission as compared with H₂ (Fig. 10). The star, located at

10:44:05.1 -59:33:41 (2000.0), was first observed photometrically by Feinstein et al. (1973) and later spectroscopically by Massey & Johnson (1993), and is listed in the Reed (2003) catalog of O and B stars. The above references named the star Trumpler 14 29 and Trumpler 14 MJ 218, respectively. The stellar colors are consistent with a reddened early B star, and the high-quality blue spectrum (Massey & Johnson 1993) shows a spectral type of B1.5V.

The arc has recently been discussed in some detail by Ngoumou et al. (2013), who refer to it as the ‘Sickle’ (see also Fig. 1 of Ascenso et al. 2007). As shown by Ngoumou et al. (2013), the star appears to be moving past a dense clump observed in $870\mu\text{m}$ images, and the shape and offset of the bow shock from the stellar image is consistent with a wind from the star impacting denser material in the vicinity of the globule. The star has a large proper motion of 8.7 mas yr^{-1} at PA = 307 degrees (95 km s^{-1} at a distance of 2.3 kpc), consistent with producing the bow shock (Zacharias et al. 2013), and is most likely a runaway star ejected as its companion underwent a supernova explosion. However, errors in proper motion measurements at the distance of Carina are relatively large, and if the X-ray radiation from this source arises from a companion, it may be difficult to keep the binary system intact if a more massive primary became a supernova. Our difference image ($\text{H}_2 - \text{Br}\gamma$) in Fig. 10 shows enhanced H_2 along a flattened structure that lies along the portion of the bow closest to the star, as one would expect if molecular hydrogen in the shell were excited either by the shock or by UV fluorescence from the star.

Extrapolating forward, Tr 14 MJ 218 should move a degree on the sky in about 4×10^5 years, which amounts to $\sim 10\%$ of the star-forming epoch within a typical molecular cloud. Carina hosts ~ 70 O stars, which typically become supernovae after 5 – 10 million years (Meynet & Maeder 2003). Many of these O stars are binaries, with the companions being future runaway stars. Hence, we expect at most a few runaway stars to exist within the Carina nebula at any given time. We note that one neutron star has been discovered in the Carina region, implying recent supernova activity (Hamaguchi et al. 2009), and abundance variations of heavy metals across the nebula also point to recent supernovae (Hamaguchi et al. 2007).

Tr 14 MJ 218 represents the only clear candidate for a runaway star in our field – many emission-line arcs appear in our images, but the bow shock ahead of this star is unusual in that it has a smooth, diffuse shape, a large $\text{Br}\gamma$ -to- H_2 ratio, and a bright star contained within the bow. This object, together with eight other early-type stars in Carina, were highlighted by Smith et al. (2010b) as having extended emission in $8\mu\text{m}$ Spitzer images and classified as extended red objects (EROs). Two of these EROs lie to the south of our mosaics, while the other six appear as unremarkable point sources in the $\text{Br}\gamma$ and H_2 images.

5. H₂ Within Embedded Clusters

The Carina star-formation region is sometimes referred to as a ‘cluster of clusters’; as many as 24 separate clusters were identified in the recent deep CCCP X-ray survey Feigelson et al. (2011). The Trumpler 16 region (near η Car) alone consists of least six smaller clusters, and as many as eight were identified from Spitzer data (Smith et al. 2010b). While H₂ walls and pillars often exist in the vicinity of these clusters, most clusters visible in the optical and near-IR are no longer embedded within their nascent molecular cloud cores.

However, two young clusters stand out in our images in that they have what appear to be cavities defined by Br γ emission at the cluster’s center that is surrounded by circular arcs of H₂ that mark the boundary of the cavities evacuated by the cluster stars. The most notable of these from the standpoint of H₂ emission is undoubtedly the Treasure Chest (Area 8 in Fig. 4). This region was described in some detail by Smith et al. (2005). The star at the center of the Br γ emission is an O9.5V star named CPD -59°2661, and this object excites the emission lines within the local H II region that surrounds it. A bright emission-line star (Sanduleak & Stephenson 1973, Hen 3-485 in Area 8) lies to the upper left of the cluster, and was identified as a likely Herbig Be star on the basis of its X-ray flux by Gagne et al. (2011). The near-IR observations of Preibisch et al. (2011a) show that about one-third of the stars in the Treasure Chest have near-IR excesses indicative of circumstellar disks, a fraction about three times larger than occurs in the rest of the Nebula.

The narrowband images in Fig. 3 of Smith et al. (2005) show that faint Pa β extends northward from the H₂ emission in the Treasure Chest, in the direction of η Car and Tr 16. We also observe this behavior in the reddening-independent H₂ – Br γ difference image in Area 8 of Fig. 3. Bright Br γ emission defines the H II region excited by the cluster, and a sinuous arc of H₂ outlines the PDR from the cluster. Hence, the dark cloud in which the Treasure Chest resides is undergoing photodissociation both internally from the embedded cluster, and externally from η Car and other young stars within Tr 16.

Another cluster of interest that has H₂ emission is shown in Area 30 (Fig. 10). Discovered independently by Preibisch et al. (2011b), it was not identified by Feigelson et al. (2011) as either a major cluster or as a smaller group. While less spectacular than the Treasure Chest, this cluster contains 30 - 40 stars and is surrounded by filamentary H₂ emission. The brightest NIR source is G 287.51-0.49, located at 10:44:59.70 -59:31:19.5, is also a mid-IR source (Rathborne et al. 2004; Sanchawala et al. 2007), though the lack of a prominent H II region in Br γ implies it is not a powerful source of ionizing radiation.

6. Discussion: Feedback, Triggering, and PDR Physics in the Carina Complex

6.1. Feedback

Carina is among the most active regions of star formation within several kpc of the Sun. The region contains more than 70 stars of spectral type O, has a total mass of young stars of $M_{stars} \simeq 4 \times 10^4 M_{\odot}$ and a neutral gas mass of at least $M_{gas} \simeq (0.5 - 1) \times 10^6 M_{\odot}$ (Smith 2006b; Smith & Brooks 2007; Preibisch et al. 2011b,c). The kinetic energy of the expanding nebula is about 8×10^{51} ergs, about 1/3 of the mechanical energy available from stellar winds in the past ~ 3 Myr (Smith & Brooks 2007).

Feedback from the many young massive stars in the Carina Nebula has had a profound influence on the surrounding interstellar medium. These massive stars have cleared a cavity and sculpted dozens of gas pillars that face the center of the Nebula. The detailed structure of these pillars and other cloud formations stand out in the H_2 images presented in our paper because the H_2 images trace the thin PDRs on the surfaces that outline these irradiated clouds. The relatively high sub-arcsecond angular resolution provided by these images complements the longer wavelength data that trace the warm dust and molecular gas inside the clouds seen in previous surveys with *IRAS*, *MSX*, *Spitzer*, and CO data (Yonekura et al. 2005; Smith & Brooks 2007; Smith et al. 2010b).

Recently Roccatagliata et al. (2013) analyzed the impact of feedback in Carina using ground-based APEX and space-based data (Preibisch et al. 2011b) and Herschel Space Observatory sub-mm observations of Preibisch et al. (2012). However, disentangling the emission from the thin PDRs and protostars embedded within them that emit at long wavelengths remains challenging because emission from the PDR and the protostar are not resolved from one-another at long wavelengths. Perhaps this is a task for ALMA, and to this end our new H_2 images will provide a reliable reference for the structure of the PDRs over the entire region.

Some authors have proposed that the initial formation of the massive stars in Carina was itself triggered by external influences. Maps of the molecular gas surrounding the Carina Nebula reveal a CO supershell containing about $8 \times 10^2 M_{\odot}$ of H_2 , the Carina Flare, which appears to be blowing out of the Galactic Plane (Fukui et al. 1999; Dawson et al. 2008a,b; Wunsch et al. 2012). Emission in the 21 cm HI line from the Carina Flare and 10 to 100 μm dust emission also uncover a shell that extends up to 10° above the Galactic plane with a mass of at least $2 \times 10^5 M_{\odot}$. Fukui et al. (1999) propose that energetic feedback inflated a 300×400 pc superbubble that expands with a mean velocity of about 10 km s^{-1} . These authors propose that the Carina Flare was produced by massive stars that formed about 120 pc above the Galactic mid-plane, and that the impact of their energy release may have

triggered star formation in the current Carina Nebula.

6.2. Triggering (or Not)?

There are three main conceptual scenarios that describe how young massive stars affect star formation in their neighborhoods: (1) “pre-existing uncovered” star formation (PRE-SF), where winds and radiation from massive stars evacuate material in the region and reveal stars that have already formed in multiple locations throughout the molecular cloud, (2) “external pressure-induced collapse” of pre-existing clouds that would not otherwise have formed stars in isolation (e.g. induced by radiation, winds, or supernovae; EPIC-SF), and (3) “collect and collapse” star formation (CC-SF), where the external agent is also responsible for forming the parent cloud (see, e.g. Elmegreen & Lada 1977; Bertoldi 1989).

Although our new images of Carina provide a rich harvest of phenomena associated with stars currently forming under the influence of external feedback, the degree to which this star formation activity was actually triggered by that feedback remains quite unclear. This situation echoes many discussions of morphological evidence for triggered star formation in other regions; despite abundant wide-field imaging data, the questions persist and have been debated for decades. Our images show that the Carina Nebula contains dozens of pillars with cometary tails that trail away from Carina’s massive stars, and in nearly all cases there is a young star with an infrared excess embedded at the head of the pillar, sometimes driving an outflow. Although morphologies of this kind have been interpreted as evidence for triggered star formation, this geometry could also arise as winds and radiation from massive stars uncover star formation events that would have occurred anyway in the absence of any triggering effects.

To demonstrate that triggering occurs in any given region is a difficult problem, requiring numerical simulations with multi-dimensional radiation hydrodynamics, and perhaps magnetic fields. Currently, models have not provided decisive observational tests to determine if star formation is triggered based on the morphology of the gas and protostars, and in the absence of such discerning tests, morphology alone as seen in our images cannot be used to support or refute triggering. If future theoretical studies can clarify specific morphologies that are or are not due to triggering, the H₂ images presented here may be quite valuable to address this question.

In the meantime, detailed investigations of age gradients in the stars as compared to gas, as well as star and gas kinematics may be more fruitful avenues to investigate triggering, although we cannot address these with the present dataset. Here too, though, clear

predictions of ages or age-gradients for triggered star formation as opposed to uncovered (and possibly truncated) star formation are not obvious. The upcoming GAIA mission will have 10 to 100 micro-arcsecond proper motion sensitivity, which for Carina and other nearby regions, has the potential to distinguish pre-existing uncovered star formation from triggered star formation, at least among the young stars already exposed at visual wavelengths. Protostars still embedded in Carina’s pillars, young clusters such as the Treasure Chest (Smith et al. 2005), and the driving sources of active outflows such as HH 666 exhibit large infrared excesses, indicating ages less than about 1 Myr. In contrast, the massive stars that have evolved to the LBV or red supergiant phases, and the “naked” portions of clusters such as Tr 15 must be at least 3 Myrs old. But, as noted above, it remains possible that the younger stars and clusters embedded in the surviving molecular clouds of Carina would have formed anyway in the absence of the older generation.

In the case of the Treasure Chest, our H₂ images (Sec. 5; Area 8 of Fig. 4) show an external PDR produced by radiation from the massive stars in the environment, as seen previously, but they also reveal an *internal* PDR that marks the boundary of where the embedded cluster stars dissociate molecules in their natal cloud core. Forming such a structure by triggering is only viable if the lifetime of the core after it is exposed by the triggering event - in this case radiation and winds from the nearby massive stars - is long enough to allow for an entire cluster to form and to create its own internal H II region and PDR. This complex problem should be addressed numerically in light of this observational constraint.

6.3. The Carina Nebula as a Laboratory for PDR Physics

Models of PDRs typically specify the FUV radiation flux G_0 (6 eV - 13.6 eV) and the particle density n , and then track how the molecular, atomic, and ionic elemental abundances vary with depth into the molecular cloud. Most theoretical formalisms use the visual extinction A_V as a convenient independent variable, with the boundary of the H II region at $A_V \lesssim 1$, followed by the PDR at larger A_V . Specific zones exist within a PDR: models show a transition from H to H₂ at $A_V \sim 2$, C⁺ to C and CO at $A_V \sim 4$, and more complex chemistry ongoing at larger depths (Tielens & Hollenbach 1985; Hollenbach et al. 1991).

Models of H II regions require less chemistry, and are correspondingly more sophisticated than their PDR counterparts when it comes to dynamics such as R- and D-fronts (Henney et al. 2005), 3-D capability, magnetic fields, and time-dependence (Arthur et al. 2011), turbulence (Medina et al. 2014), and photoevaporation from pillars (Ercolano et al. 2011). These H II region models also produce synthetic emission-line images that have a direct connection to observations. Merged models of H II regions and PDRs developed by assuming

pressure equilibrium between the PDR and H II region as a first approximation to the dynamics are a relatively recent theoretical development (Abel et al. 2005; Kaufman et al. 2006), and fractal models of PDRs are under development (Andree et al. 2013).

Our observations of H₂ 1-0 S(1), [S II], Br γ and H α probe the boundary between the H II region and the PDR and show clear offsets in the spatial locations of these lines (Fig. 16). While modern PDR models include H₂ (1-0) S1 emission from fluorescent processes, and H II region calculations include Br γ , H α , [S II], and [O III] line cooling, we are not aware of any simulations that predict synthetic emission maps for all these lines in a single simulation, even for a 1-D model. It should be possible to produce such maps for both a planar geometry and pillars with existing codes. For example, motivated by new Spitzer mid-IR spectra, Kaufman et al. (2006) made predictions for rotational H₂ 0-0 lines along with forbidden lines of Si II, Fe II, and C II. Relative to the Spitzer data, our observations give an order-of-magnitude improvement in spatial resolution and reliable photocenter offsets between the H₂, H, and S II lines. Simply predicting photocenter offsets of all the bright emission lines in an H II region/PDR interface in a 1-D model as a function of parameters such as densities, radiation fields, ages, and even magnetic field strengths would be the easiest and most direct comparison with the data in Fig. 16.

7. Summary

We have presented a survey of the H₂ and Br γ emission line sources over a square degree in size centered on the Carina Nebula using the NEWFIRM camera at the CTIO 4-m telescope with total integration times on-source of 12.5 and 8.7 ksec, respectively, and subarcsecond seeing. Our near-IR images are complemented by new narrowband optical images at [O III], H α , and [S II], as well as a suite of broad-band images. The new data clarify the morphologies of irradiated interfaces such as pillars, walls, and globules, identify jets, outflows and flared disks, and provide insights into the star formation activity present within embedded clusters. We also quantified spatial offsets that are present between various emission lines along the irradiated interfaces, and compared each region with existing far-IR and X-ray images.

In many ways, the Carina Nebula is an ideal region to study how massive stars affect their surroundings. The large number of O-stars, combined with relatively low extinction and moderate distance makes it possible to study star formation on a variety of scales. Surveys such as ours provide an overview of the entire region, and also identify specific objects that are worthy of followup with higher-resolution imaging and spectroscopy with HST and ground-based AO systems. The high radiation environment in a region like Carina

in some ways makes it easier to interpret outflows, pillars, and walls because all irradiated dense regions become visible in emission-line images. This advantage is particularly evident in fluorescent lines such as H_2 . However, in some regions projection of multiple irradiated surfaces makes interpretation difficult. Future work centered on time-domain observations such as high-precision proper motions should help to clarify the dynamics of the stars and gas in this remarkable region.

We thank Jacob Palmer for his assistance with the NEWFIRM data acquisition at the 4-m, and the CTIO and NOAO staff for their efforts in getting the instrument operational. Megan Reiter would like to thank Andy Marble for his help generating the jet distribution plot. We thank Bo Reipurth and Chris Davis for quickly providing new HH and MHO object numbers, and an anonymous referee for helpful suggestions regarding the presentation and organization of the paper. The PI was funded by DOE through the NLUF program during the course of this project.

REFERENCES

- Abel, N.P., Ferland, G.J., Shaw, G., & van Hoof, P.A.M. 2005, *ApJS* 161, 65
- Andree, S., Röllig, M., & Ossenkopf, V. 2013, in “New Trends in Radio Astronomy in the ALMA Era”, *ASPC* 476, 311
- Arthur, J. et al. 2011, *MNRAS* 414, 1747
- Ascenso, J., Alves, J., Vicente, S., & Lago, M.T.V.T. 2007, *A&A* 476, 199
- Bally, J., Johnstone, D., Joncas, G., Reipurth, B., & Mallén-Ornelas, G. 2001, *AJ* 122, 1508
- Bally, J., Reipurth, B., Walawender, J., & Armond, T. 2002, *AJ* 124, 2152
- Bertoldi, F. 1989, *ApJ* 346, 735
- Brooks K.J., Burton M.G., Rathborne J.M., Ashley M.C.B., Storey J.W.V. 2000, *MNRAS* 319, 95
- Brooks K.J., Storey J.W.V., Whiteoak J.B. 2001, *MNRAS* 327, 46
- Brooks, K.J, Cox, P., Schneider, N., Storey, J.W.V., Poglitsch, A., Geis, N., & Bronfman, L. 2003, *A&A* 412, 751
- Broos, P.S., et al. 2011, *ApJS* 194, 2
- Davis, C., Gell, R. Khanzadyan, T., Smith, M.D., & Jenness, T. 2010, *A&A* 511, A24
- Dawson, J.R., Kawamura, A., Mizuno, N., Onishi, T., & Fukui, Y. 2008a, *PASJ* 60, 1297
- Dawson, J.R., Mizuno, N., Onishi, T., McClure-Griffiths, N.M., & Fukui, Y. 2008b, *MNRAS* 387, 31
- Donehew, B. & Brittain, S. 2011, *AJ* 141, 46
- Elmegreen, B.G. & Lada, C.J. 1977, *ApJ* 214, 725
- Ercolano, B., Dale, J.E., Gritschneider, M., & Westmoquette, M. 2011, *MNRAS* 420, 141
- Gagne, M. et al. 2011, *ApJS* 194, 5
- Ginsburg, A., Bally, J., & Williams, J.P. 2011, *MNRAS* 418, 2121
- Feigelson, E. et al. 2011, *ApJS* 194, 9

- Feinstein, A., Marraco, H.G., & Muzzio, J.C. 1973, *A&AS* 12, 331
- Foster, J.M., Rosen, P.A., Wilde, B.H., Hartigan, P., and Perry, T.S. 2010, *Phys. Plasmas* 17, 112704
- Fukui, Y., et al. 1999, *PASJ* 51, 751
- Ghosh S.K., Iyengar K.V.K., Rengarajan T.N., Tandon S.N., Verma R.P., & Daniel R.P. 1988, *ApJ* 330, 928
- Grenman, T., & Gahm, G.F. 2014, *A&A* 565, A107
- Hamaguchi, K. et al. 2007 *PASJ* 59, 151
- Hamaguchi, K. et al. 2009 *ApJ* 695, L4
- Hartigan, P., et al. 2011, *ApJ* 736, 29
- Hartigan, P., Palmer, J., & Cleeves, L.I. 2012, *High Energy Density Phys.* 8, 313
- Haro, G. 1952, *ApJ* 115, 572
- Haro, G. 1953, *ApJ* 117, 73
- Harvey P. M., Hoffmann W. F., Campbell M. F., 1979, *ApJ* 227, 114
- Henney, W.J., Arthur, S.J., Williams, R.J.R., & Ferland, G.J. 2005, *ApJ*, 621, 328
- Herbig, G.H. 1950, *ApJ* 111, 11
- Hester, J.J. et al. 1996, *AJ* 111, 2349
- Hollenbach, D.J., Takahashi, T., & Tielens, A.G.G.M. 1991, *ApJ* 377, 192
- Hollenbach, D.J., & Tielens, A.G.G.M. 1997, *ARA&A* 35, 179
- Hur, H., Hwankyung, S., & Bessell, M.S. 2012 *AJ* 143, 41
- Kaufman, M.J., Wolfire, M.G., & Hollenbach, D.J. 2006, *ApJ* 644, 283
- Lee, H.-T., Takami, M., Duan, H.-Y., Karr, J., Su, Y.-N., Liu, S.-Y., Froebrich, D., & Yeh, C.C. 2012, *ApJS* 200, 2
- Lee, H.-T., Liao, W.-T., Froebrich, D., Karr, J., Ioannidis, G., Lee, Y.-H., Su, Y.-N., Liu, S.-Y., Duan, H.-Y., & Takami, M., 2013, *ApJS* 208, 23

- Massey, P., & Johnson, J. 1993, AJ 105, 980
- Meaburn, J., & Walsh, J.R. 1986, MNRAS 220, 745
- Medina, S.-N.X., Arthur, S.J., Henney, W.J., Mellema, G., & Gazol, A. 2014, MNRAS 445, 1797
- Megeath, S.T., Cox, P., Bronfman, L., & Roelfsema, P.R. 1996, A&A 305, 296
- Meynet, G., & Maeder, A. 2003, A&A 404, 975
- Muzerolle, J., Calvet, N., & Hartmann, L. 1998, AJ 116, 2965
- Ngoumou, J., Preibisch, T., Ratzka, T., & Burkert, A. 2013, ApJ 769, 139
- O’Dell, C.R., Wen, Z., & Hu, X. 1993, ApJ 410, 696
- Offner, S., Robitaille, T., Hansen, C.E., McKee, C.F., & Klein, R.I. 2012, ApJ 753, 98
- Ohlendorf, H., Preibisch, T., Gaczkowski, B., Ratzka, T., Grellmann, R., & McLeod, A.M. 2012, A&A 540, A81
- Pekruhl, S., Preibisch, T., Schuller, F., & Menten, K. 2013, A&A 550, A29
- Preibisch, T. et al. 2011a, A&A 530, A34
- Preibisch, T. et al. 2011b, ApJS 194, 10
- Preibisch, T., Schuller, F., Ohlendorf, H., Pekruhl, S., Menten, K., & Zinnecker, H. 2011c, A&A 525, A92
- Preibisch, T. et al. 2011d, A&A 530, A40
- Preibisch, T., Roccatagliata, V., Gaczkowski, B., & Ratzka, T. 2012, A&A 541, A132
- Probst, R.G., et al. 2008, Proc. SPIE 7014, 70142S
- Povich, M.S., et al. 2011, ApJS 194, 14
- Povich, M.S., et al. 2011, ApJS 194, 6
- Rathborne J.M., Burton M.G., Brooks K.J., Cohen M., Ashley M.C.B., Storey J.W.V. 2002, MNRAS 331, 85
- Rathborne, J.M., Brooks, K.M., Burton, M.G., Cohen, M. & Bontemps, S. 2004, A&A 418, 563

- Reed, B.C. 2003, AJ 125, 2531
- Reiter, M., & Smith, N. 2013, MNRAS 433, 2226
- Reiter, M., & Smith, N. 2014, submitted to MNRAS
- Retallack, D.S. 1983, MNRAS 204, 669
- Robitaille, T.P., Whitney, B.A., Indebetouw, R., Wood, K., & Denzmore, P. 2006, ApJS 167, 256
- Robitaille, T.P., Whitney, B.A., Indebetouw, R., & Wood, K. 2007, ApJS 169, 328
- Roccatagliata, V., Preibisch, T., Ratzka, T., & Gaczkowski, B. 2013, A&A 554, A6
- Sanchawala, K. et al. 2007, ApJ 667, 963
- Sanduleak, N. & Stephenson, C.B. 1973, ApJ 185, 899
- Smith, N., Egan, M.P., Carey, S., Price, S.D., Morse, J.A., & Price, P.A. 2000, ApJ 532, 145
- Smith, N., Bally, J., & Brooks, K. J. 2004a, AJ 127, 2793
- Smith, N., Barbá, R.H., & Walborn, N.R. 2004b, MNRAS 351, 1457.
- Smith, N., Stassun, K., & Bally, J. 2005, AJ 129, 888
- Smith, N. 2006a, ApJ 644, 1151
- Smith, N. 2006b, MNRAS 367, 763
- Smith, N., & Brooks, K.J. 2007, MNRAS 379, 1279
- Smith, N., Conti, P.S. 2008, ApJ 679, 1467
- Smith, N., Bally, J., & Walborn, N. 2010a, MNRAS 405, 1153
- Smith, N., et al. 2010b, MNRAS 406, 952
- Stanke, T., McCaughrean, M.J., & Zinnecker, H., 2002, A&A 355, 639
- Stanke, T., McCaughrean, M.J., & Zinnecker, H., 2002, A&A 392, 239
- Tapia, M., Roth, M., Bohigas, J., & Persi, P. 2011, MNRAS 416, 2163
- Tielens, A.G.G.M., & Hollenbach, D.J. 1985, ApJ 291, 722

Townsley, L. et al. 2011, ApJS 194, 1

Walborn, N.R., et al. 2002, AJ 123, 2754

Wang, J. et al. 2011, ApJS 194, 11

Wolk, S.J. et al. 2011, ApJS 194, 12

Wünsch, R., et al. 2012, A&A 539, A116

Yirak, K. et al. 2013, High Energy Density Phys. 9, 251

Yonekura, Y., Asayama, S., Kimura, K., Ogawa, H., Kanai, Y., Yamaguchi, N., Barnes, P.J.,
& Fukui, Y. 2005, ApJ 634, 476

Zacharias, N., Finch, C.T., Girard, T.M., Henden, A., Bartlett, J.L., Monet, D.G., &
Zacharias, M.I. 2013, AJ 145, 44

Table 1. Summary of Carina Mosaics

Date	Filter	Exposure Time (ks) ^a	FWHM (arcsec) ^b	Camera
9-10 Mar 2003	[O III] 5007Å	0.60	0.8	Mosaic
9-10 Mar 2003	H α 6563Å	0.60	0.8	Mosaic
9-10 Mar 2003	[S II] 6720Å	0.60	0.8	Mosaic
9-10 Mar 2003	I 0.9 μ m	0.06	0.8	Mosaic
13-16 Mar 2011	H2 2.12 μ m	12.5	0.7	Newfirm
14-17 Mar 2011	Br γ 2.16 μ m	8.7	0.8	Newfirm
9-18 Mar 2011	K 2.2 μ m		0.7 – 2.2	Newfirm
21-22 Jan, 13 Jun, 17 Jul 2005	3.6 μ m	0.032	\sim 2	Spitzer
21-22 Jan, 13 Jun, 17 Jul 2005	4.5 μ m	0.032	\sim 2	Spitzer
21-22 Jan, 13 Jun, 17 Jul 2005	5.8 μ m	0.032	\sim 2	Spitzer
21-22 Jan, 13 Jun, 17 Jul 2005	8.0 μ m	0.032	\sim 2	Spitzer

^aTypical exposure time at center of mosaic

^bImage quality of final coadded mosaic

Table 2. Coordinates for images

Object	α (2000)	δ (2000)	Figure	Notes
Area 1 center	10:45:22.07	-59:58:48	3	
Area 2 center	10:45:58.27	-60:06:30	3	
Area 3 center	10:43:50.16	-59:57:38	3	
Area 4 center	10:44:41.04	-59:57:37	3	
Area 5 center	10:47:07.56	-60:02:15	3	
Area 6 center	10:45:13.57	-60:02:51	4	
Area 7 center	10:44:03.21	-60:07:00	4	
Area 8 center	10:45:52.71	-59:58:40	4	
Area 8 inset	10:45:53.73	-59:57:02	4	
Area 9 center	10:45:01.54	-59:47:43	5	
Area 10 center	10:46:03.19	-59:44:42	5	
Area 11 center	10:45:24.30	-59:45:37	6	
Area 12 center	10:45:28.92	-59:53:37	6	
Area 13 center	10:46:05.22	-59:33:46	6	
Area 14 center	10:47:00.47	-59:37:49	6	
Area 15 center	10:47:04.49	-59:51:43	7	
Area 16 center	10:45:58.82	-59:12:50	8	
Area 17 center	10:46:18.41	-59:14:27	8	
Area 18 center	10:45:31.98	-59:12:23	8	
Area 19 center	10:44:07.69	-59:08:58	8	
Area 20 center	10:45:00.73	-59:21:60	8	
Area 21 center	10:45:15.82	-59:27:31	9	
Area 22 center	10:44:01.97	-59:18:00	9	
Area 23 center	10:44:47.22	-59:27:21	10	
Area 24 center	10:44:19.45	-59:25:44	10	
Area 25 center	10:44:22.42	-59:27:53	10	
Area 26 center	10:44:04.15	-59:33:42	10	
Area 27 center	10:43:30.73	-59:27:45	10	
Area 28 center	10:44:33.88	-59:34:57	10	
Area 29 center	10:43:58.22	-59:29:44	10	
Area 30 center	10:44:59.42	-59:31:19	10	
Area 31 center	10:43:38.38	-59:33:18	10	
Area 32 center	10:43:49.54	-59:37:40	10	
Area 33 center	10:44:26.54	-59:32:43	10	
Area 34 center	10:45:07.60	-59:39:17	11	
Area 35 center	10:44:48.08	-59:37:39	11	
Area 36 center	10:44:50.97	-59:40:55	11	
Area 37 center	10:44:31.44	-59:39:21	11	
Area 38 center	10:45:12.50	-59:37:41	11	
Area 39 center	10:44:43.02	-59:44:03	11	
Area 40 center	10:44:03.17	-59:40:42	11	
Area 41 center	10:44:21.10	-59:42:04	11	
Area 42 center	10:45:32.65	-59:37:41	11	
Area 43 center	10:43:41.47	-59:41:45	11	
Area 44 center	10:41:39.21	-59:43:33	12	
Area 45 center	10:41:20.69	-59:48:23	12	

Table 2—Continued

Object	α (2000)	δ (2000)	Figure	Notes
Area 46 center	10:42:43.72	-59:36:02	12	
Area 47 center	10:41:35.31	-59:35:07	12	
Area 48 center	10:42:12.15	-59:35:30	12	
Area 49 center	10:41:54.01	-59:37:59	12	
Area 50 center	10:43:13.16	-59:37:24	12	
Area 51 center	10:42:50.33	-59:31:43	13	
Area 52 center	10:42:36.51	-59:26:22	13	
Area 53 center	10:43:05.53	-59:32:36	13	
Area 54 center	10:43:20.57	-59:31:05	13	
Area 55 center	10:42:58.29	-59:17:25	13	
Area 56 center	10:42:09.74	-59:32:52	13	
Area 57 center	10:43:10.69	-59:24:44	13	
Area 58 center	10:41:12.93	-59:32:43	13	
Area 59 center	10:43:07.04	-59:29:04	13	
Area 60 center	10:42:10.27	-59:20:24	13	
Area 61 center	10:43:26.00	-59:34:45	14	
Area 62 center	10:43:17.13	-60:02:51	33	
Area 63 center	10:41:20.90	-60:08:18	33	
New Candidate Flows and Associated Objects				
HH 1123 A	10:40:03.82	-60:05:43.1	23	H α , [S II]
HH 1123 B	10:40:03.57	-60:05:44.9	23	H α , [S II]
HH 1123 C	10:40:04.07	-60:05:46.8	23	H α , [S II]
HH 1123 D	10:40:03.66	-60:05:49.8	23	H α , [S II]
HH 1124 PCYC 884	10:45:28.53	-59:13:18.8	24	Star
HH 1124 PCYC 889	10:45:29.01	-59:13:19.5	24	Star
HH 1124 IRS1	10:45:29.84	-59:13:16.1	24	Star
HH 1124 IRS2	10:45:29.54	-59:13:21.0	24	Star
HH 1124 A	10:45:31.39	-59:13:26.6	24	H α , [S II]
HH 1124 B	10:45:30.83	-59:13:26.4	24	H α , [S II]
HH 1124 C	10:45:29.07	-59:13:22.3	24	H α , [S II]
HH 1124 D	10:45:26.17	-59:12:44.0	24	H α , [S II]
HH 1124 E	10:45:24.60	-59:11:54.9	24	H α , [S II]
HH 1125 A	10:43:04.18	-59:55:01.2	25	[S II]
HH 1125 B	10:43:00.44	-59:54:52.4	25	[S II]
HHc-21 Star	10:44:10.20	-59:08:06.5	32	
MHO 1605 center	10:43:51.48	-59:39:11.0	10	H $_2$, [S II]
IRS 902	10:44:31.09	-59:33:09.6	10	‘Disk Object’
MHO 1606	10:44:22.67	-59:33:53.6	10	H $_2$, [S II]
MHO 1607	10:44:28.48	-59:32:45.5	10	H $_2$, east knot
MHO 1608	10:44:29.12	-59:32:42.6	10	H $_2$
MHO 1609a	10:45:09.89	-60:02:25.8	27, 4	H $_2$, H α , [S II]
MHO 1609b	10:45:10.21	-60:02:34.1	27, 4	H $_2$, H α , [S II]
MHO 1610	10:46:08.45	-59:45:23.8	28	H $_2$
MHO 1610 IRS	10:46:07.72	-59:45:26.6	28	Br γ , H $_2$
MHO 1611 a	10:42:48.31	-59:25:42.1	29	H $_2$
MHO 1611 b	10:42:47.10	-59:25:42.8	29	H $_2$

Table 2—Continued

Object	α (2000)	δ (2000)	Figure	Notes
MHO 1611 c	10:42:48.04	–59:25:47.3	29	H ₂
MHO 1611 d	10:42:47.86	–59:25:52.1	29	H ₂
MHO 1611 e	10:42:47.73	–59:26:01.8	29	H ₂
MHO 1611 f	10:42:47.36	–59:26:07.8	29	H ₂
MHO 1611 g	10:42:46.94	–59:26:13.6	29	H ₂
MHO 1611 h	10:42:45.09	–59:26:24.8	29	H ₂
MHO 1611 i	10:42:46.11	–59:26:29.1	29	H ₂
MHO 1611 j	10:42:45.54	–59:26:43.6	29	H ₂
MHO 1612 a	10:42:45.95	–59:25:21.8	29	H ₂
MHO 1612 b	10:42:45.79	–59:25:17.7	29	H ₂
MHO 1612 c	10:42:45.43	–59:25:15.8	29	H ₂
MHO 1612 d	10:42:45.11	–59:25:10.4	29	H ₂
MHO 1613	10:42:46.99	–59:25:21.1	29	H ₂
MHO 1614 a	10:42:49.40	–59:25:29.6	29	H ₂
MHO 1614 b	10:42:48.68	–59:25:27.9	29	H ₂
MHO 1615 a	10:42:47.28	–59:25:30.4	29	H ₂
MHO 1615 b	10:42:46.52	–59:25:29.4	29	H ₂
MHO 1616 a	10:43:09.13	–59:24:24.7	13	H ₂
MHO 1616 b	10:43:09.40	–59:24:26.9	13	H ₂
MHO 1616 c	10:43:10.30	–59:24:37.9	13	H ₂
MHO 1616 d	10:43:11.30	–59:24:46.9	13	H ₂
MHO 1616 e	10:43:11.50	–59:24:48.2	13	H ₂
MHO 1616 f	10:43:12.70	–59:24:59.5	13	H ₂
MHO 1616 g	10:43:12.95	–59:25:01.5	13	H ₂
MHO 1617	10:43:10.22	–59:24:53.1	13	H ₂
MHO 1617 IR	10:43:09.68	–59:24:58.8	13	H ₂
MHO 1618 IR	10:45:28.63	–59:47:55.1	30	H ₂
MHO 1618 a	10:45:26.59	–59:47:32.6	30	H ₂
MHO 1618 b	10:45:28.31	–59:47:51.2	30	H ₂
MHO 1618 c	10:45:28.81	–59:47:58.5	30	H ₂
MHO 1618 d	10:45:28.98	–59:48:04.4	30	H ₂
MHO 1619 a	10:46:10.50	–59:33:17.9	31	H ₂
MHO 1619 b	10:46:10.49	–59:33:21.6	31	H ₂
MHO 1619 c	10:46:10.29	–59:33:22.4	31	H ₂
MHO 1620 a	10:46:11.47	–59:33:30.6	31	H ₂ , [S II]
MHO 1620 b	10:46:11.99	–59:33:30.3	31	H ₂
MHO 1620 c	10:46:12.73	–59:33:31.4	31	H ₂
MHO 1620 d	10:46:13.19	–59:33:28.4	31	H ₂
MHO 1620 e	10:46:13.56	–59:33:29.6	31	H ₂
MHO 1620 f	10:46:14.03	–59:33:29.2	31	H ₂
MHO 1621 a	10:46:12.96	–59:33:35.5	31	H ₂
MHO 1621 b	10:46:13.18	–59:33:36.6	31	H ₂
MHO 1621 c	10:46:13.43	–59:33:39.3	31	H ₂
MHO 1621 d	10:46:13.62	–59:33:36.9	31	H ₂
MHO 1621 e	10:46:13.86	–59:33:34.5	31	H ₂
PCYC 438	10:44:07.03	–59:08:39.1	32	Star

Table 2—Continued

Object	α (2000)	δ (2000)	Figure	Notes
MHO 1622 a	10:43:53.18	–59:09:02.5	32	H ₂
MHO 1622 b	10:43:53.84	–59:09:05.4	32	H ₂
MHO 1623 a	10:43:54.96	–59:07:52.8	32	H ₂
MHO 1623 b	10:43:55.24	–59:07:55.8	32	H ₂
MHO 1623 c	10:43:56.58	–59:08:07.0	32	H ₂
MHO 1623 d	10:43:57.28	–59:08:18.1	32	H ₂
MHO 1624 a	10:44:01.93	–59:08:53.0	32	H ₂
MHO 1624 b	10:44:03.13	–59:08:51.0	32	H ₂
MHO 1624 c	10:44:04.31	–59:08:51.6	32	H ₂
MHO 1625 a	10:44:08.49	–59:09:03.0	32	H ₂
MHO 1625 b	10:44:08.31	–59:09:08.6	32	H ₂
MHO 1625 c	10:44:09.07	–59:09:03.9	32	H ₂
MHO 1626 a	10:44:08.35	–59:09:25.9	32	H ₂
MHO 1626 b	10:44:09.14	–59:09:26.4	32	H ₂
MHO 1626 c	10:44:10.36	–59:09:30.0	32	H ₂
R1	10:44:21.6	–59:08:24	32	H ₂ , [S II], H α
R2	10:44:11.0	–59:08:26	32	H ₂ , [S II], H α
R3	10:44:11.5	–59:07:31	32	H ₂ , [S II], H α
R4	10:44:05.1	–59:07:42	32	H α
R5	10:43:58.0	–59:08:02	32	H ₂ , [S II], H α
MHO 1627 a	10:41:14.63	–59:32:49.9	13	H ₂
MHO 1627 b	10:41:14.77	–59:32:58.7	13	H ₂
MHO 1627 c	10:41:15.29	–59:33:16.3	13	H ₂
MHO 1628 a	10:41:14.15	–59:32:35.9	13	H ₂
MHO 1628 b	10:41:14.16	–59:32:38.2	13	H ₂
PN Candidate	10:43:34.77	–59:42:01.5	11	H ₂
Finger IRS	10:44:30.16	–59:38:40.4	35	Star
SW Loop A	10:40:16.26	–60:17:09.7	34	H α , Northern knot of arc
SW Loop B	10:40:12.91	–60:16:44.7	34	H α , Center of diffuse area
SW Loop C	10:40:05.30	–60:16:14.4	34	H α , Brightest knot
SW Loop D	10:40:00.20	–60:16:12.9	34	H α , Diffuse structure
SW Loop E	10:39:52.62	–60:16:17.0	34	H α , Middle of a bright arc
SW Loop F	10:39:53.64	–60:14:09.9	34	H α
SW Loop G	10:39:47.60	–60:12:20.3	34	H α

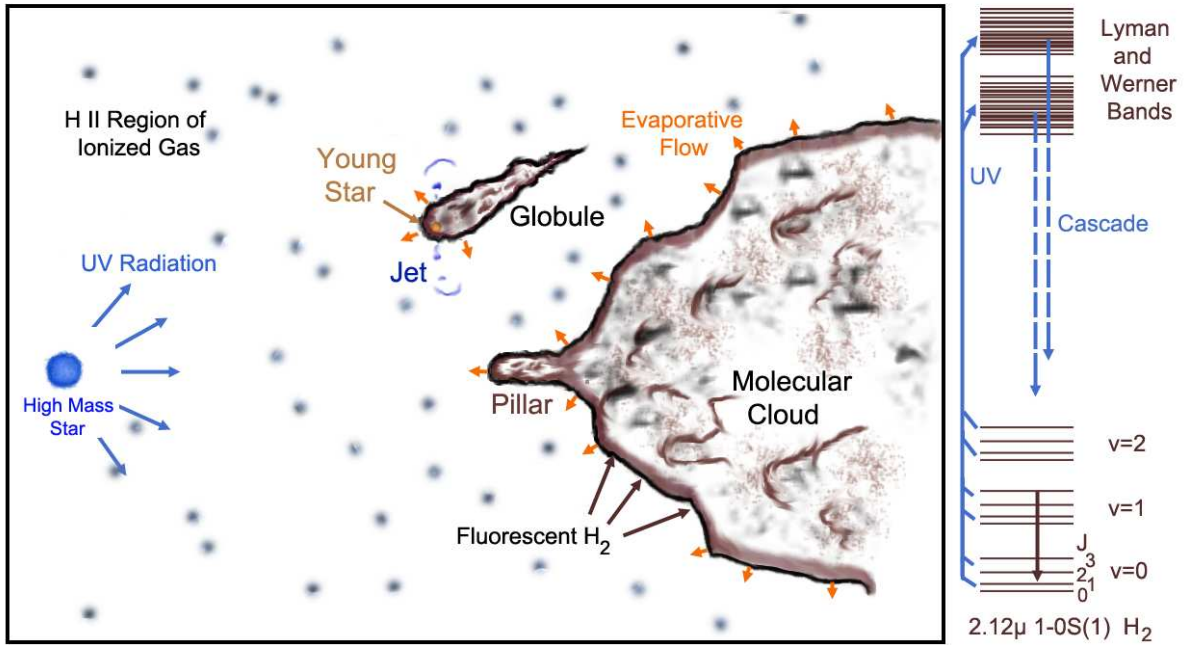


Fig. 1.— Schematic of a photodissociation region. Ultraviolet radiation from an O-star excites H₂ at the interface between an ambient molecular cloud and the H II region, and the molecule emits 2.12μm line radiation as it transitions to the ground state. Recombination lines of Hα and Brγ form throughout the H II region, and are enhanced as H in the dense photoevaporative flow becomes ionized. Globules and pillars form in response to the radiation. Jets from young stars create shock fronts that radiate permitted and forbidden line radiation, and may also excite the 2.12μm lines of H₂ if molecules are present within or alongside the jet.

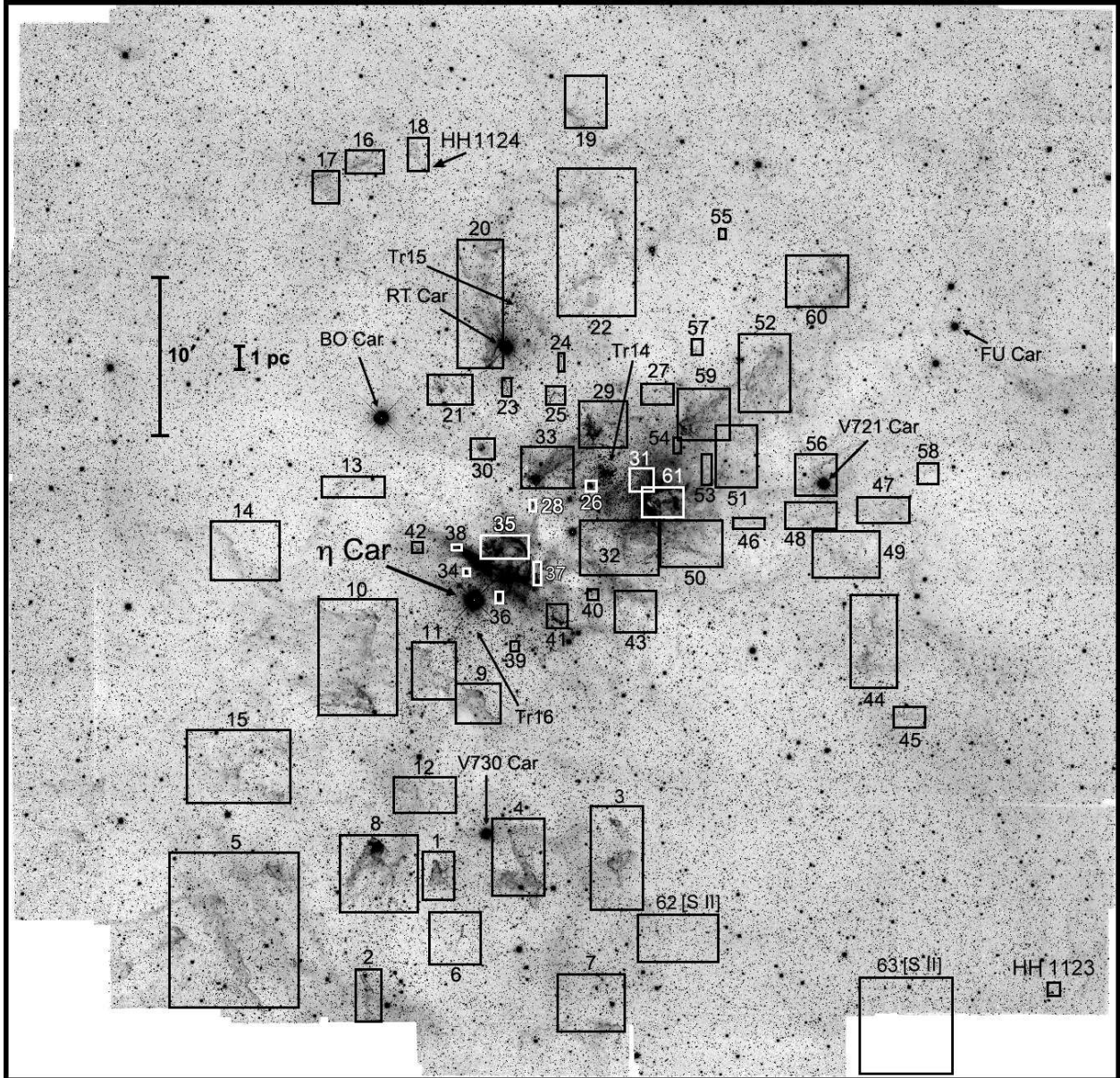


Fig. 2.— Overview of the Carina region in H_2 2.12 μ m. Numbered boxes mark the regions of H_2 emission highlighted in Fig. 3. The scale bar assumes a distance of 2.3 kpc. Coordinates for the centers of each box are compiled in Table 2. The clusters Tr 14, Tr 15, Tr 16, and the brightest stars are marked. The image spans ~ 1.1 degrees on a side, with a scale of 0.4 arcseconds per pixel. North is up and east to the left in this and subsequent images.

Southern Pillars

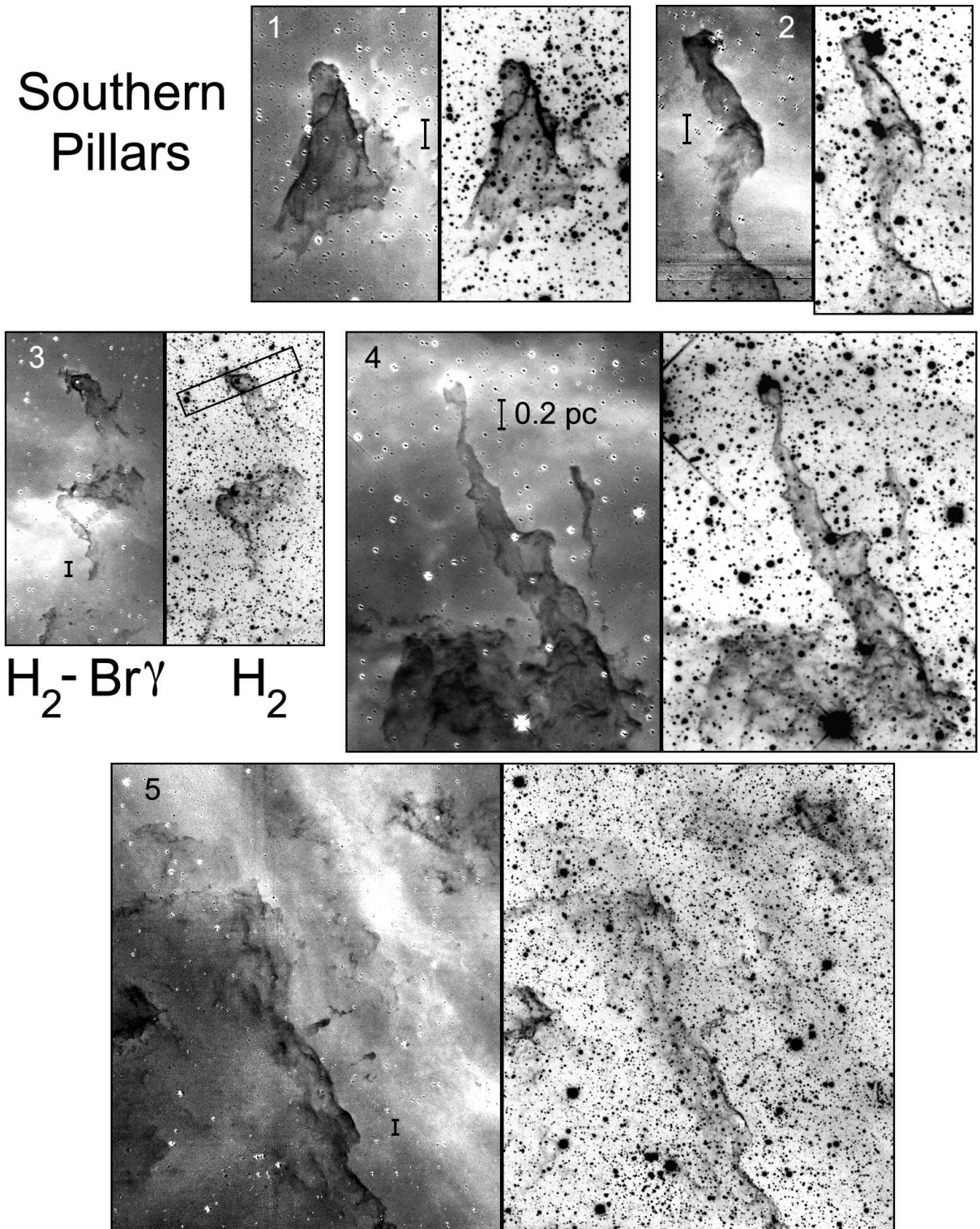


Fig. 3.— The Southern Pillars of H₂ emission in Carina. Numbers refer to the Areas 1 – 5 marked in Fig 2. Right: H₂ 2.12 μm image, Left: Difference image of H₂ – Br γ, with Br γ emission relatively brighter where the image is white, and H₂ relatively brighter where the image is black. The scale bar of 0.2 pc corresponds to a distance of 2.3 kpc. The rectangle in Area 3 denotes the region covered in Fig. 18.

Southern Pillars (cont.)

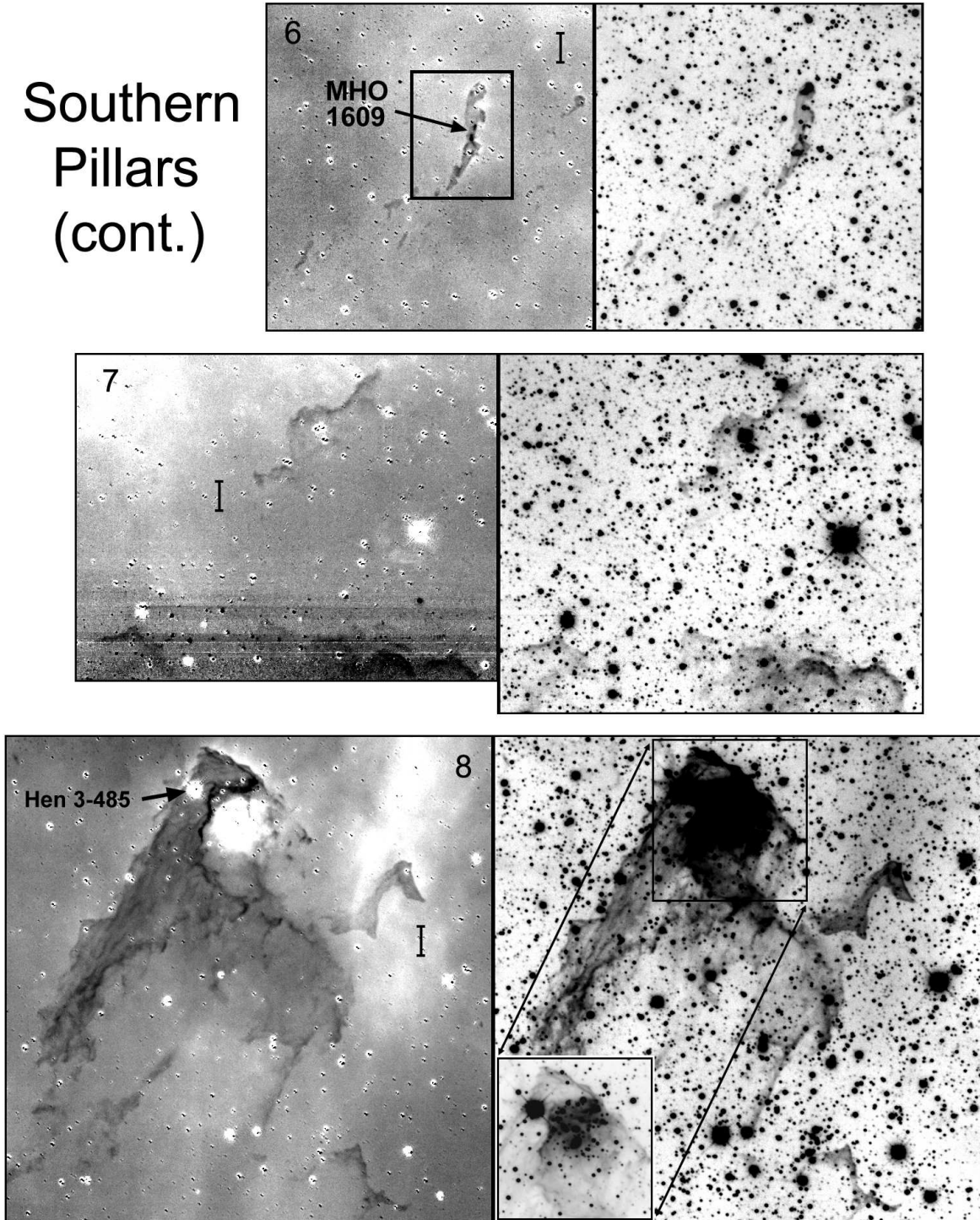


Fig. 4.— Same as Fig. 3 for additional Southern Pillars of H_2 emission in the Carina Nebula. Numbers refer to the Area 6 – 8 marked in Fig. 2. The MHO 1609 region is expanded in Fig. 27. The inset in Area 8 is the embedded cluster known as the Treasure Chest.

Eastern Walls

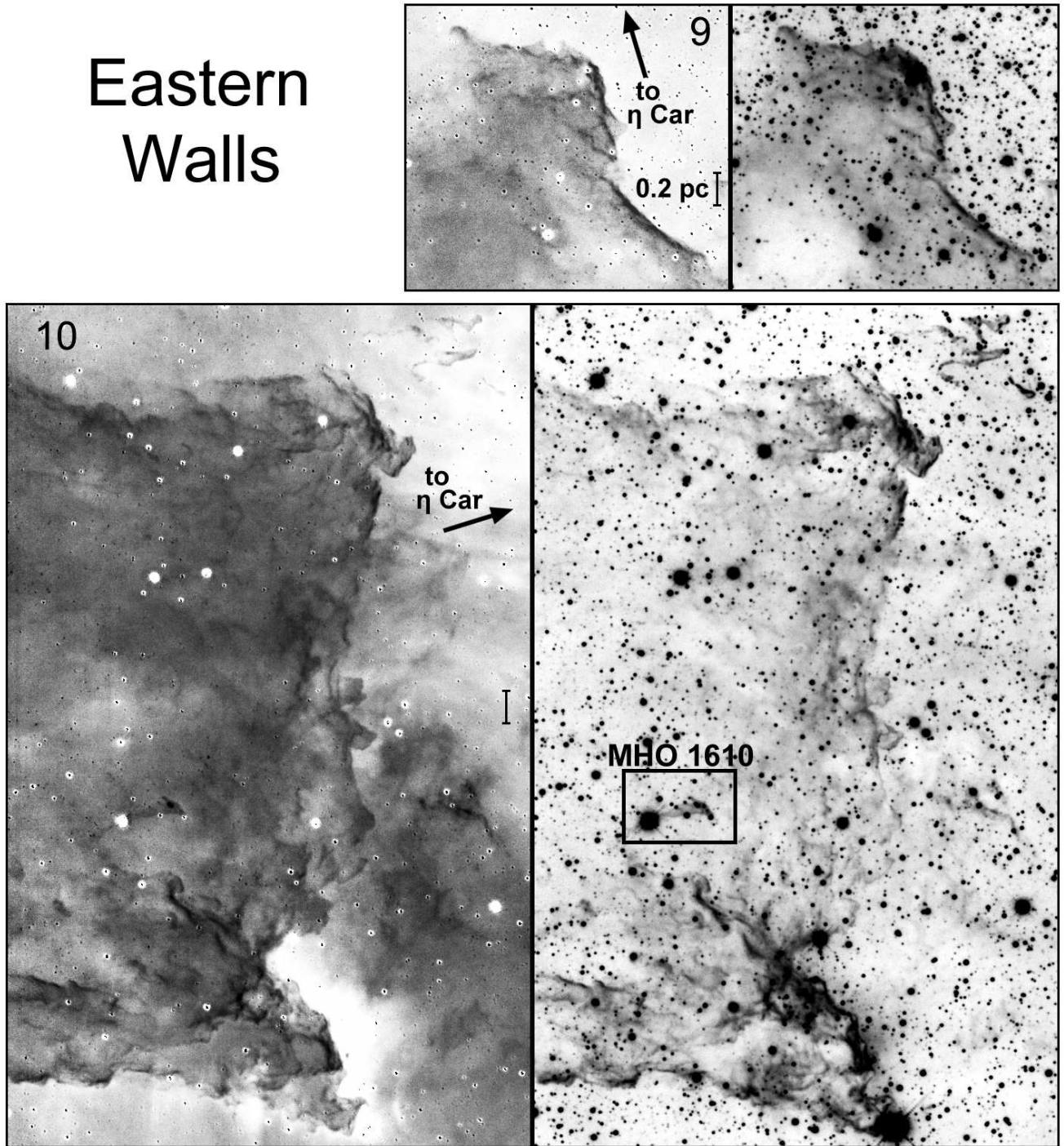


Fig. 5.— Same as Fig. 3 but for Areas 9 and 10 of the Eastern Walls in Fig 2. The boxed region surrounding MHO 1610 is enlarged in Fig. 28.

Eastern Walls (cont.)

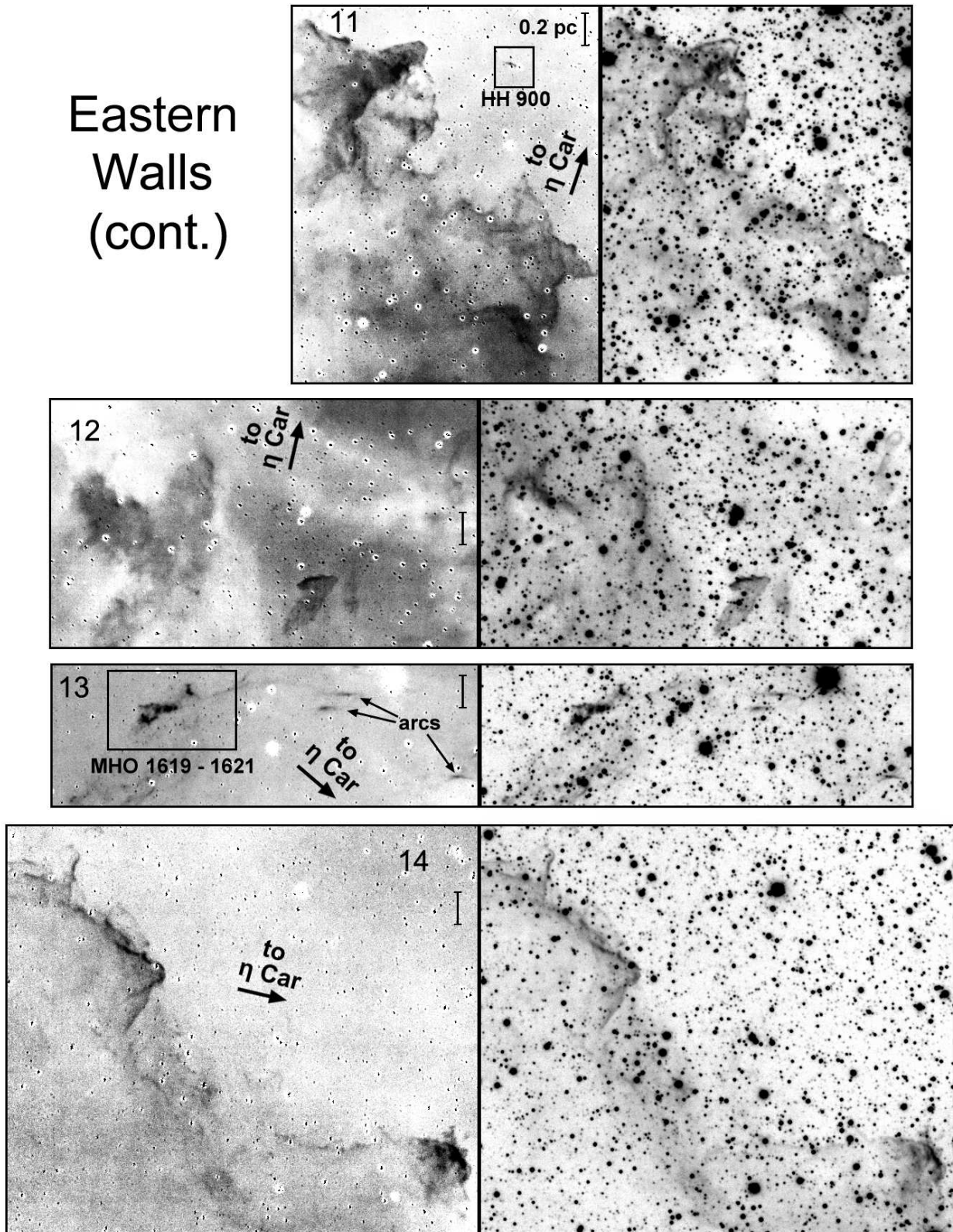


Fig. 6.— Same as Fig. 3 but for Areas 11 through 14 of the Eastern Walls in Fig. 2. The small boxed region in Area 11 is HH 900, reproduced in Fig. 19, and MHO 1619 – MHO 1621 in Area 13 is expanded in Fig. 31. The direction to η Car is shown.

Eastern Walls (cont.)

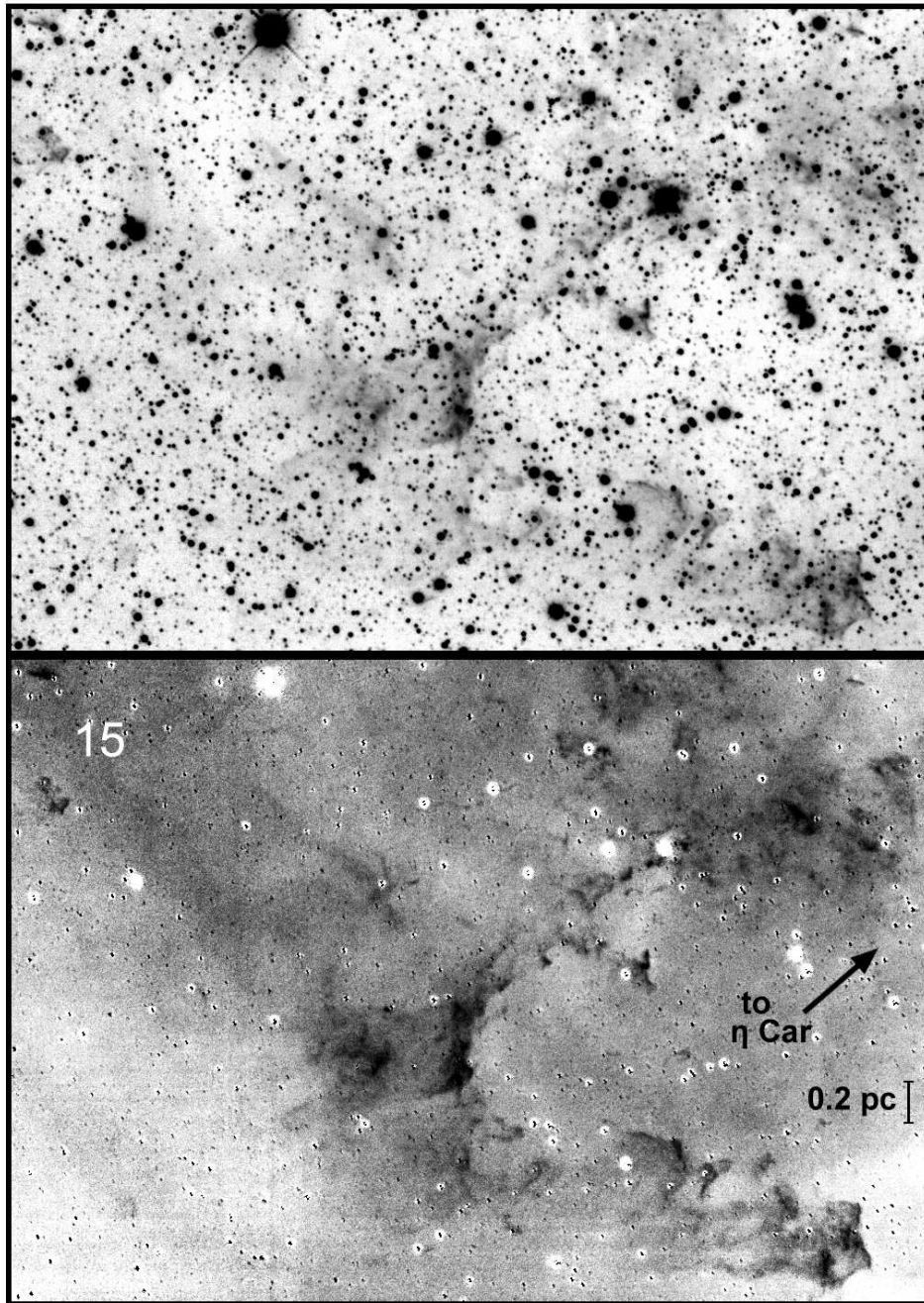


Fig. 7.— Same as Fig. 3 but for Area 15 of the Eastern Walls in Fig 2. The H₂ image is at top with the difference image below it.

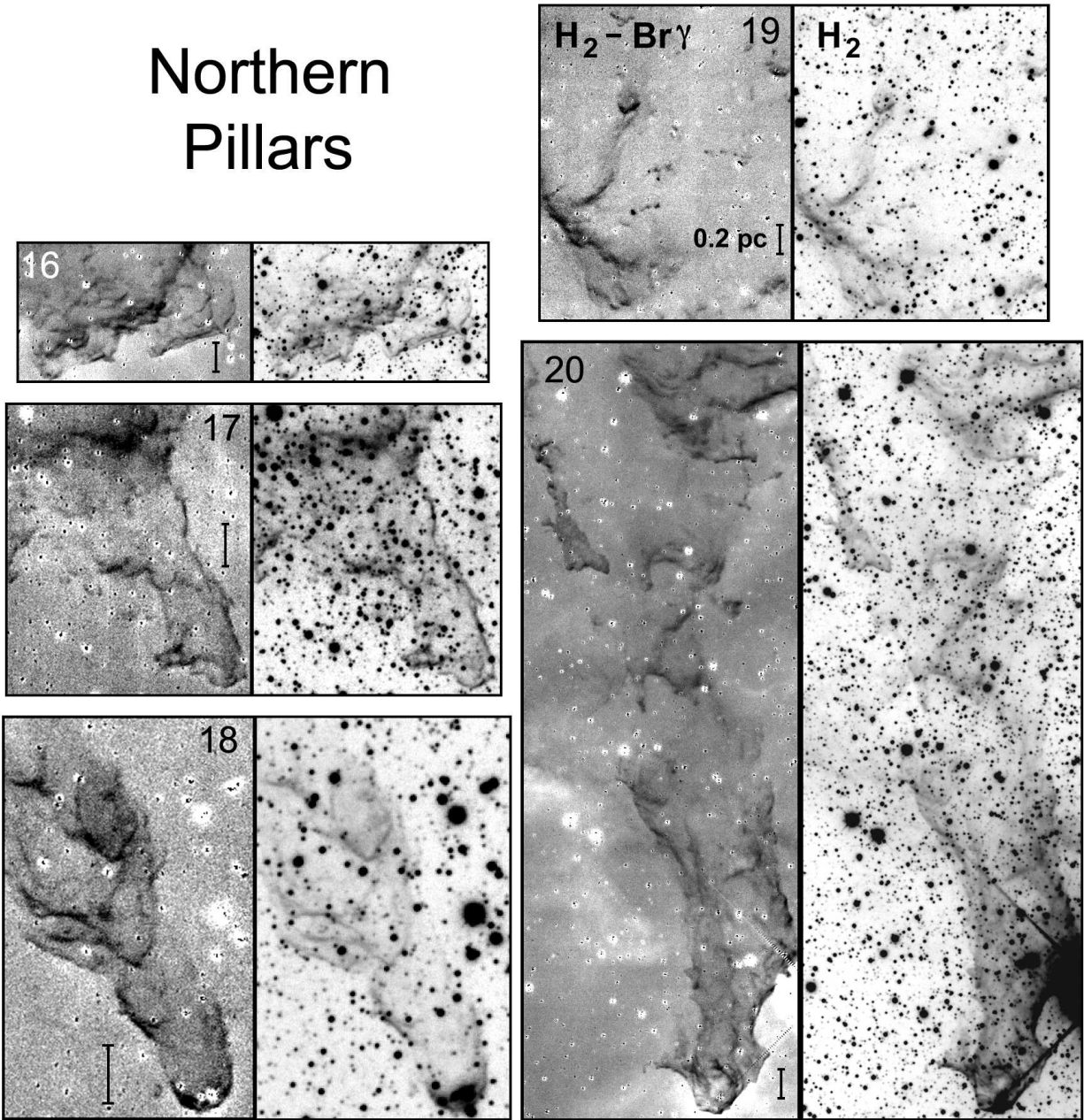


Fig. 8.— Same as Fig. 3 but for Areas 16 through 20 of the Northern Pillars in Fig 2. Fig. 32 presents an expanded version of the MHO objects in Area 19.

Northern
Pillars
(cont.)

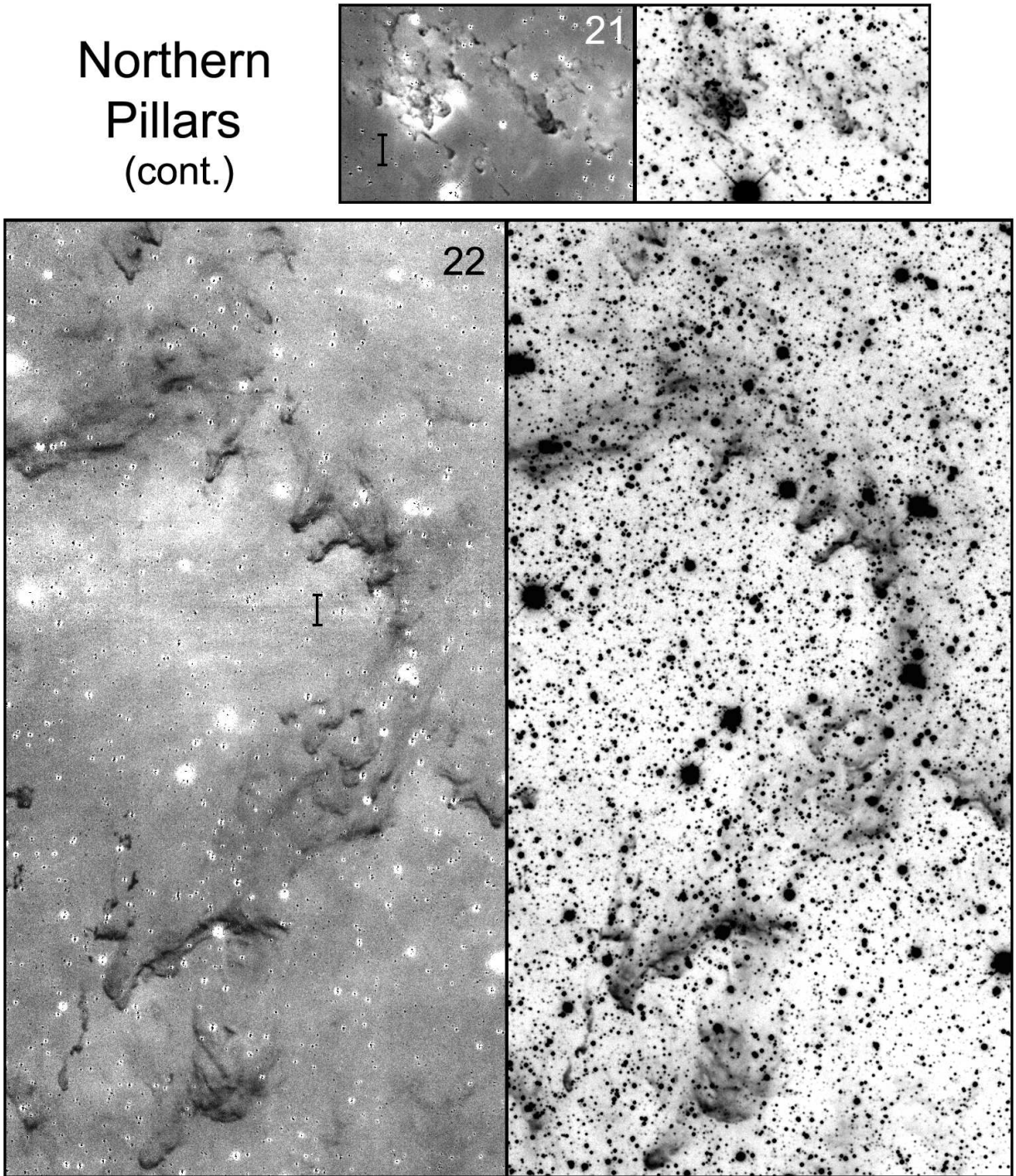


Fig. 9.— Same as Fig. 3 but for Areas 21 and 22 of the Northern Pillars in Fig 2.

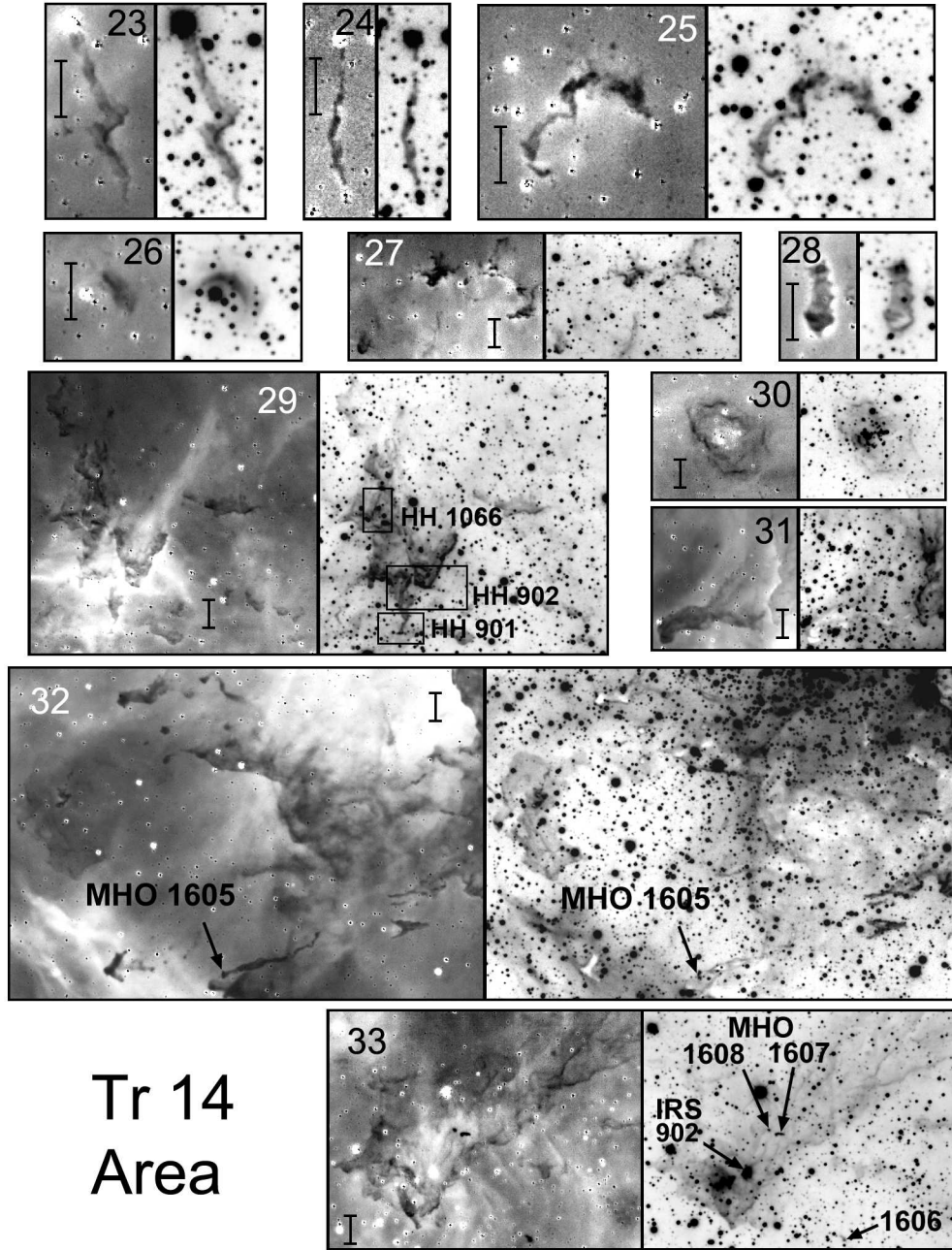


Fig. 10.— Same as Fig. 3 but for Areas 23 through 33 of the Trumpler 14 region in Fig 2. Boxes around HH 901, HH 902, and HH 1066 are expanded in Figs. 20, 21, and 22, respectively. The MHO objects in Areas 32 and 33 are discussed in the text.

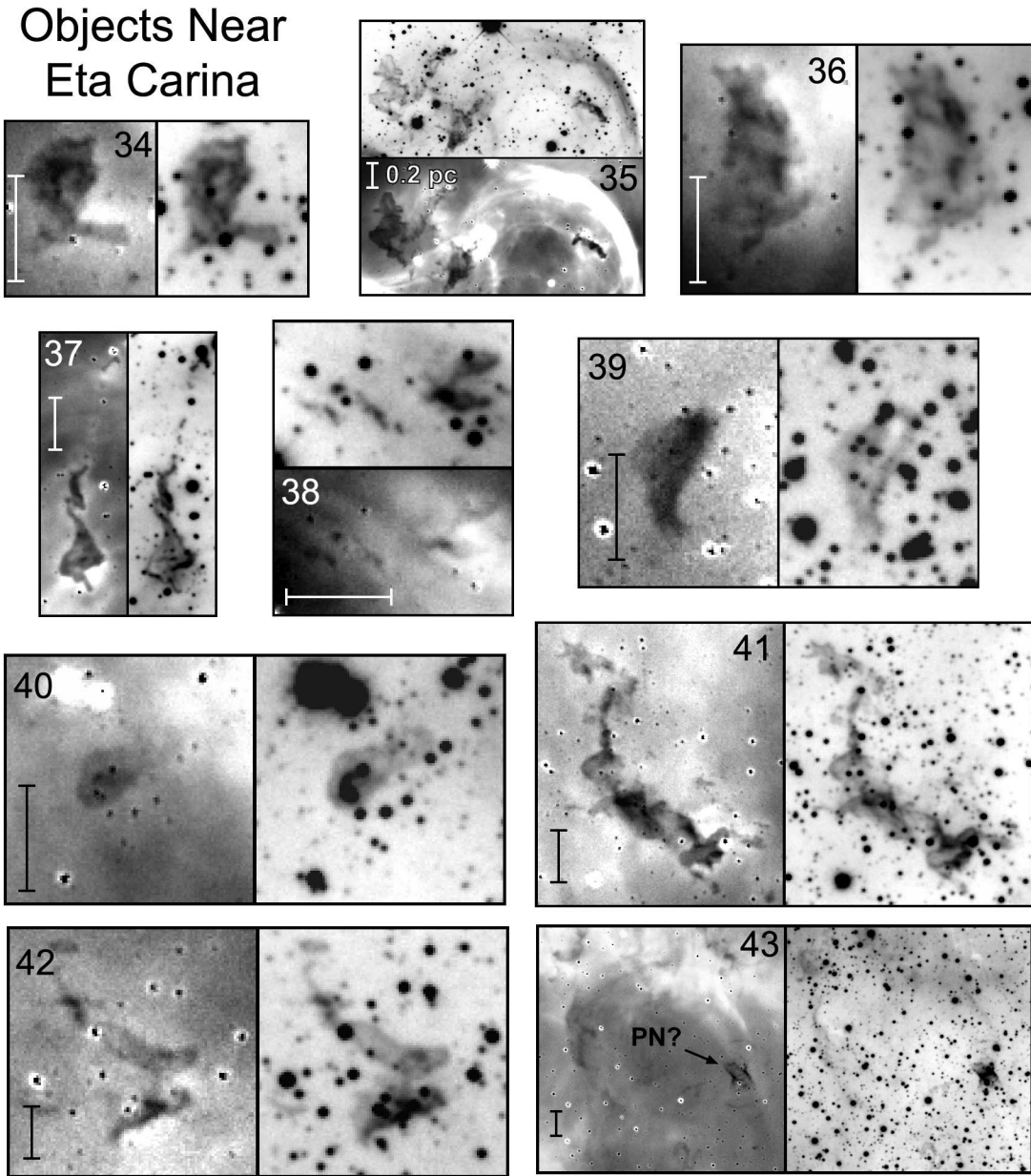


Fig. 11.— Same as Fig. 3 but for Areas 34 through 43 in the vicinity of η Car in Fig 2. The nebulous object on the right side of Area 43 is a candidate planetary nebula.

Southwestern Pillars and Walls

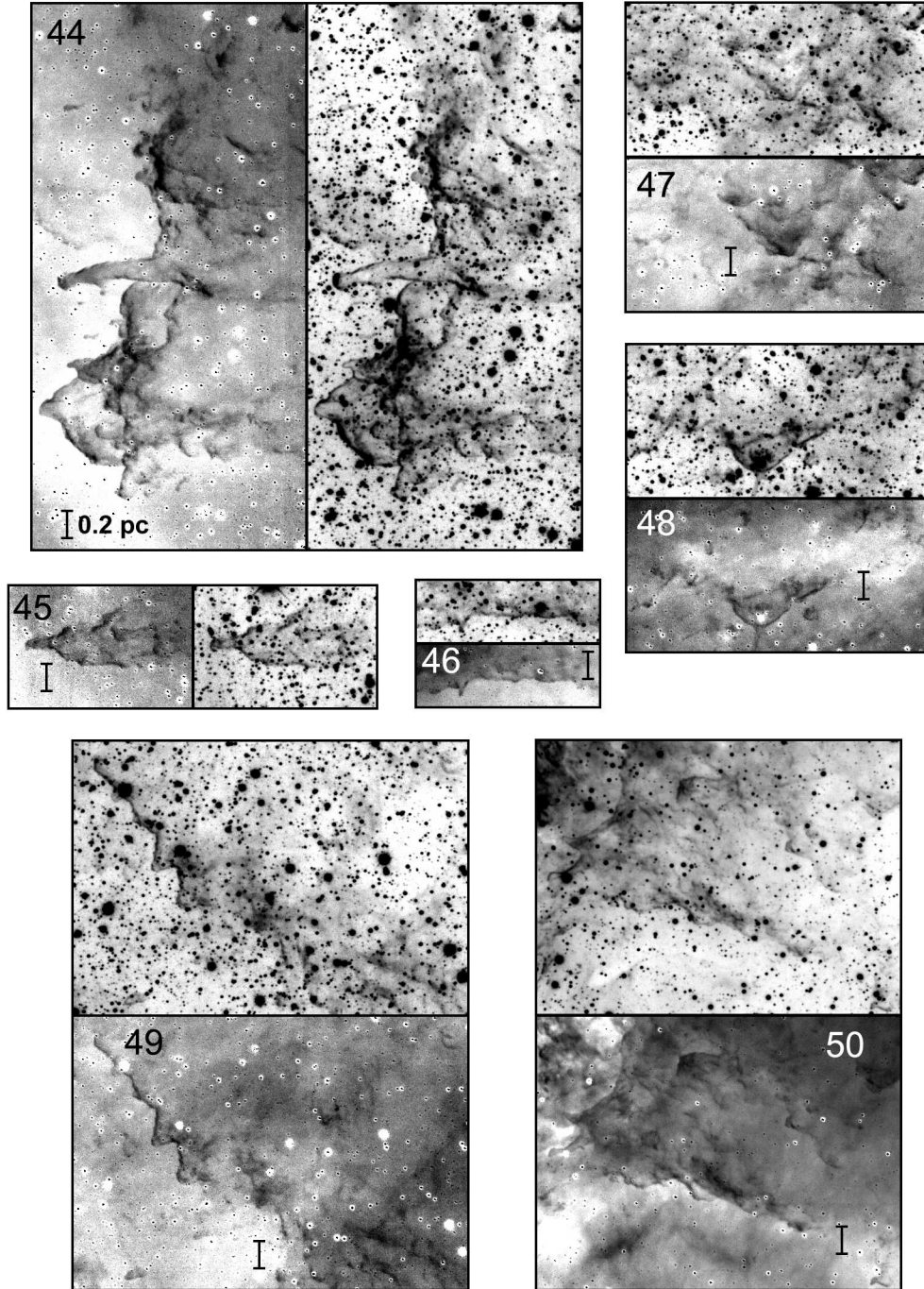


Fig. 12.— Same as Fig. 3 but for Areas 44 through 50 of the Southwestern Pillars and Walls in Fig 2. The H_2 images are at the top or right in each panel, with the $H_2 - Br\gamma$ images at bottom or left.

Northwestern Pillars, Walls, and Jets

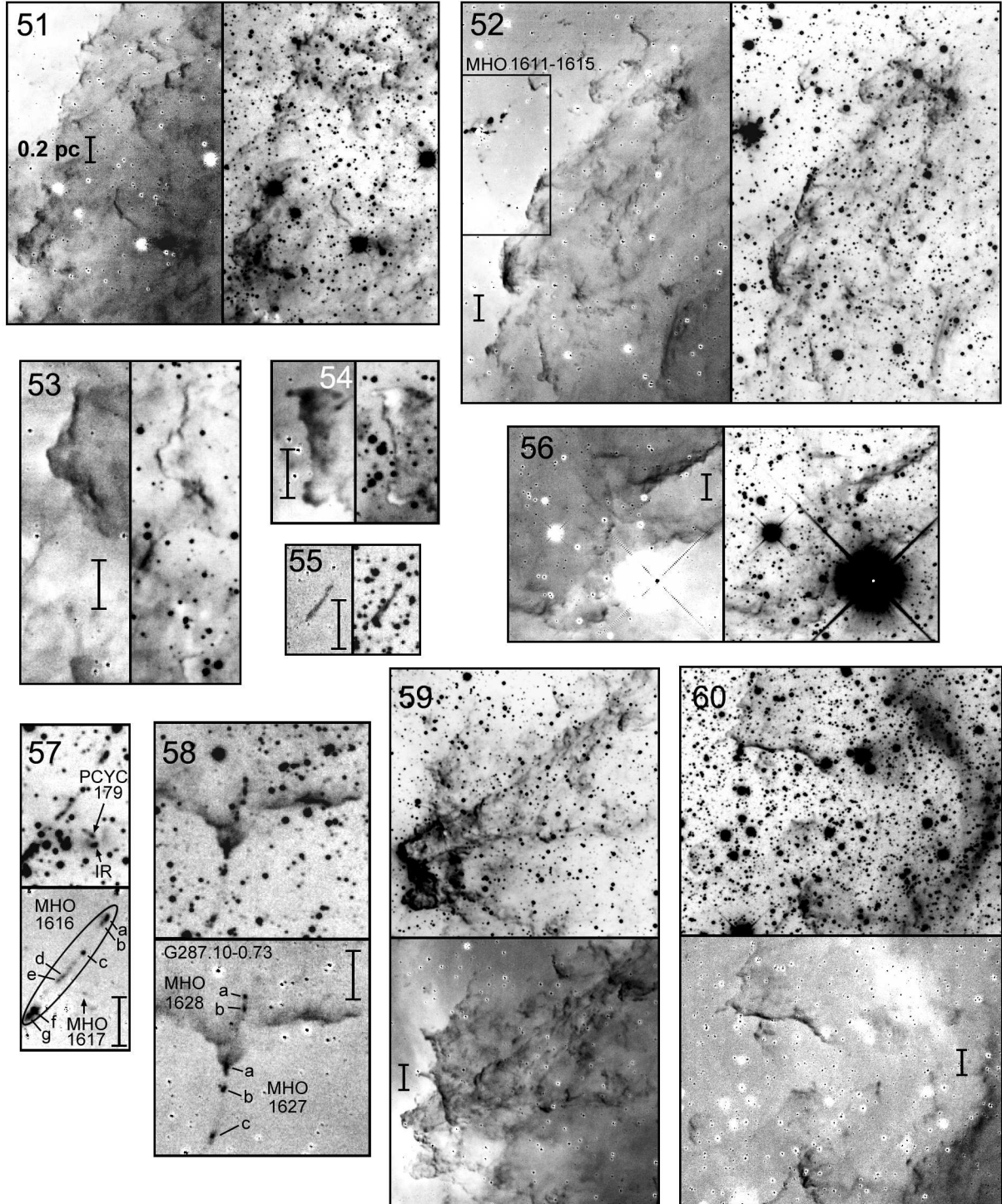


Fig. 13.— Same as Fig. 3 but for Areas 51 through 60 of the Northwestern Pillars, Walls and Jets in Fig. 2. The H_2 images are at the top or right in each panel, with the $H_2 - Br\gamma$ images at bottom or left. The region marked in Area 52 is expanded in Fig. 29.

Western Wall

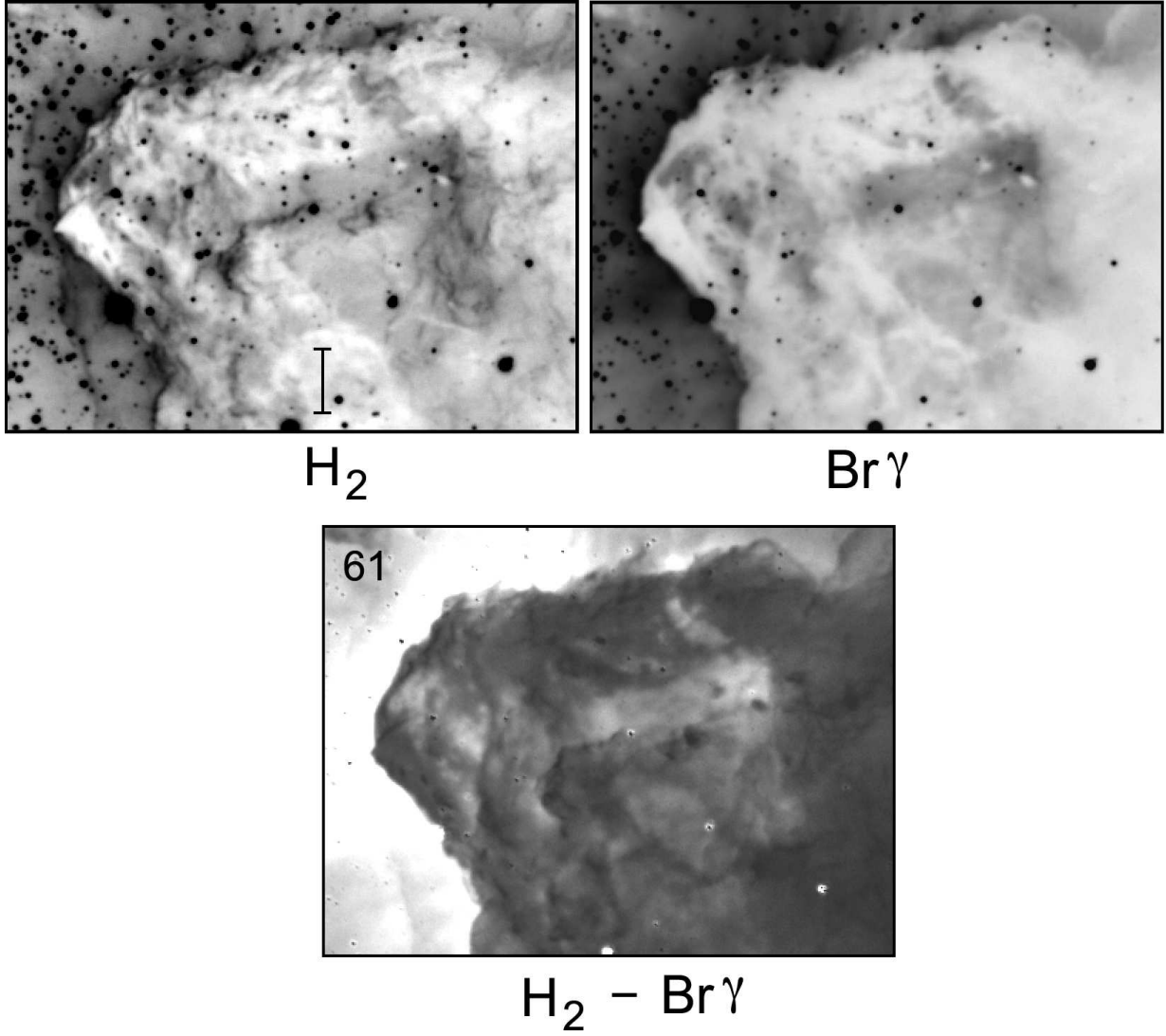


Fig. 14.— Same as Fig. 3 but for Area 61 (G287.38-0.62), the Western Wall in Fig 2. The H_2 and $Br\gamma$ images are at the top, with the $H_2 - Br\gamma$ images at bottom.

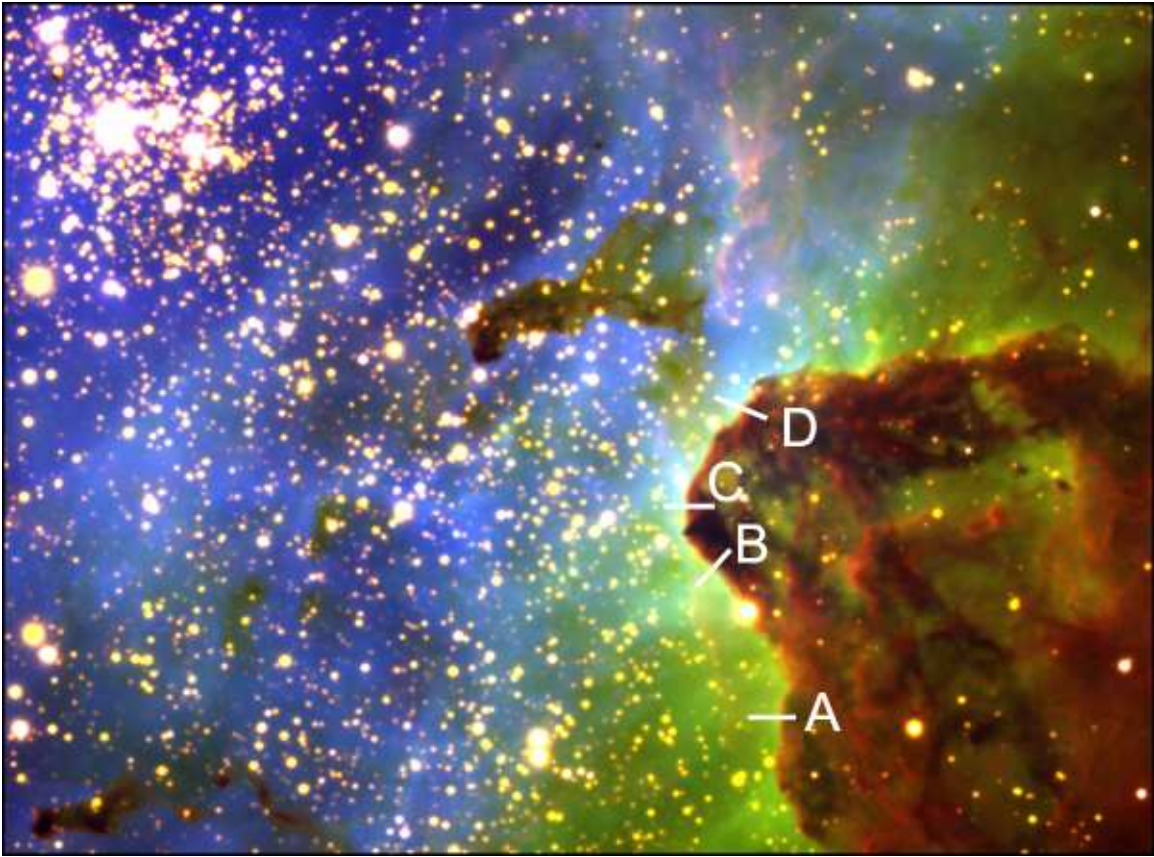


Fig. 15.— Color composite of the Western Wall in Figure 14, with H_2 in red, $\text{Br}\gamma$ in green, and $[\text{O III}] 5007\text{\AA}$ in blue. Positions A, B, C, and D mark the four slices along the PDR interface used in Figure 16 to demonstrate positional offsets in the emission line fluxes.

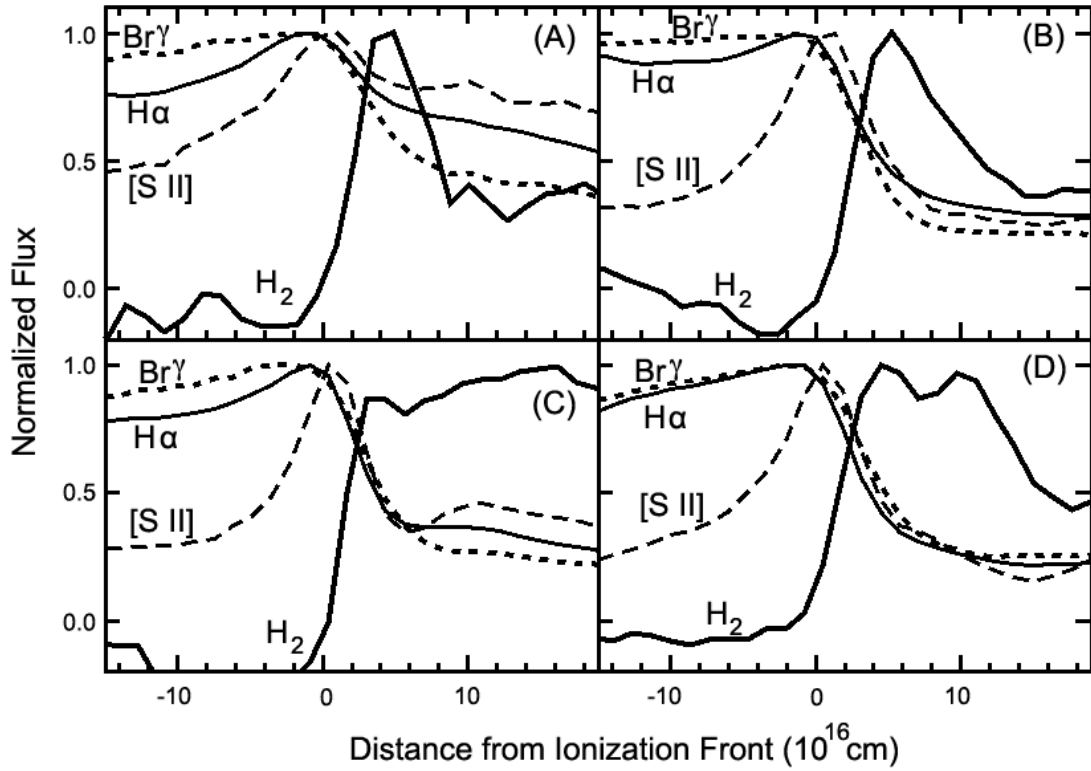


Fig. 16.— Spatial offsets of Br γ (short-dashed) and H $_2$ (bold) emission along the four positions shown in Fig. 15. The fluxes are corrected for K-band continuum as described in the text. Note the distinct offset between H $_2$ and Br γ .

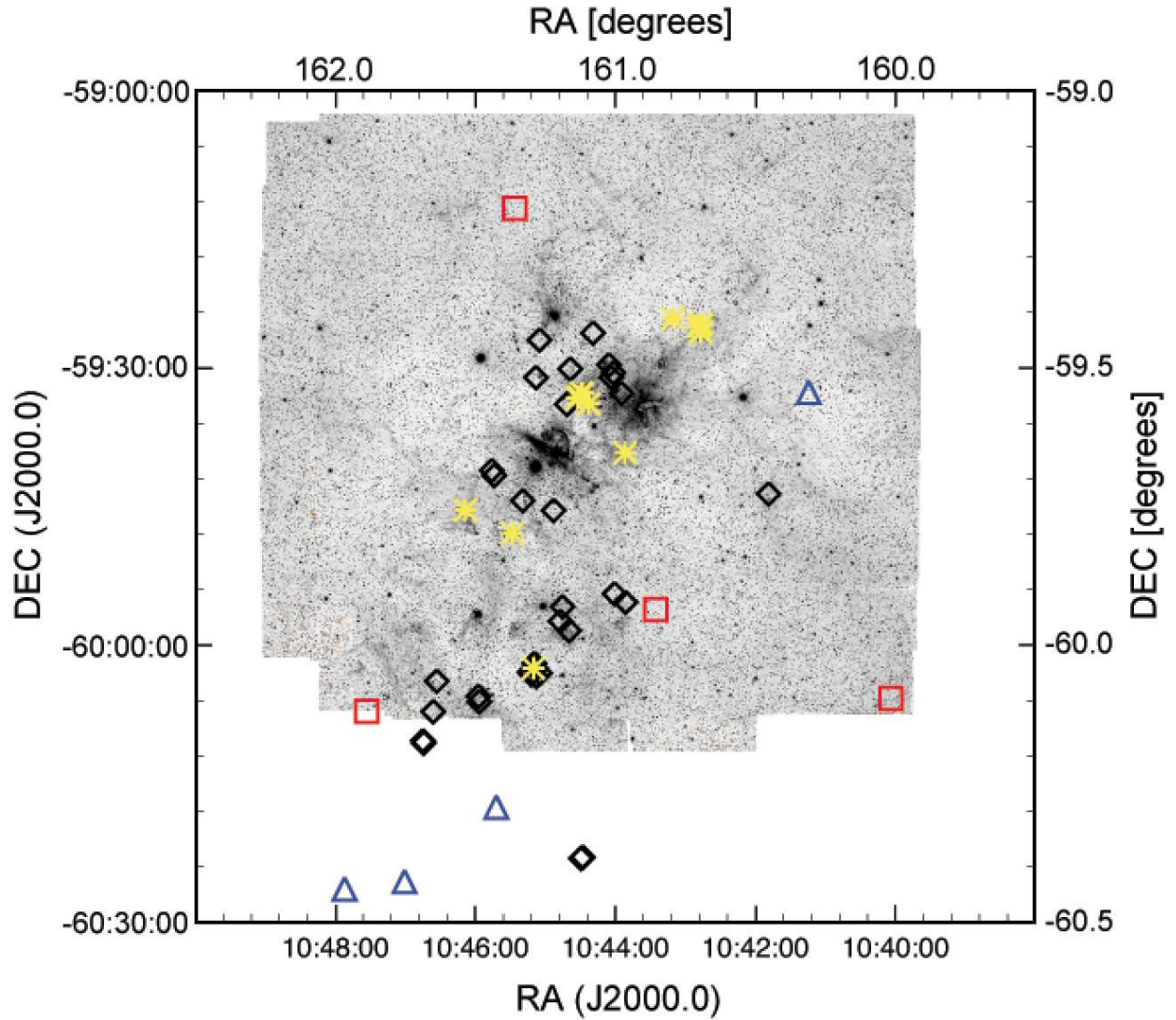
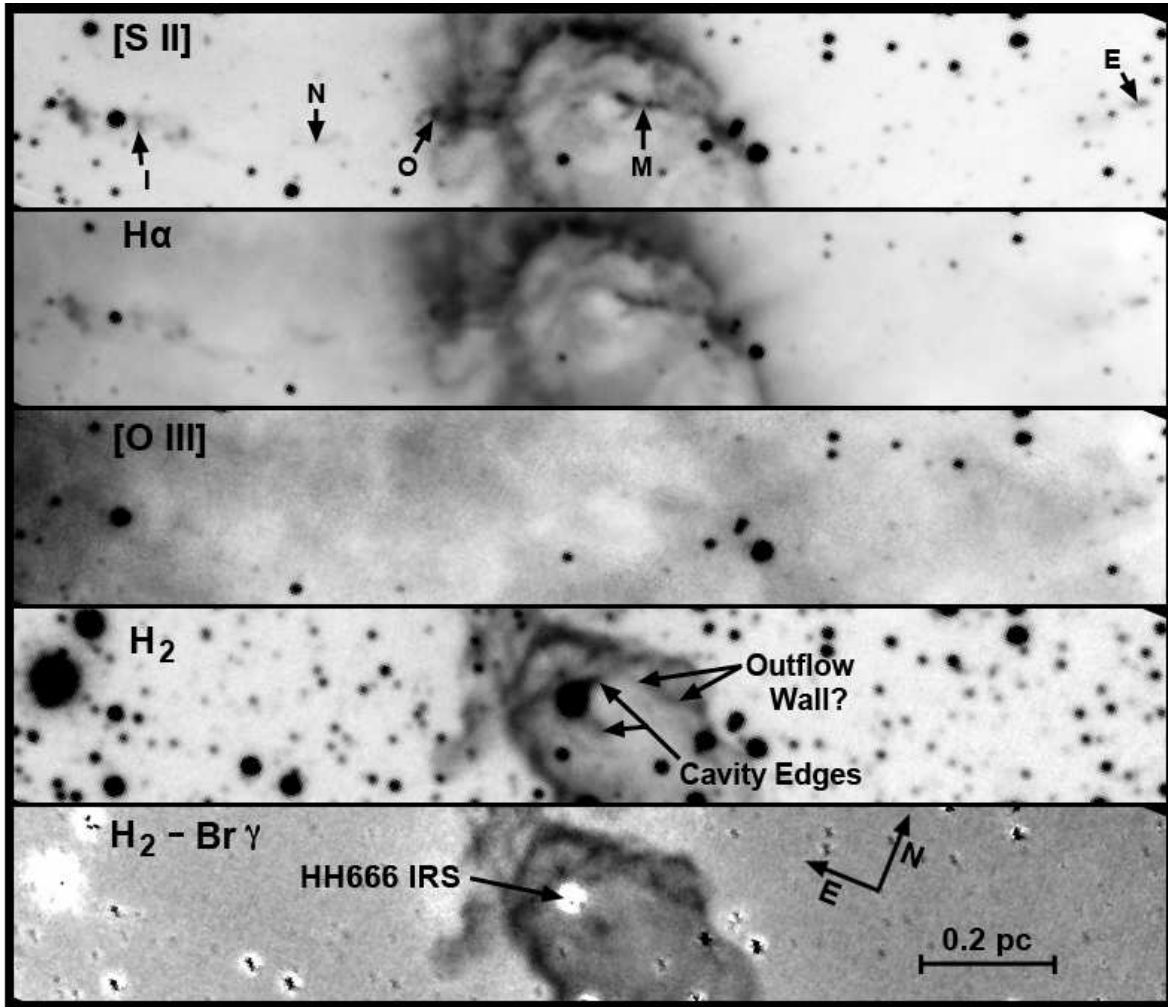
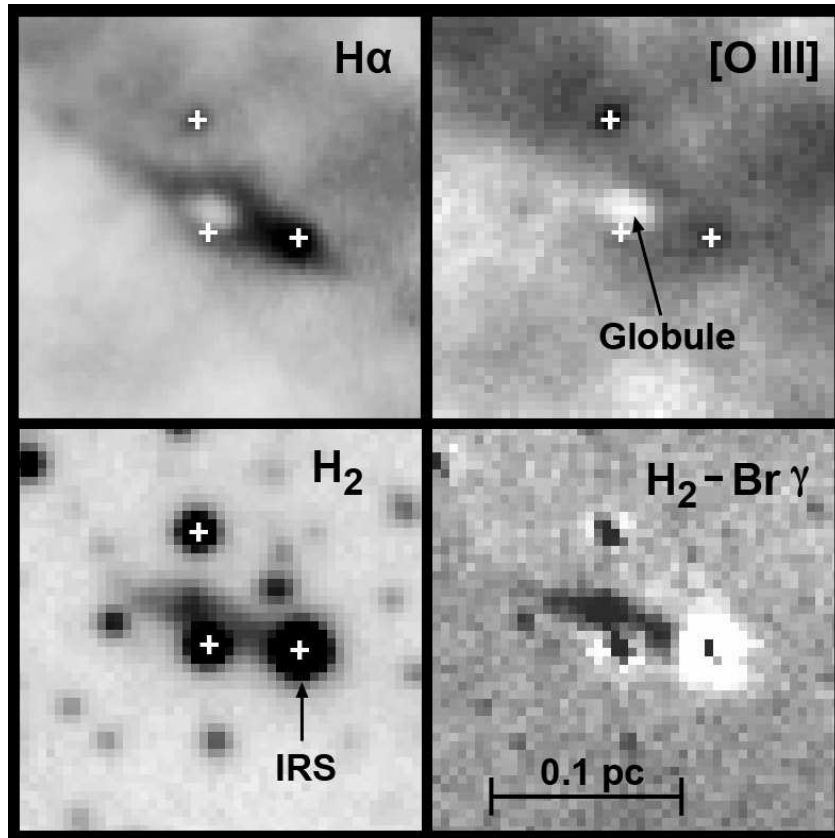


Fig. 17.— Distribution of candidate jets and previously observed outflows in Carina plotted over the narrowband H₂ image. Black diamonds indicate jets previously discovered with HST (Smith et al. 2010a), blue triangles indicate Spitzer EGOs from Smith et al. (2010b), red squares are new candidate jets visible in [S II], and yellow stars are new H₂ flow candidates found in this work.



HH 666

Fig. 18.— Narrowband optical and IR images of HH 666. Labels of the jet features in the [S II] image follow the nomenclature of Smith et al. (2004a). The H $_2$ emission outlines the edges of a cavity along the jet, and may also trace the northern boundary of the outflow, but no H $_2$ is unambiguously associated with the jet.



HH 900

Fig. 19.— Composite of HH 900. The dark globule and IRS (PCYC 838) discussed in the text are marked. Plus-signs denote the location of three bright stars in the region.

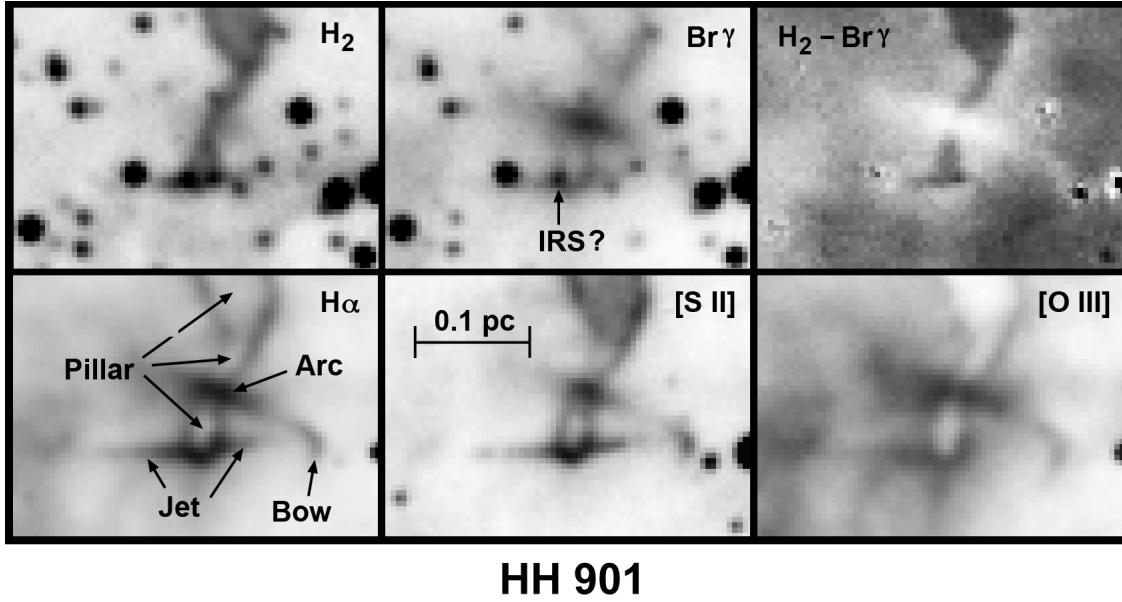


Fig. 20.— Composite of HH 901. H₂ emission is evident as the jet emerges from the pillar. The objects labeled arc, jet, pillar, and a potential driving source (IRS) are discussed in the text.

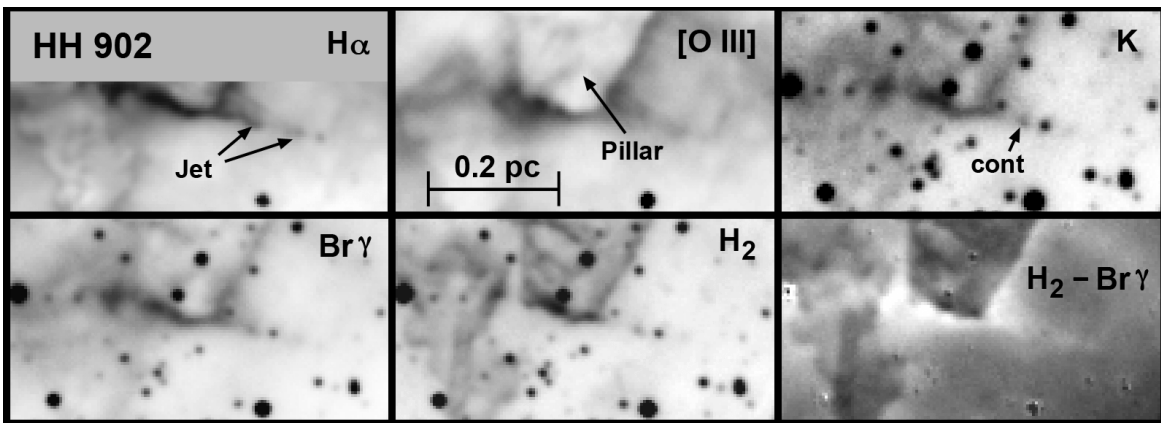


Fig. 21.— Composite images of the HH 902 region. Labeled objects are described in the text.

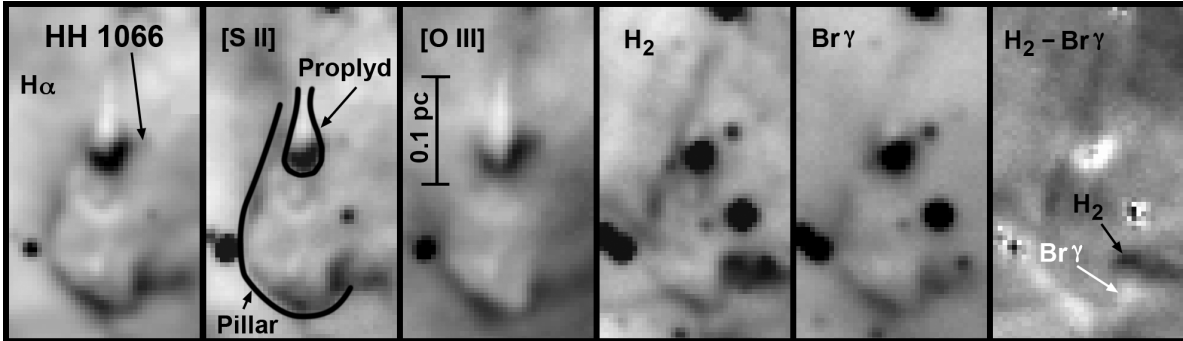
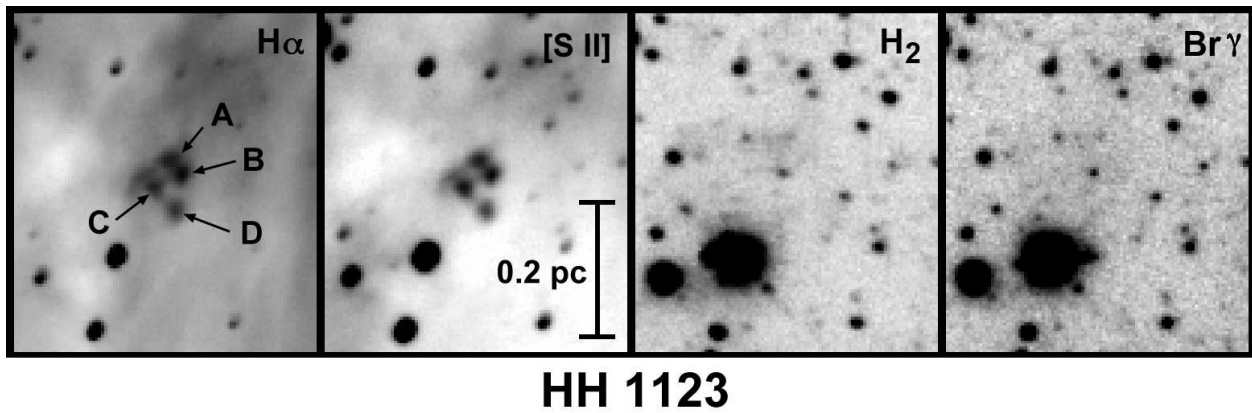


Fig. 22.— Composite of the proplyd and pillars near HH 1066 (formerly HHc-1). The head of the proplyd shows a distinct C-shape as it is illuminated by stars to the south. Regions marked as bright $\text{Br}\gamma$ and H_2 emission are discussed in the text. The star at the head of the proplyd is PCYC 429.



HH 1123

Fig. 23.— Knots of $\text{H}\alpha$ and $[\text{S II}]$ in HH 1123. No clear jet structure exists in any of the observed wavelengths.

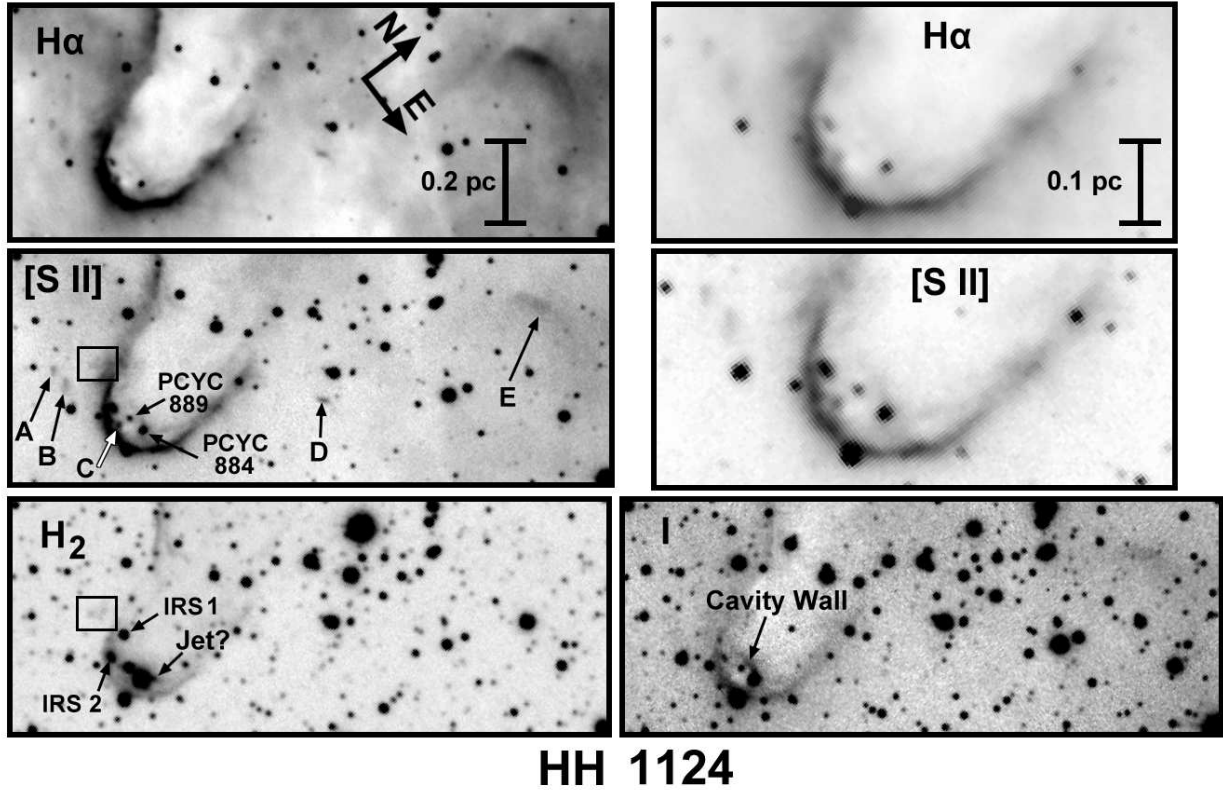


Fig. 24.— Optical emission-line knots A–C outline a bent flow that emerges to the west of the head of the pillar shown in Area 18 of Fig. 8. Knot D and the bow-shaped object E lie to the east. The source labeled IRS (PCYC 884) shows what appears to be a cavity wall in reflected continuum. An extension in the H_2 image (also visible in the $H_2 - Br\gamma$ image in Fig. 8) may outline a jet, but it could also define a photodissociation surface on the irradiated pillar. Emission in the boxed region is discussed in the text.

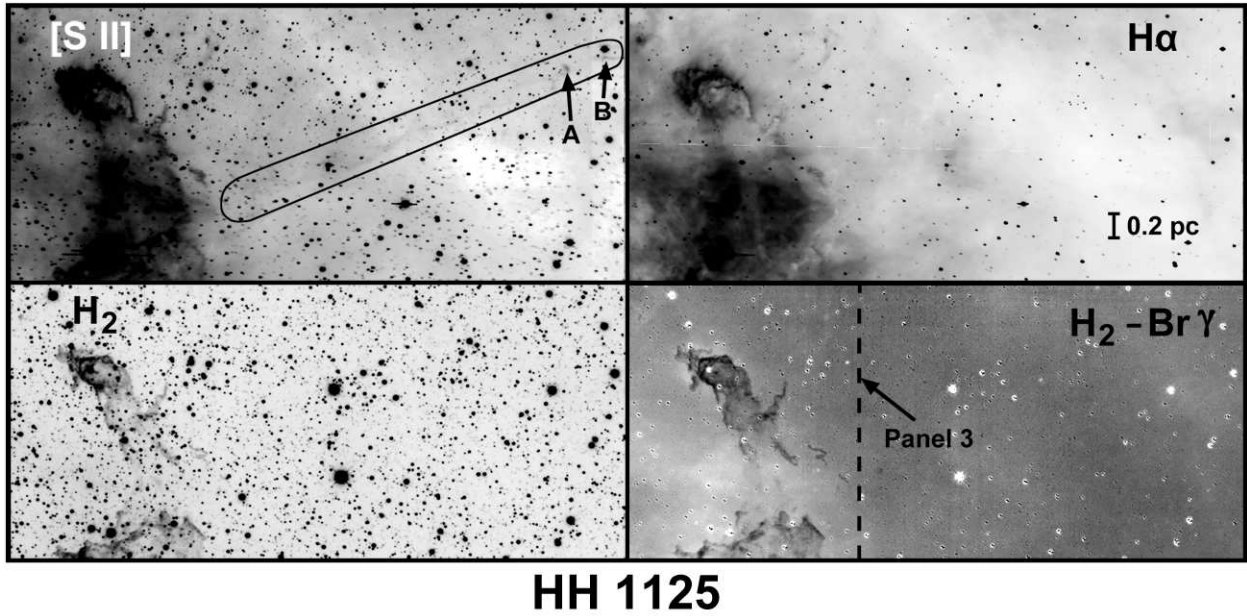


Fig. 25.— The elongated region marked in the upper left panel encloses a thin filament of [S II] emission that comprises HH 1125. There is no clear driving source if the object is a jet, though the morphology of knot A resembles that of a bow shock. The filament is not visible in H₂, Br γ , [O III] or H α . A dashed line marks the edge of Area 3 in Fig. 3.

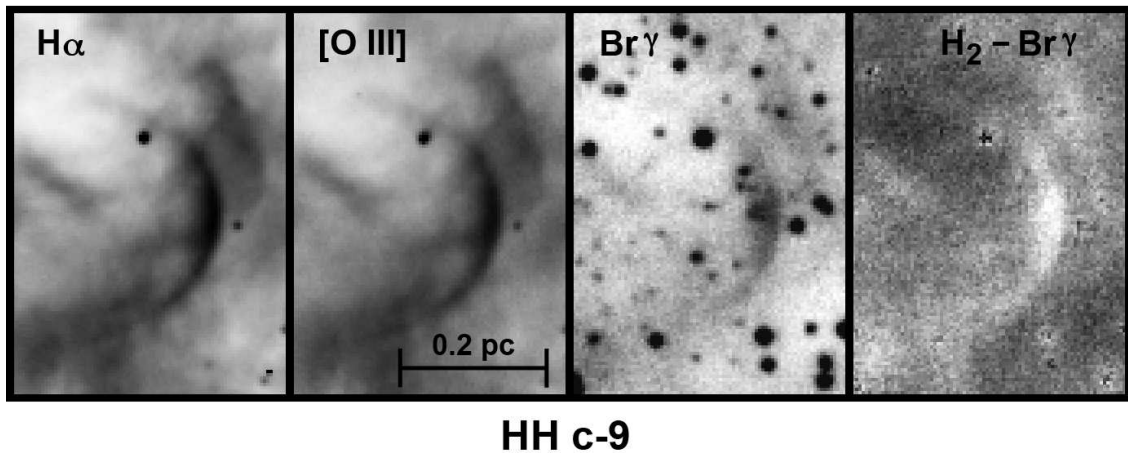
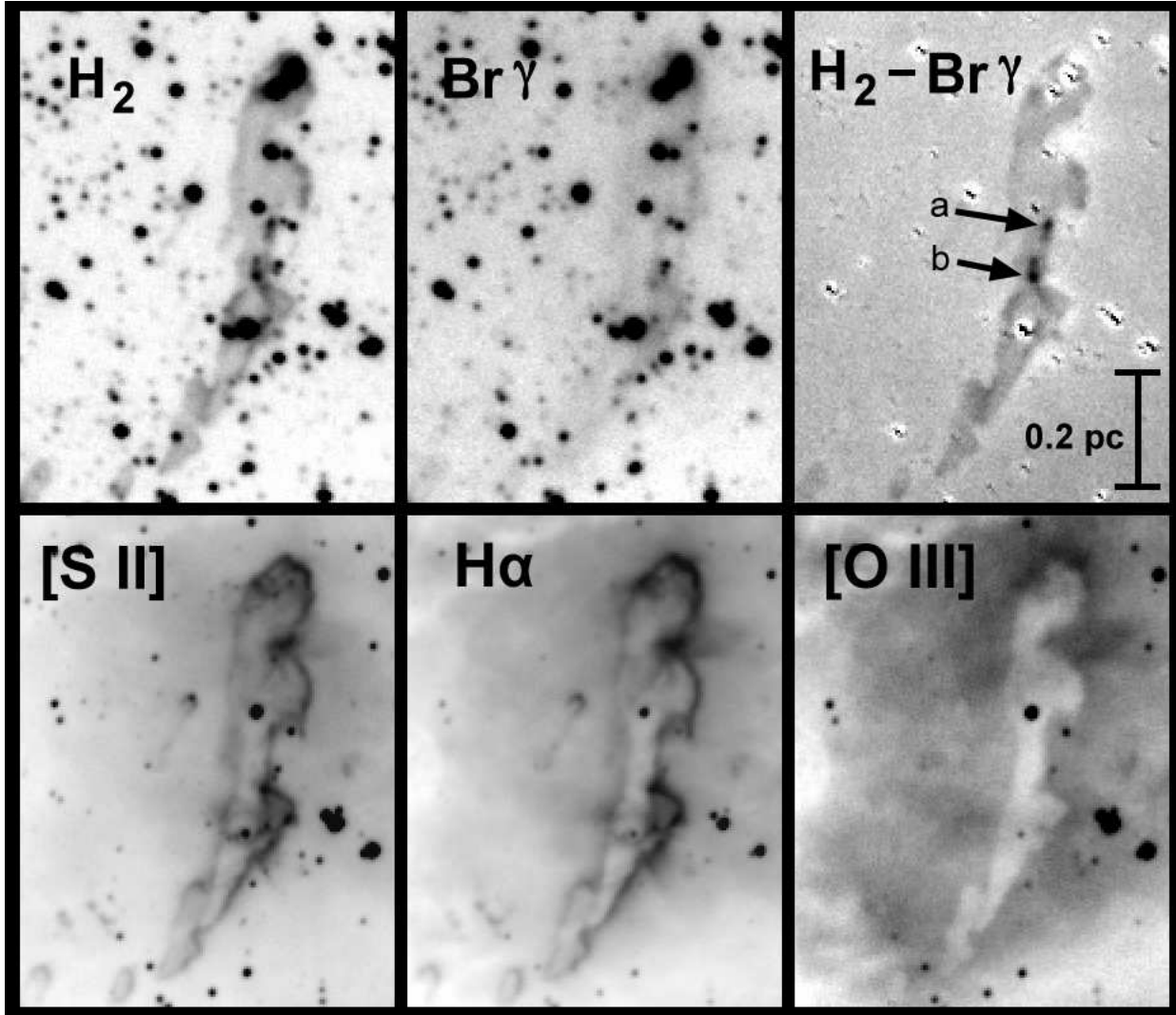


Fig. 26.— The highly-ionized arc-shaped HH c-9 is bright in H α and [O III], and has a similar morphology in Br γ . No H₂ is present in this object. If the object is a bow shock, its driving source remains unidentified.



MHO 1609

Fig. 27.— Two bright, extended H₂ features within an irradiated pillar comprise MHO 1609. Several optical outflow candidates were identified from this detached globule in the HST data.

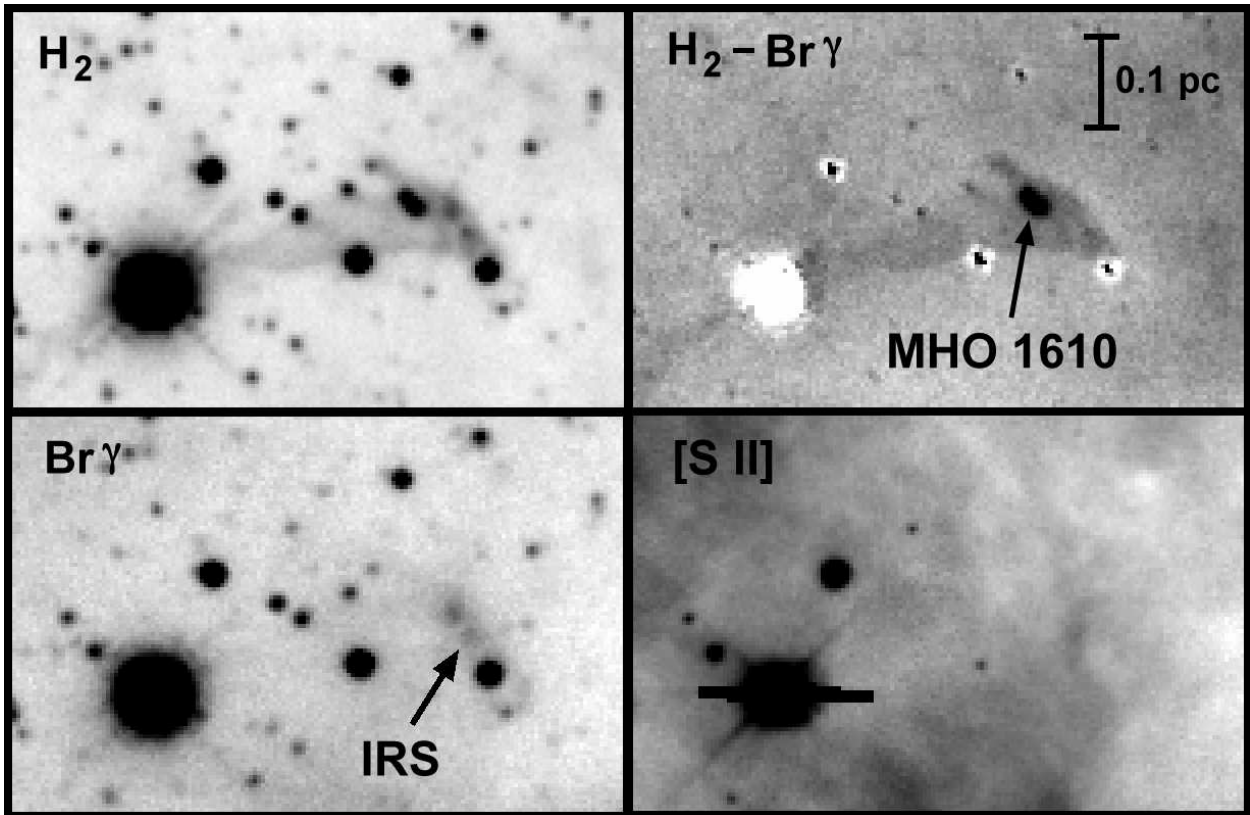
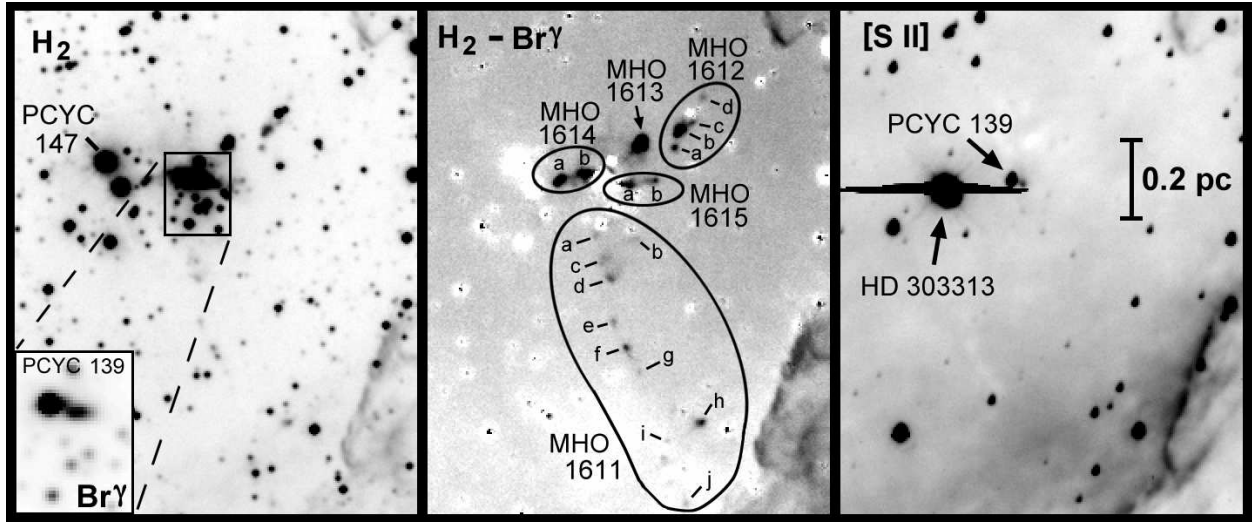
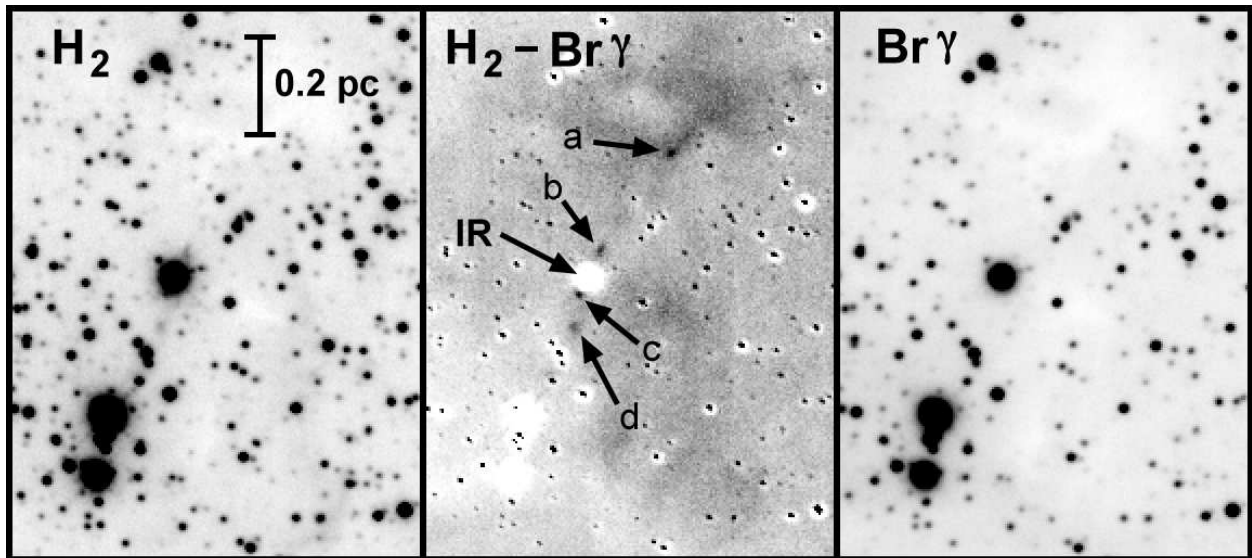


Fig. 28.— Composite images of MHO 1610 (see also Area 10 of Fig. 5) reveal a single bright H_2 knot with no optical counterpart. A Herschel point source at $70\mu m$ is coincident with the faint continuum source labeled IRS.



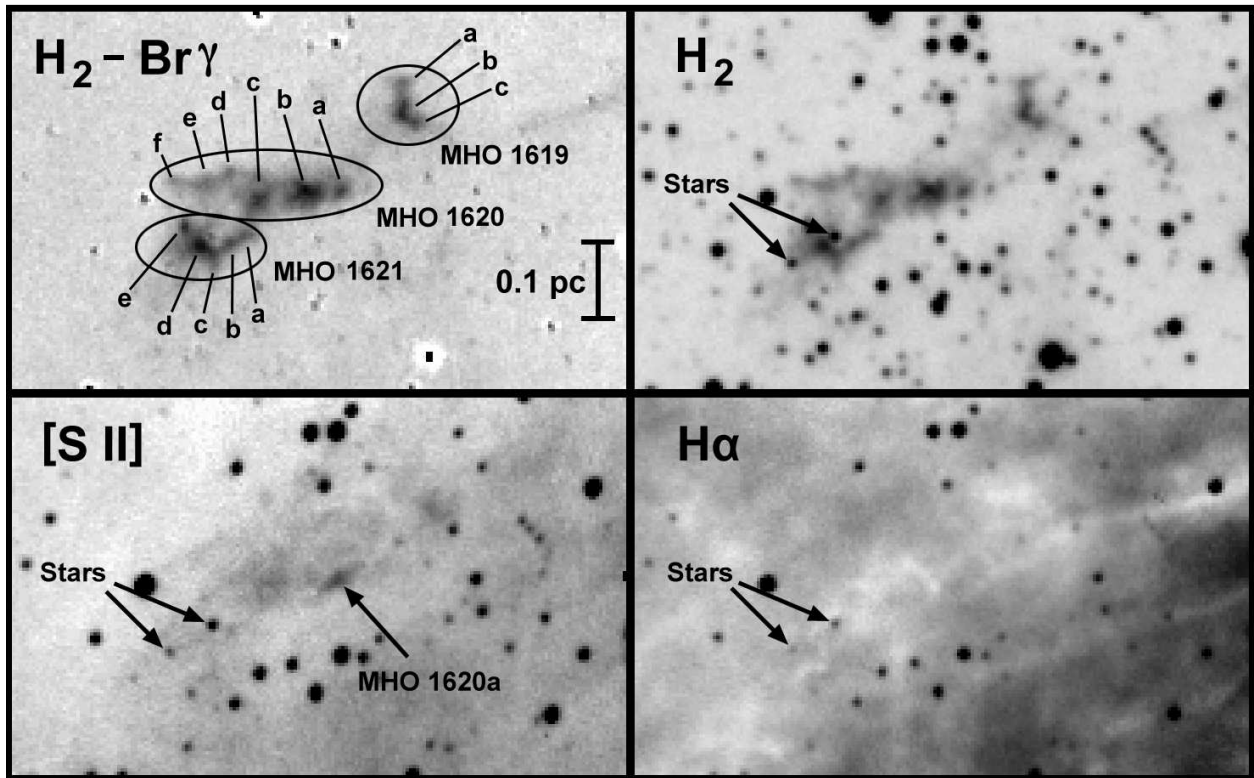
MHO 1611 - 1615

Fig. 29.— Several bright H_2 knots in the vicinity of a small cluster of stars centered on PCYC 139 comprise the candidate flows MHO 1611 - MHO 1615. These objects are identified by their H_2 emission, and lie outside a very dark dust lane to the southwest. There are no obvious optical counterparts to any of these outflow candidates.



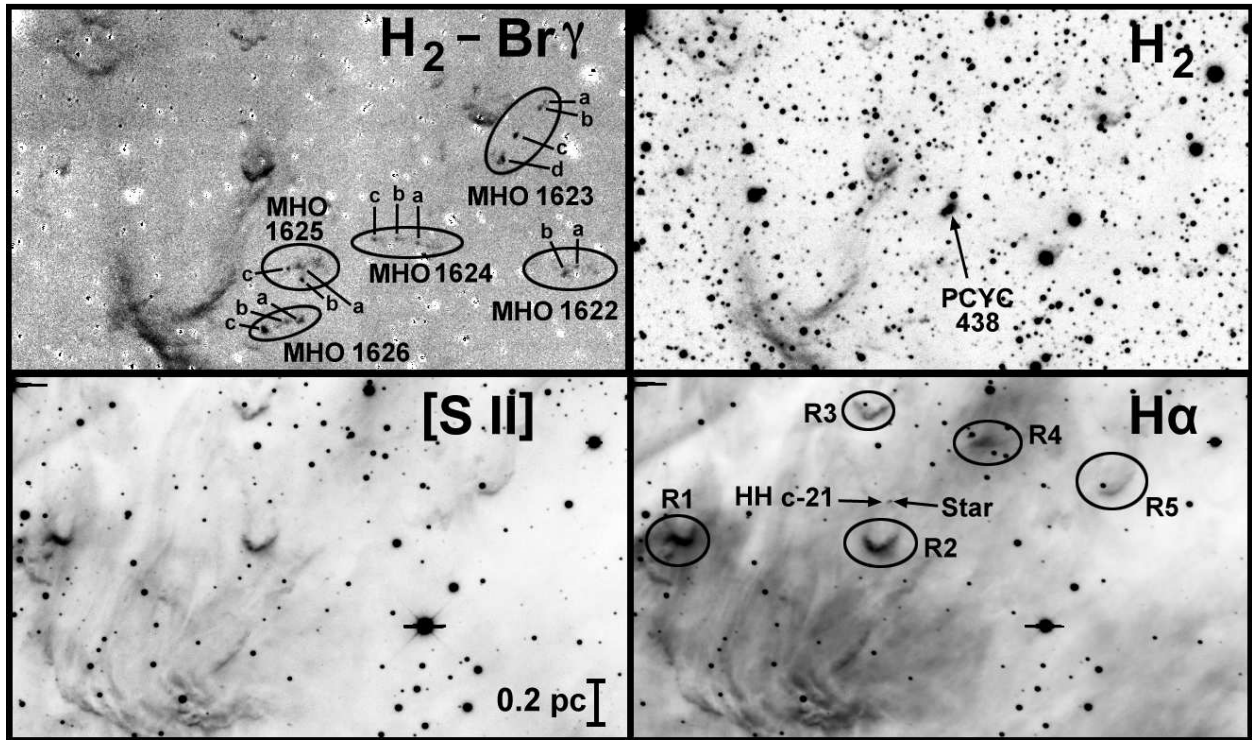
MHO 1618

Fig. 30.— Situated in the Eastern Walls, the candidate outflow MHO 1618 appears as a curving string of H_2 knots on either side of an infrared source.



MHO 1619 - 1621

Fig. 31.— Composite images of MHO 1619 – MHO 1621 (see also Area 13 of Fig. 6). MHO 1620a is visible in the [S II] image. No driving source is present.



MHO 1622 - 1626

Fig. 32.— Composite images in the G287.24-0.21 cloud, showing several strings of H_2 knots groups as MHO 1622 – MHO 1626 (see also Area 19 of Fig. 8). The arc-shaped sources R1 – R5 mark locations of irradiated pillars.

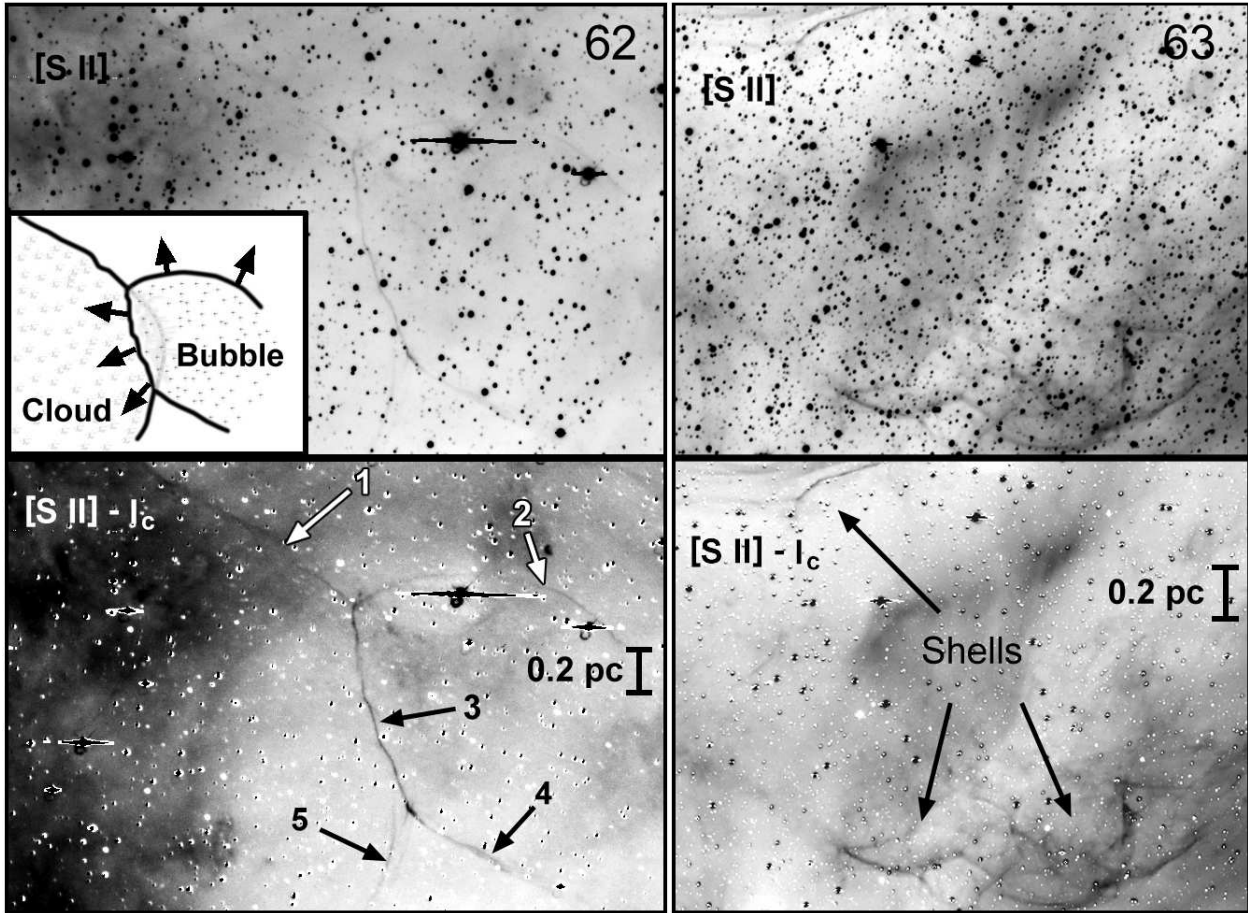
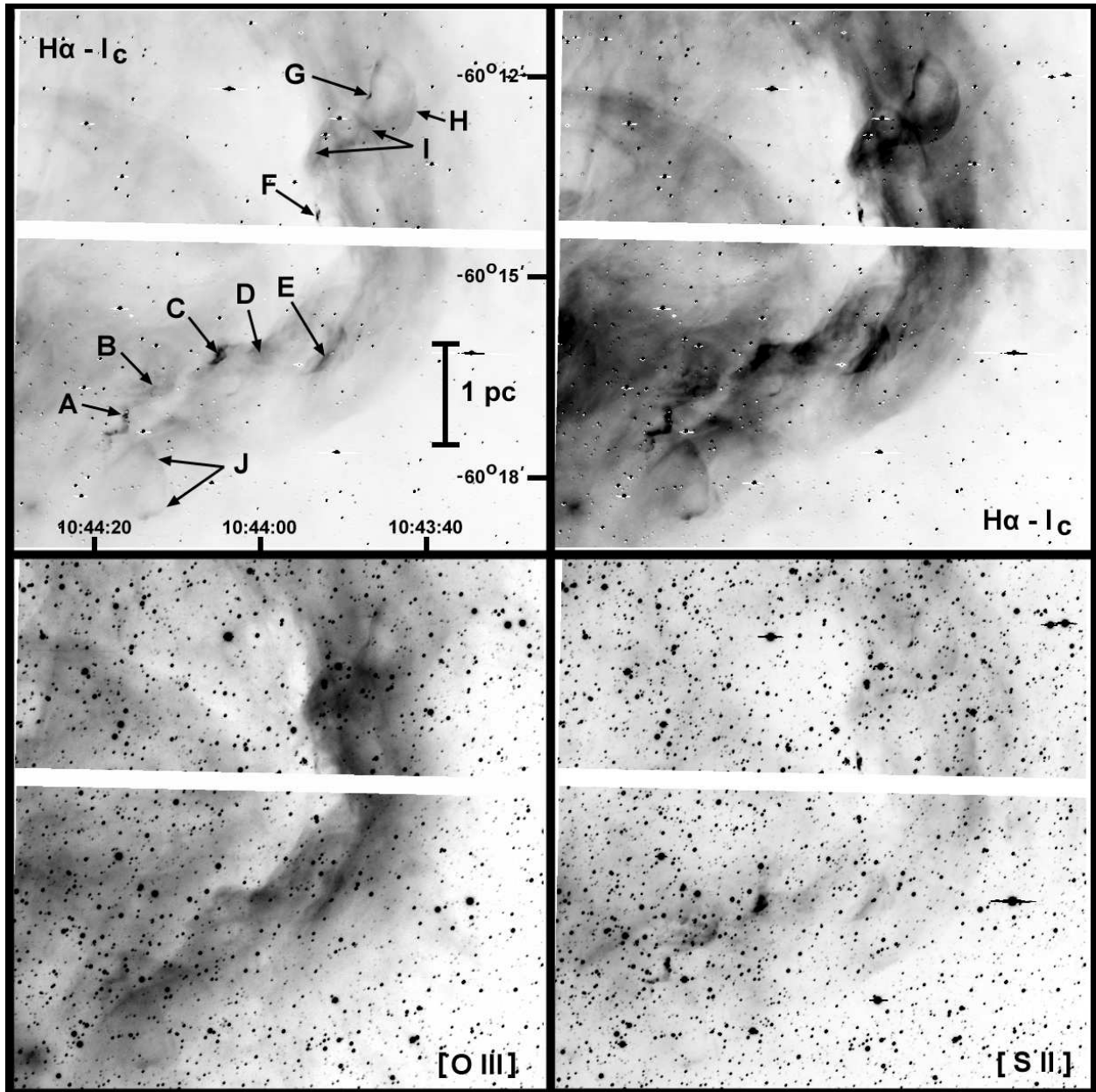


Fig. 33.— Left: A network of five narrow filaments is visible in the [S II] image (top), and the continuum-subtracted image (bottom). The model described by the inset is discussed in the text. Right: Area 63 shows an extensive network of overlapping shells in the [S II] images. They are oriented as if driven by the massive stars to the north of this region.



Southwest Loop

Fig. 34.— Cavities, filaments and knots in the Southwestern Loop, located at the edge of the bright optical emission in Carina. Top: $H\alpha$ images with scaled I_c continuum subtracted, presented at two different greyscales. Bottom: A narrowband $[O III]$ image (left) and $[S II]$ image (right).

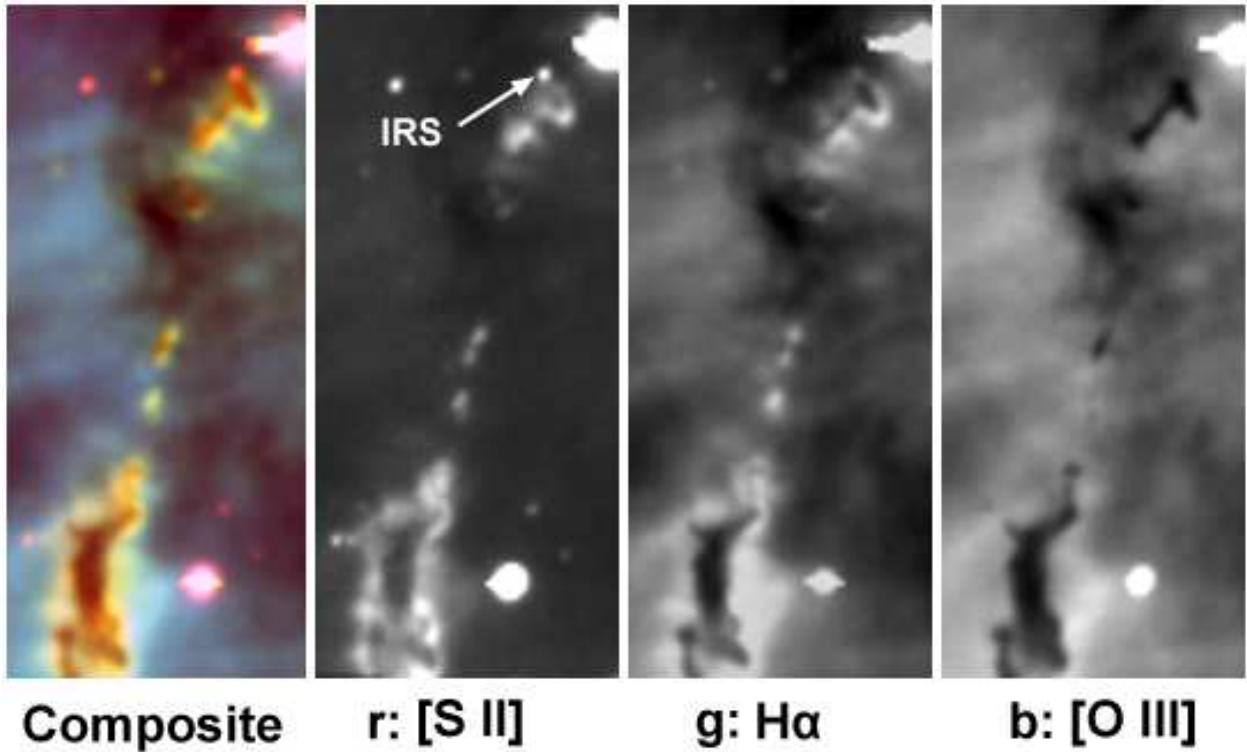


Fig. 35.— An optical color composite (red = [S II], green = H α and blue = [O III]) of the remnants of a pillar to the north of Carina’s finger, shown in Area 37 of Fig. 11. The bright near-IR source labeled IRS is discussed in the text. The emission lines arise from PDRs at the surface of the knots.